December 2019

Hybridly Integrated Diode Lasers for Emerging Applications: Design, Fabrication, and Characterization

Yeyu Zhu
Clemson University, rainyleafyy@gmail.com

HYBRIDLY INTEGRATED DIODE LASERS FOR EMERGING APPLICATIONS: DESIGN, FABRICATION, AND CHARACTERIZATION

A Dissertation
Presented to
the Graduate School of
Clemson University

In Partial Fulfillment
of the Requirements for the Degree
Doctor of Philosophy
Electrical Engineering

---

by
Yeyu Zhu
December 2019

Accepted by:
Dr. Lin Zhu, Committee Chair
Dr. John Ballato
Dr. Pingshan Wang
Dr. Hai Xiao

ABSTRACT

The emerging applications of LiDAR, microresonator based frequency comb, and photon pair generation in photonic integrated circuits (PICs) have attracted lots of research interests recently. The single frequency, high power, narrow-linewidth, tunable semiconductor lasers are highly desired for the implementation of these emerging applications in future PICs. In this dissertation, we use the hybrid integration via edge coupling to obtain the integrated diode lasers for future PICs, since the active chip and the passive chip can be fabricated and optimized independently.

We demonstrate hybridly integrated narrow-linewidth, tunable diode lasers in the Indium Phosphide/Gallium Arsenide-silicon nitride (InP/GaAs-Si_3N_4) platform. Silicon nitride photonic integrated circuits, instead of silicon waveguides that suffer from high optical loss near 1 μm, are chosen to build a tunable external cavity for both InP and GaAs gain chips at the same time. Single frequency lasing at 1.55 μm and 1 μm is simultaneously obtained on a single chip with spectral linewidths of 18-kHz and 70-kHz, a side mode suppression ratio of 52 dB and 46 dB, and tuning range of 46 nm and 38 nm, respectively. The resulting dual-band narrow-linewidth diode lasers have potential for use in a variety of novel applications such as integrated difference-frequency generation, quantum photonics, and nonlinear optics. We also demonstrate one potential application of the dual-band diode laser in beam steering. The dual-band diode laser combined with a waveguide surface grating can provide the beam steering by tuning the wavelength of the light signal.

However, the output power of the hybridly integrated diode lasers is still limited. Integrated coherent beam combining (CBC) is a promising solution to overcome this limitation. In this dissertation, coherently combined, integrated diode laser systems are experimentally demonstrated through hybrid integration. A chip-scale coherently combined laser system is experimentally demonstrated in the InP-Si_3N_4 platform through the manipulation of optical feedbacks at different output ports of the coupled laser cavities. Coherent combining of two InP-based reflective semiconductor amplifiers is obtained by use of the cross-coupling provided by an adiabatic 3 dB coupler in silicon nitride, with a combining efficiency of ~92%. The novel system not only realizes the miniaturization of coherent laser beam combining but also provides a chip-scale platform to study the coherent coupling between coupled laser cavities.

Besides, the emerging platforms (i.e., gain chips based on semiconductor quantum dots, silicon-carbide-on-insulator and lithium-niobate-on-insulator) have attracted intense interests in recent years. The hybridly integrated diode lasers through edge coupling are demonstrated in these emerging platforms.

In addition, we study the Parity-Time (PT) symmetry in the chip-scale hybrid platform. PT symmetric coupled microresonators with judiciously modulated loss and gain have been widely studied to reveal many non-Hermitian features in optical systems. The phase transition at the exceptional points (EPs) is a unique feature of the PT symmetric non-Hermitian systems. In this dissertation, we propose and demonstrate an electrically pumped, hybridly integrated chip-scale non-Hermitian system, where the optical gain, loss and coupling are separately controlled to allow for the PT symmetry

breaking and direct access of the EPs. We use the coupled Fabry-Perot resonators through the hybrid integration of two InP active chips with one Si_3N_4 passive chip to realize the versatile control of the gain and loss. We first demonstrate the PT symmetry breaking and access of the EPs by investigating the spectral and spatial transition processes of the hybrid system induced by the asymmetric gains in the InP active chips. We then control the loss distribution in the Si_3N_4 passive chip so that the system loss contrast exceeds the coupling coefficient, which leads to the PT symmetry breaking and coherent addition of the two coupled lasers. Our integrated non-Hermitian optical system in the chip-scale hybrid integration platform successfully bridges the non-Hermitian physics and photonic integrated circuits and is able to expand the practical applications of non-Hermitian optical systems to a whole new stage.

DEDICATION

To:

My family and friends!

ACKNOWLEDGMENTS

First and foremost, I would like to express my gratitude to Dr. Lin Zhu, my advisor for taking me on as a graduate student and for providing such a tremendous amount of support, advice and encouragement during my study at Clemson.

I would also like to thank Professor John Ballato, Professor Pingshan Wang and Professor Hai Xiao for being my committee member and for providing advice on my research.

Thank all my colleagues for all their effort to help me through the entire project. For all the members in our group, thank you for all your help and the great team work to get where we are today. I cannot say how much I value you and the time I spent with you together.

Thank you also to the staff members in Gatech Institute for Electronics and Nanotechnology and Cornell Nanoscale Facility (CNF) for their help on the facilities training and for their invaluable experience on device fabrication.

For all the kind people who helped me and all my lovely friends who supported me, you may or may not see this dissertation, but I thank each single one of you for helping me to get through life.

At last, I am very grateful to my family for their endless and unconditional love and support.

TABLE OF CONTENTS

Page

Table of Contents (Continued)

Page

Table of Contents (Continued)

Page

LIST OF FIGURES

List of Figures (Continued)

Figure Page

List of Figures (Continued)

Figure Page

List of Figures (Continued)

Figure Page

List of Figures (Continued)

Figure Page

List of Figures (Continued)

Figure Page

LIST OF ACRONYMS

AR — Anti-Reflection

BOX — Buried Oxide

CBC — Coherent Beam Combining

CMOS — Complementary Metal–Oxide–Semiconductor

CPA — Coherent Perfect Absorber

Cr — Chromium

CW — Continuous Wave

DBR — Distributed Bragg Reflector

DC — Directional Coupler

DFB — Distributed Feedback

DSH — Delayed Self-heterodyne

EBL — Electron Beam Lithography

EOM — Electro-Optic Modulator

EPs — Exceptional Points

ESA — Electrical Spectrum Analyzer

FDTD — Finite-Difference Time-Domain

FEM — Finite Element Method

F-P — Fabry-Perot

FPC — Fiber Polarization Controller

FSR — Free Spectral Range

FWHM — Full Width at Half Maximum

List of Acronyms (Continued)

GaAs — Gallium Arsenide

HR — High Reflection

InP — Indium Phosphide

IR — Infrared

I-V — Current-Voltage

LD — Laser Diode

L-I — Light Intensity-Current

LiDAR — Light Detection and Ranging

LPCVD — Low-Press Chemical Vapor Deposition

MMI — Multiple Mode Interferometers

MOPA — Master Oscillator Power Amplifier

OSA — Optical Spectrum Analyzer

PD — Photodiode

PICs — Photonic Integrated Circuits

Pt — Platinum

PT — Parity-Time

RIE — Reactive Ion Etching

RSOA — Reflective Semiconductor Optical Amplifier

SEM — Scanning Electron Microscope

Si — Silicon

Si_3N_4 — Silicon Nitride

List of Acronyms (Continued)

SiO_2 — Silicon Dioxide

SMSR — Side Mode Suppression Ratio

SOI — Silicon on Insulator

SWaP — Size, Weight and Power consumption

TEC — Thermoelectric Cooler

VOA — Variable Optical Attenuator

CHAPTER ONE

INTRODUCTION

1.1 Background and motivation

The cost of modern optical communication systems is still high due to the cost of assembly and packaging, which limits the scalability of the number of optical components within an optical system. Photonic integrated circuits (PICs), also known as planar lightwave circuits, are devices comprising a variety of photonic functional elements, such as lasers, detectors, modulators, filters, routers and nonlinear processing units, on a single small chip, which are considered promising for a revolution in optoelectronics [1]. PICs can significantly reduce the photonic system size, weight, operation power, and cost, and have attracted a lot of research interest since the late 1960s [2]. They have provided a foundation platform for cost-effective, high-performance solutions in a wide range of applications, such as optical communication systems, optical interconnects and free-space communication systems [3].

PICs have been fabricated in different material systems, such as silicon, III-V semiconductors, dielectrics, polymers, and nonlinear crystal materials [4]. The dominant platforms for commercially-available PICs are the monolithic III-V semiconductors (gallium arsenide and indium phosphide) and silicon based material systems [5]. III-V semiconductors are well suitable for light generation and detection. In addition, both passive and active components can be integrated in the same substrate, which requires advanced fabrication process [6]. However, the manufacturing cost of gallium arsenide

(GaAs) or indium phosphide (InP) based PICs is not reduced proportionally due to limited substrate sizes, 150mm or less, and hence they are not the best choices for large scale production. Silicon-based PICs have also become very popular in the past decade since it is potential to produce low cost, high quality integrated photonic systems by use of mature complementary metal–oxide–semiconductor (CMOS) technologies with low cost and high-volume processing [7]. Silicon based materials have desirable properties for passive components and modulators. They have gained intense interests no matter in industry or academia. Low loss waveguides in silicon have been demonstrated with losses over an order of magnitude improvement over their indium phosphide counterparts. Many passive silicon waveguide-based circuits, such as wavelength multiplexers/ demultiplexers, filters and couplers, have been available commercially.

Although silicon (Si) waveguides are good for providing tight optical confinement and large third order optical nonlinearity, they are not suitable for the applications that require high power continuous wave (CW) light due to the two-photon absorption limiting the maximum light intensity. An alternative candidate, silicon nitride (Si_3N_4), has been used as a platform for integrated photonics to create passive optical components with high performance due to its low nonlinearity, high index contract with silica, very large transparency window, low linear propagation loss, and low thermal drift [8]. Besides, silicon nitride waveguides are obtained without silicon-on-insulator (SOI) and therefore are lower cost.

However, it is difficult to directly obtain electrically pumped laser sources in the passive platform. So, for now, most of silicon based photonic integrated systems are

driven by external laser sources via fiber coupling that will compromise the compactness. Recently, one promising solution for this problem is through hybrid integration that can break the material limitations.

Hybrid integration has become a promising approach for multi-functional PICs beyond monolithic integration in recent years [9-11]. Such a hybrid system can create active and passive components on their native substrates with different material systems [12-14]. The outputs of the active and passive devices are optically coupled through mode matching or free-space optics [15-17]. A unique advantage associated with the hybridly integrated diode laser system is that the optical resonator and highly absorbing active medium are separated, allowing for independent component optimization and better reliability. Besides, the Schawlow-Townes linewidth of the laser is greatly reduced due to the increased cavity photon lifetime [18], which is obtained through increasing the effective cavity length and/or decreasing the cavity loss with the low loss PICs. Therefore, hybridly integrated diode lasers in the passive silicon nitride platform are highly desired for future PICs.

The hybrid integration can be obtained through lensed coupling, edge coupling, vertical coupling, die/wafer bonding, or heteroepitaxy as shown in Fig. 1.1 [19]. The edge coupling and wafer/die bonding are two main methods utilized for obtaining the hybrid integration. For wafer bonding method, III-V dies/wafers are directly bonded on a silicon wafer. Then all the active components are processed. The alignment between the active and passive components is limited by the lithography accuracy. It may provide a cost-effective, high-performance platform for optical systems with large number of active

components. Instead, edge coupling requires precise alignment between the active and passive chips, which is promising for optical systems with only a few lasers. A unique advantage of the edge coupling approach is that the chips can be fabricated and optimized independently resulting in high performance.

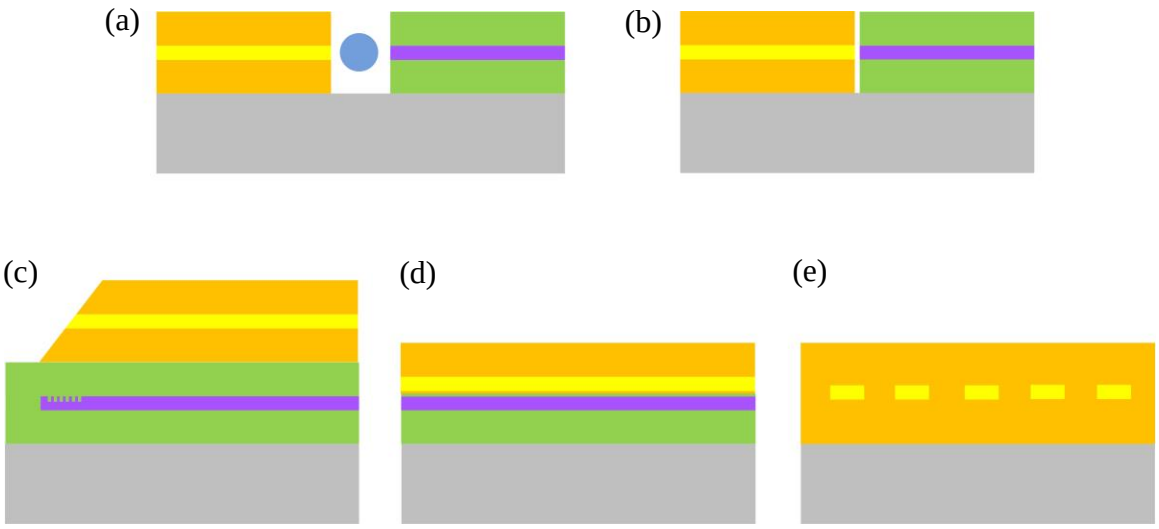

Figure 1.1: (a) Lensed-coupling. (b) Edge-coupling. (c) Vertical coupling. (d) Wafer/dies bonding. (e) Hetero-epitaxy.

1.2 Dissertation outline

In this dissertation, we mainly focused on the hybridly integrated diode lasers in the III-V/Si_3N_4 platform through edge coupling.

In Chapter 2, a spot-size converter is well designed to achieve the low coupling loss between the active chip and passive chip. The hybrid integration of a low-loss,

passive Si_3N_4 external cavity with an III-V gain chip in silicon photonics platform is presented.

Chapter 3 discusses the hybridly integrated narrow-linewidth, tunable diode lasers in InP/GaAs-Si_3N_4 platform. Single frequency lasing at 1.55 μm and 1 μm is simultaneously obtained on a single chip with the spectral linewidths of 18 kHz and 70 kHz, side mode suppression ratio of 52 dB and 46 dB, and tuning range of 46 nm and 38 nm, respectively. The beam steering is obtained using the tunable dual-band diode laser and a waveguide surface grating.

Chapter 4 describes the coherent combining of two InP-based reflective semiconductor optical amplifiers (RSOAs) by use of the cross-coupling provided by a specially designed adiabatic 3 dB coupler in silicon nitride, with a combining efficiency of ~92%. It is important for realizing on-chip high power laser sources.

Chapter 5 shows that hybridly integrated diode lasers can be obtained in the emerging platforms. We first demonstrate a chip-scale, wavelength tunable, narrow linewidth (~85-kHz), hybridly integrated diode lasers around 1.3 μm based on a quantum-dot RSOA gain chip and Si_3N_4 external cavity. Then, hybridly integrated diode lasers in silicon-carbide-on-insulator and lithium-niobate-on-insulator platforms are demonstrated.

Chapter 6 presents the demonstration of coupled Fabry-Perot (F-P) resonators as a novel non-Hermitian optical system in the InP-Si_3N_4 hybrid platform, where the optical gain, loss and coupling are separately controlled to allow for the Parity-Time (PT) symmetry breaking and direct access of the exceptional points (EPs).

Chapter 7 summarizes this dissertation and outline the future development of hybridly integrated diode lasers.

CHAPTER TWO

HYBRIDLY INTEGRATED DIODE LASERS

2.1 Introduction

Hybrid integration has become a promising candidate for multi-functional PICs beyond monolithic integration and has attracted intense interests in recent years [9, 10, 20, 21]. In such a hybrid system, active and passive components are created respectively on their native substrates with suitable material systems [12, 14, 22]. The output of the active devices can be directly end-to-end coupled to the waveguides on the passive chip [15, 23]. Until now the hybridly integrated diode lasers via edge-coupling exhibits the best performance [24] since the active chip and the passive chip can be optimized and fabricated independently. There are two main methods for obtaining the hybrid integration via edge coupling, i.e., active alignment method and flip-chip bonding method.

2.2 Direct chip-to-chip coupling

For the flip-chip bonding method, a diode laser chip is flip-chip bonded on a silicon substrate. The detailed description of this method is shown in Appendix A. Since the flip-chip bonding method requires multiple steps of complex etching and film deposition, here we just use active alignment method to demonstrate the hybrid

integration of RSOAs and a passive cavity [25]. The active alignment method for obtaining hybrid integration through direct chip-to-chip coupling is shown in Fig. 2.1. We simply mount each chip on independent xyz stages for the accurate control of the coupling between the two chips. In this dissertation, the active alignment method is mainly used for obtaining the hybrid integration for simplicity.

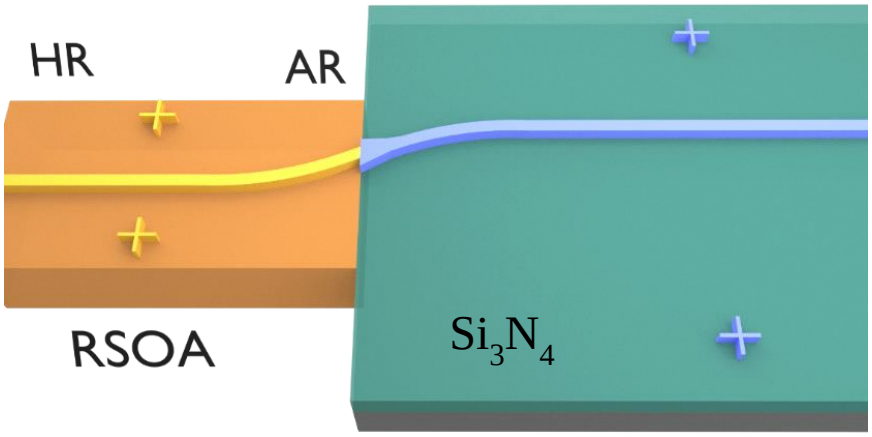

Figure 2.1: Direct chip-to-chip coupling through the active alignment method.

To obtain low coupling loss, a well-designed spot-size converter is usually needed. The mode size of a single mode ridge waveguide laser diode is about several microns in the horizontal direction and 1~2 microns in the vertical direction. However, in a silicon nitride passive single mode waveguide, the optical mode is usually well confined within the submicron waveguides. There will be a large mode mismatch between the laser diode and passive silicon nitride waveguide without a spot-size

converter, leading to high coupling losses. The coupling efficiency of two optical modes can be quantified with an overlap integral indicated by the following formula:

$$\eta = \frac{\left| \int E_1^* E_2 dA \right|^2}{\int |E_1|^2 dA \int |E_2|^2 dA} \tag{2.1}$$

where E_1 and E_2 are the complex electric fields of the optical modes, referring e.g. to a laser diode mode and waveguide mode, A is the integration cross-section.

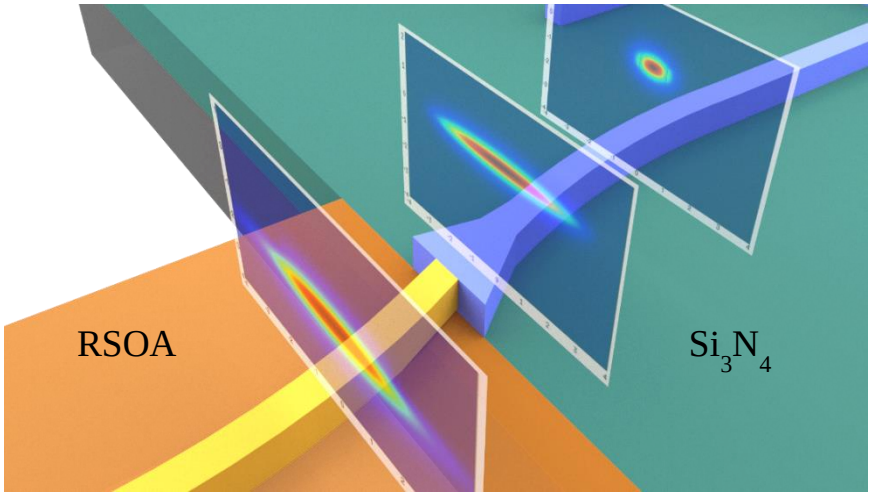

Figure 2.2: Spot size converter (the profile variation of mode propagating from the single-mode ridge waveguide laser to the silicon nitride waveguide).

For the mode mismatch problem, a well-designed spot size convertor has to be used. Figure 2.2 shows the profile variation of mode propagating from the single-mode ridge waveguide laser to the silicon nitride waveguide through a spot size convertor. Three types of taper waveguide design are investigated. All the designs have the same

total taper length of 50 μm. The first design is a linearly narrowing taper, the second design has a curved shape which obeys the circle equation, and the last one is the combination of the other two designs. We use the 3D Finite-Difference Time-Domain (FDTD) simulation to compare the performance of the three different designs. To account for the mode matching at the coupling interface, the laser output mode is used as the input signal for the tapered waveguides. Figure 2.3(b) shows the power transmission for the three designs based on FDTD simulation. The interconnection plane between the taper and waveguide is around 100 in the plot. It is obvious that the linear design has a gradually dropping transmission after the connection due to the scattering and the curved design has a step drop around the connection due to the mode mismatch. The combined design has the highest transmission over 94%. Since we use the laser output mode as the input signal in this simulation, the mode mismatch loss at the laser and taper interface has already been included and the total coupling loss is around 0.26 dB.

The RSOA is directly coupled to the passive silicon nitride waveguide through a spot-size converter. To eliminate the reflection at the interface between the RSOA gain chip and the passive silicon chip, the ridge waveguide in the RSOA gain chip and the Si_3N_4 waveguide are both angle-cleaved. Besides, the chip facet is anti-reflection (AR) coated. The interface reflectivity measured between the RSOA gain chip and passive silicon chip is less than 0.01%. In Fig. 2.4(a), we show an optical image of a RSOA gain chip directly coupled with a passive silicon chip. Figure 2.4(b) shows the variation of the insertion loss between the ridge waveguide in the RSOA gain chip and the Si_3N_4 waveguide as a function of the gap distance between them. Since we use the cleaved facet

for both chips, the smallest gap between the active chip and the passive chip we can obtain is ~1 μm (the corresponding insertion loss is ~2.5 dB). The gap distance can be further reduced with a polished silicon chip facet.

(a)

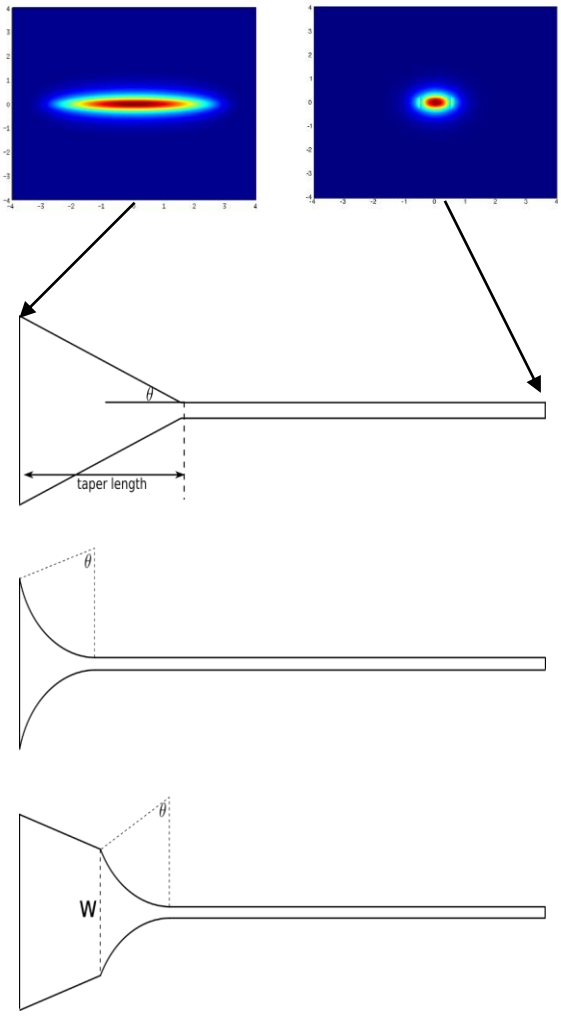

(b)

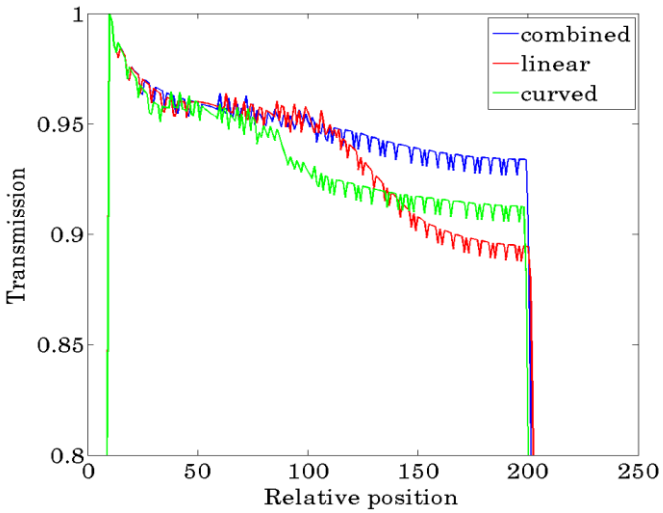

(c)

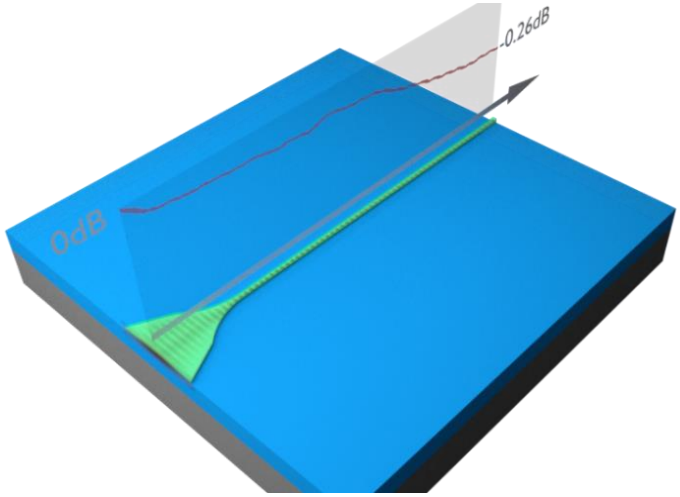

Figure 2.3: (a) Three types of the tapered waveguide design are investigated. All the designs start from a 6 μm input aperture and gradually narrow to 0.8 μm which is the width of the silicon nitride waveguide. (b) The total transmission for the three different designs. (c) The schematic plot of the spot-size convertor proposed.

(a)

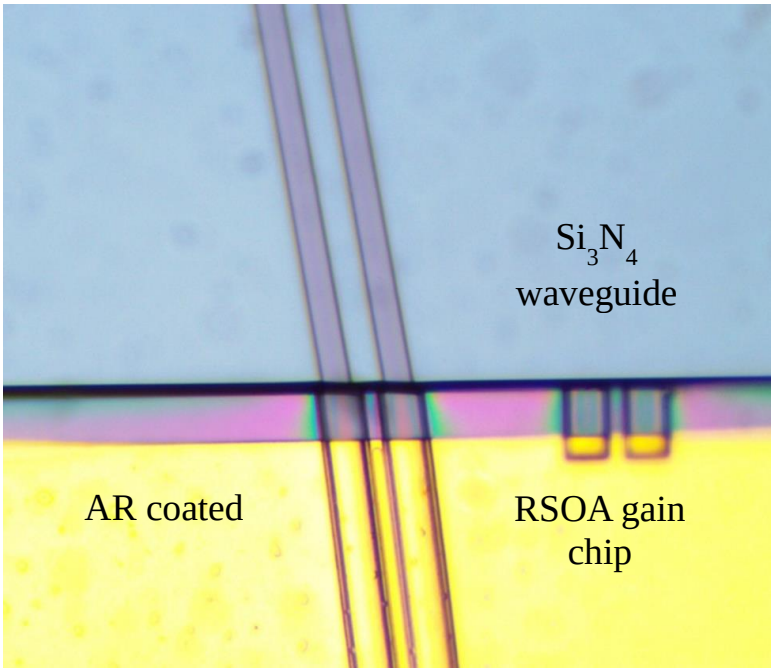

(b)

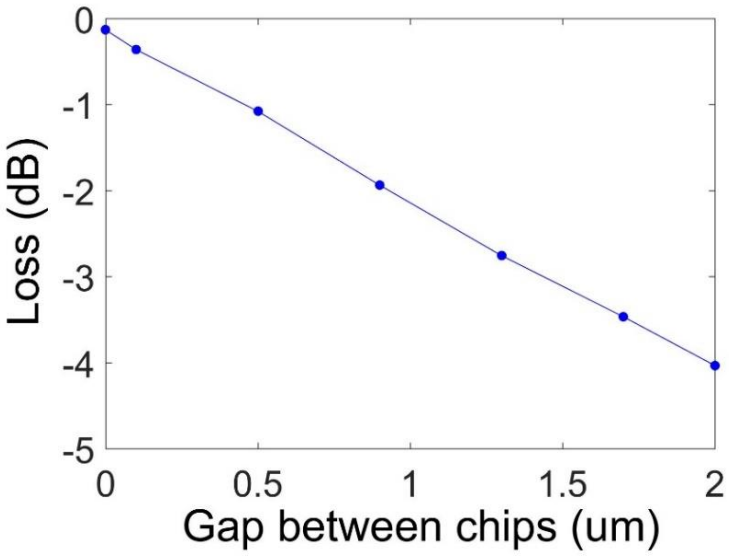

Figure 2.4: (a) A hybridly integrated RSOA gain chip with a silicon nitride waveguide. (b) the insertion loss between the two chips as a function of the gap distance between them.

2.3 Silicon nitride devices fabrication

The fabrication flow of passive silicon nitride devices is shown in Fig. 2.5. A 300-nm-thick Si_3N_4 thin film is deposited on a SiO_2-on-Si wafer using a Tystar Nitride Low-Press Chemical Vapor Deposition (LPCVD) tool. To pattern the Si_3N_4 layer, a JEOL JBX-9300FS electron-beam lithography (EBL) system is used with ZEP520A (by Zeon cooperation) as the e-beam resist. Next, the pattern is transferred to the Si_3N_4 layer using plasma etching with a CF_4/CHF_3 gas mixture in an Oxford Endpoint reactive ion etching machine. After the resist is removed, a 2-μm-thick silicon dioxide (SiO_2) is deposited on the Si_3N_4 layer using plasma-enhanced chemical vapor deposition process.

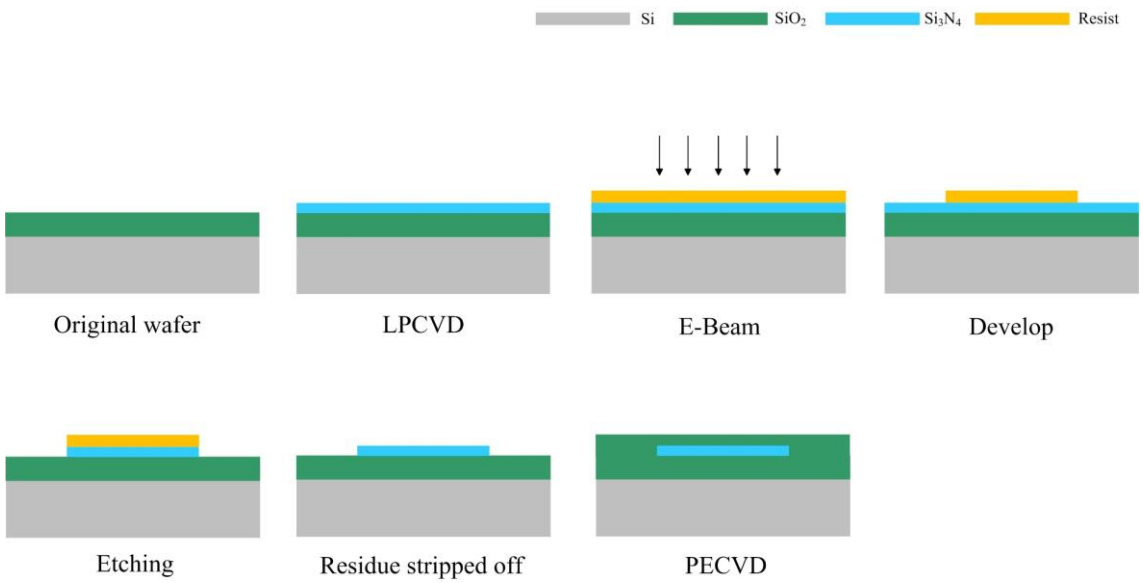

Figure 2.5: Silicon nitride devices fabrication flow.

2.4 Experimental results of integrated diode lasers

Figure 2.6(a) shows the schematic plot of the hybridly integrated diode laser. An InP RSOA gain chip is integrated with a Si_3N_4 waveguide. The two chips are mounted on independent stages for accurate control of the coupling between them. We notice that the lasing can be obtained here in the chip-scale hybrid platform. The cleaved Si_3N_4 waveguide facet can provide enough optical feedback for lasing. Figure 2.6(b) shows the corresponding light intensity-current (L-I) curve of the hybridly integrated diode laser. The threshold current is ~50 mA. Milliwatts output power is obtained from the output port using a lensed fiber.

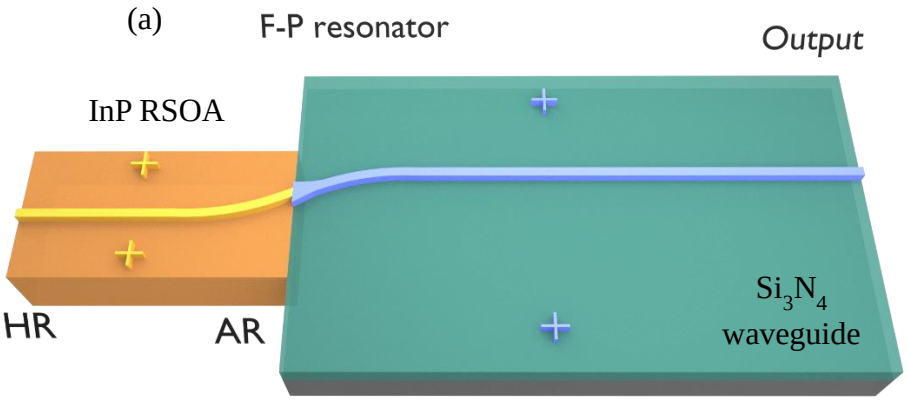

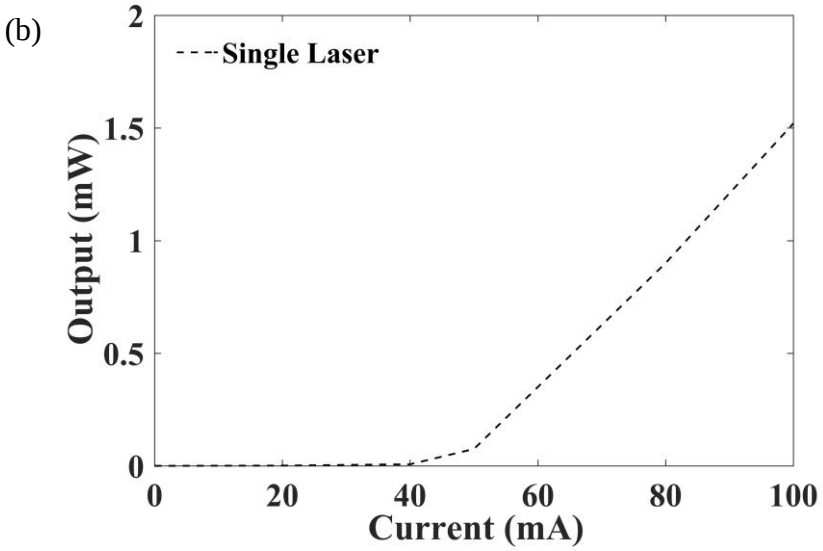

Figure 2.6: Experiment results of the hybridly integrated diode laser.

2.5 Conclusion

In conclusion, hybrid integration via edge-coupling can be obtained through the active alignment method. In order to obtain low coupling loss between the active and passive waveguides, a well-designed spot-size convertor is utilized. We have successfully demonstrated chip-scale integrated diode lasers with milliwatts output power in the InP-Si_3N_4 hybrid platform through the active alignment method.

CHAPTER THREE

NARROW-LINEWIDTH DIODE LASERS

3.1 Introduction

The performance of state-of-the-art PICs is reaching a stage that can enable a whole new class of applications beyond telecom and datacom. In recent years, the emerging applications of PICs in light detection and ranging (LiDAR) [26], microresonator based frequency comb [27], and photon pair generation [28] have aroused considerable interests. Single frequency, high power lasers are key components for implementing these emerging applications in the photonic integrated platform.

Narrow linewidth fiber and solid-state lasers have been demonstrated before by using a self-feedback circuit [29] or external cavity with narrow-band distributed feedback Bragg (DFB) reflector. However, these lasers are bulky and complex. Semiconductor lasers are promising for emerging applications where size, weight and power consumption (SWaP) are important operational parameters [30-32]. However, the conventional single frequency DFB semiconductor lasers are based on narrow stripe waveguide structures that can only provide up to tens of milliwatts output power with a few MHz spectral linewidth [33, 34]. It is difficult to reduce the linewidth of DFB semiconductor lasers below ~100 kHz. For conventional external cavity diode lasers, they are always bulky and expensive. It is difficult to direct integrate this type of lasers in a chip-scale platform.

However, it is potential for hybridly integrated diode lasers to achieve ultra-narrow linewidth and wavelength tunable operation in the chip-scale platform [35]. The Schawlow-Townes linewidth of semiconductor lasers is broadened by the refractive index and phase changes and the gain-index coupling, which resulted from the spatial variation of the internal intensity and carries density affected by spontaneous emission events [36]. An external cavity can reduce the broadening due to its insensitivity to the spatial variation and phase/gain changes. In addition, the low loss microring resonators in the passive platform effectively extend the optical length of the laser cavity due to the multiple roundtrips in the microring resonators [37]. The cavity photon lifetime for the hybridly integrated diode laser is increased, which leads to the greatly reduced Schawlow-Townes linewidth [38]. The two microring resonators also act as a wavelength filter. Through the thermo-optic effect, i.e., heating of the resonators resulting in the increment of the effective waveguide index and thereby the optical length of the resonator, the wavelength tuning is obtained [39]. The wavelength tuning range can be enhanced through Vernier effect [40].

Although silicon waveguides are capable of providing tight optical confinement and large thermal-optical effects, they are not suitable for the 1 μm wavelength band due to high absorption loss. For the 1.55 μm wavelength band, it is also not an ideal platform for the applications requiring high power CW light due to the two-photon absorption that limits the maximum light intensity. Silicon nitride has been widely utilized for integrated photonics to create passive optical components with high performance as a result of its low nonlinearity, high index contract with silica, very large transparency window and low

linear propagation loss. Narrow-linewidth hybrid lasers operating around 1.55 μm have been demonstrated using Si_3N_4 ring resonators and InP quantum-well RSOAs [24, 41, 42]. Besides the InP gain chip, the GaAs gain chip is also a good candidate for hybrid laser integration due to its higher wall plug efficiency, which is important for high power operation. Low water absorption near 1 μm is considered important for applications in sensing, free space communications, and biomedical systems. Diode lasers near 1 μm are also important for LiDAR, high power lasers [43] and seed sources to fiber lasers [44]. The emitting wavelength range of GaAs gain medium is around 750-1100 nm, where the silicon waveguide has high propagation loss. However, because of very large transparency window of Si_3N_4 (from 300 nm to several microns), the InP gain chip operating at 1.55 μm and GaAs gain chip operating at 1 μm can be hybridly integrated together into the same Si_3N_4-based platform with low loss.

In this chapter, we demonstrate chip-scale, narrow linewidth, hybridly integrated, dual-band diode lasers based on the InP/GaAs RSOA and Si_3N_4 external cavity. This design can provide on-chip narrow linewidth laser sources with wide wavelength tunability around 1.55 μm and 1 μm simultaneously for passive photonic integrated circuits. The performance of the InP-Si_3N_4 hybrid laser (i.e., output power, side mode suppression ratio, laser linewidth, wavelength tuning range) is comparable to the others demonstrated before [20, 45, 46]. To the best of our knowledge, the III-V/Si_3N_4 hybrid F-P laser working near 1 μm was first demonstrated in Ref. [47] through wafer bonding. But we demonstrate the stable single frequency lasing at 1 μm with narrow spectral linewidths and wavelength tunability in the hybrid platform for the first time. Dual-band

single frequency lasing on a single chip is potential to enable new applications in integrated nonlinear optics and provides a highly effective approach to difference frequency generation of 3-5 μm radiation for use in compact optical gas sensors [48]. Besides, high-power broadband laser sources enable technologies such as integrated spectroscopy systems [49] and wide band wavelength division multiplexing [50].

3.2 Laser design and fabrication

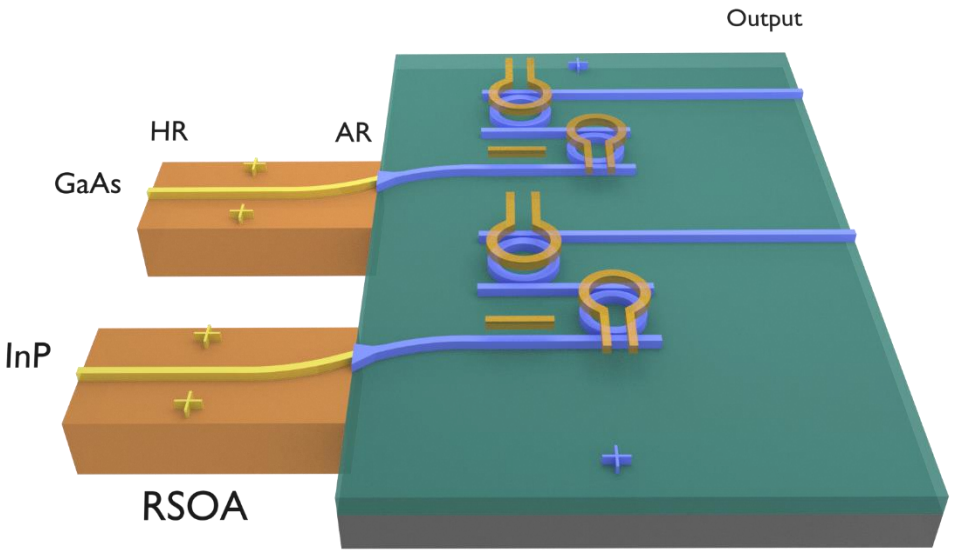

Figure 3.1: Schematic plot of the hybridly integrated diode laser.

Figure 3.1 shows the schematic plot of the hybridly integrated diode laser. It consists of two RSOAs (i.e., InP and GaAs gain chips) and a $Si_3N_4/SiO_2/Si$ chip. The buried oxide (BOX) layer is thick enough (4 μm) to prevent optical leakage from the

Si_3N_4 waveguide layer to the Si substrate. The RSOA has a high reflection (HR) coated back-facet with a 90% reflectivity and an AR coated front facet. Due to the large mode mismatch between the waveguides in the RSOA and Si_3N_4 chips, we use a well-designed spot size converter to efficiently couple the light between active and passive chips. The waveguide width at the input end of the converter is 5.9 μm, so the diode laser mode can be matched well with the input end of the converter. Then the waveguide is narrowed down to the width of the single mode waveguide. The total converter length is 50 μm. The detailed design is given in Ref. [51]. The minimal coupling loss of < 0.3 dB between the two chips is obtained through the 3D FDTD simulation. In our best samples, we achieve the experimentally measured coupling loss of less than 2 dB. Besides, the RSOA and Si_3N_4 waveguide are both angle-cleaved to eliminate the reflection at the interface between the RSOA and passive chip. The Si_3N_4-based external cavity is composed of double-ring micro-resonators with slightly different free spectral ranges (FSRs) acting as a wavelength filter and extended cavity. Figure 3.2(a) shows the simulated and measured transmission spectra of the double-ring filter around the 1.55 μm wavelength range. The radii for the two microrings are 51 and 54 μm, respectively. We observe excellent agreement between the simulation and experiment. A simple cleaved facet at the Si_3N_4 waveguide output port is utilized here to reflect the light back into the laser cavity, which can help to obtain the wide wavelength tunability due to its broadband back reflection. Figure 3.2(b) shows the scanning electron microscope (SEM) image of the cleaved facet indicating a smooth facet surface. The measured reflectivity of the cleaved facet is around 7.5%. The light is coupled into a lensed fiber for measuring the output of the laser at the

cleaved facet through a well-designed spot size converter. The width of the single mode silicon nitride waveguide for the lasing wavelength of 1.55 μm is set to be 900 nm and the height is 300 nm. The hybrid composite laser cavity consists of the RSOA, double-ring resonators, and input/output waveguides. The longitudinal modes of the entire hybrid cavity are defined by the total effective cavity length, while the mode selection is obtained by the two microring resonators with slightly different FSRs. The resonance of ring resonators is thermally tuned by micro-heaters to obtain wavelength tunability.

The passive chip fabrication process starts with a SiO_2/Si wafer where the SiO_2 cladding layer is about 4 μm thick. We deposit Si_3N_4 using Tystar Nitride LPCVD tool. The Si_3N_4 waveguides are patterned and etched using EBL and reactive ion etching (RIE) with a fluorine-based plasma chemistry, respectively. Then a SiO_2 cladding layer is deposited. In order to thermally tune the ring resonators, Chromium/Platinum (Cr/Pt) heaters are deposited and patterned over the resonators.

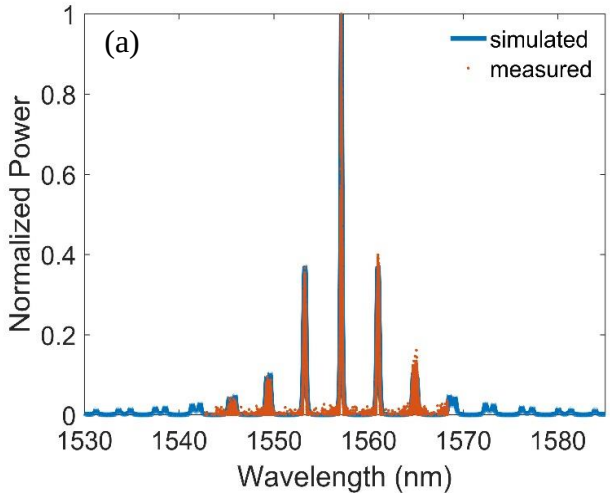

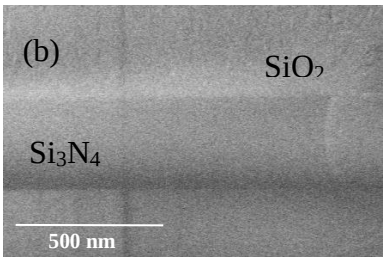

Figure 3.2. (a) Simulated and measured transmission spectra of the double-ring filter. (b) SEM image of the Si_3N_4 cleaved waveguide facet.

3.3 Experimental results of the InP-Si_3N_4 hybrid laser

Here we use active alignment to demonstrate the hybrid integration of the two RSOAs and passive chips for simplicity. To obtain the efficient control of the two RSOAs, they are placed at the two different sides of the Si_3N_4 passive chip, as shown in Ref. [35]. This configuration allows us to put each RSOA on an independent stage for accurate control of coupling with the passive cavity. The InP-Si_3N_4 and GaAs-Si_3N_4 hybrid lasers can operate at the same time. The laser light output from the InP and GaAs gain chips are detected from two different output ports through a lensed fiber separately. All the measurement results are obtained at room temperature with uncooled lasers. Figure 3.3 shows the experimental results of the hybridly integrated laser based on the InP RSOA gain chip. The L-I curve and current-voltage (I-V) for the laser is shown in Fig. 3.3(a). The threshold current is around 60 mA. The slope efficiency is 68 mW/A. The normalized output optical spectrum is shown in Fig. 3.3(b) (the pump current is set at around 100 mA). The single frequency lasing with ~52 dB side mode suppression ratio

(SMSR) is obtained by taking advantage of the Vernier effect between the two microrings. Since the resolution of optical spectrum analyzer (OSA) is inadequate to resolve the laser spectral linewidth, we use a delayed self-heterodyne (DSH) interferometer with a 10-km delay line to measure the laser spectral linewidth as shown in Fig. 3.3(c). Compared with the optical heterodyne detection method, the DSH approach does not require a reference laser with a narrower linewidth at a nearby frequency [52]. The red dots in Fig. 3.3(d) shows the measured RF-beat spectrum. A Lorentzian fit is shown by the blue line. An 18 kHz full width at half maximum (FWHM) laser linewidth is obtained. The linewidth of the hybrid laser is reduced mainly due to the increased cavity length and microring based delay-line filter. Figure 3.3(e) shows the superimposed spectra. The tuning range of ~46 nm is obtained. Coarsely tuning is obtained here when we thermally tune only one of the two microring resonators.

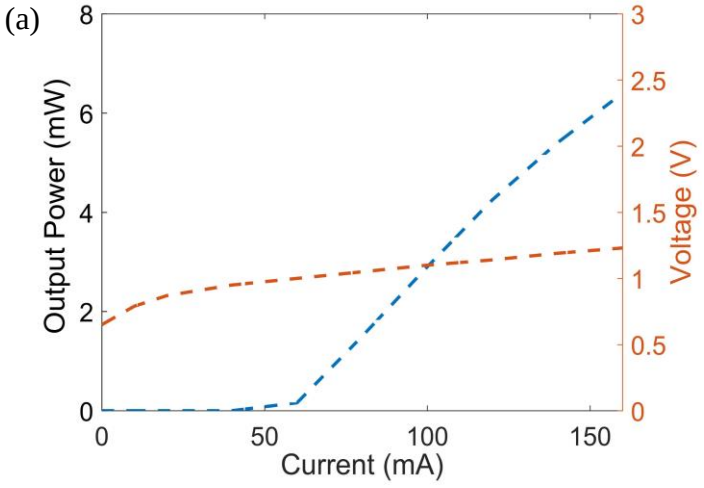

(b)

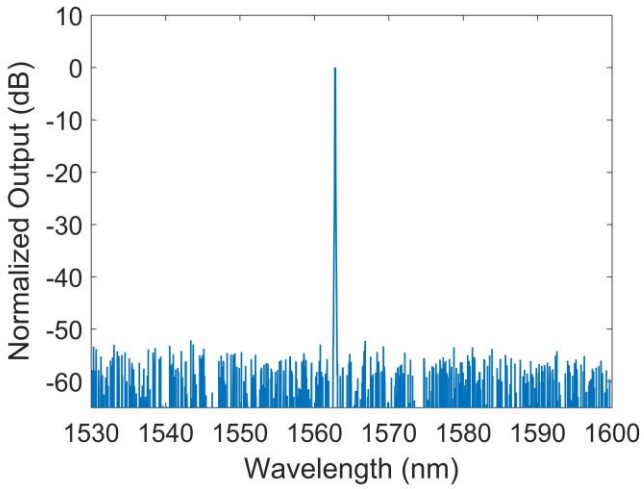
Normalized Output (dB)
10
0
-10
-20
-30
-40
-50
-60
1530 1540 1550 1560 1570 1580 1590 1600
Wavelength (nm)

(c)

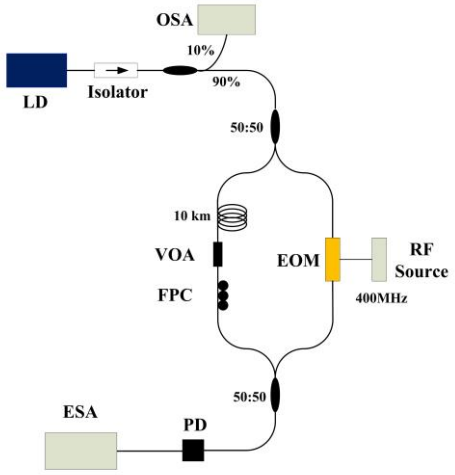
OSA
10%
90%
LD
Isolator
50:50
10 km
VOA
FPC
EOM
RF
Source
400MHz
50:50
ESA
PD

(d)

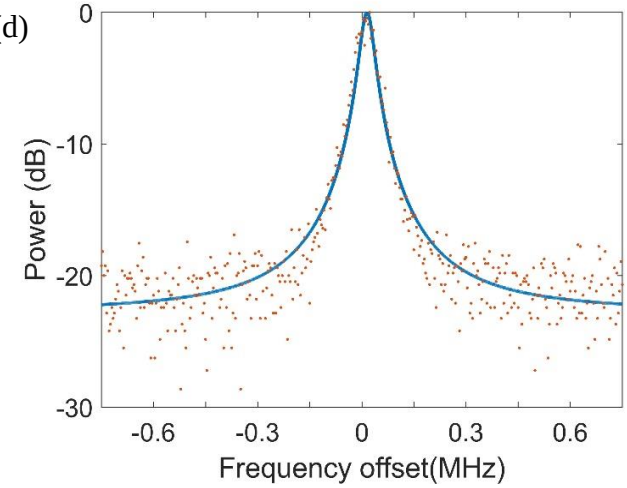
Power (dB)
0
-10
-20
-30
-0.6 -0.3 0 0.3 0.6
Frequency offset(MHz)

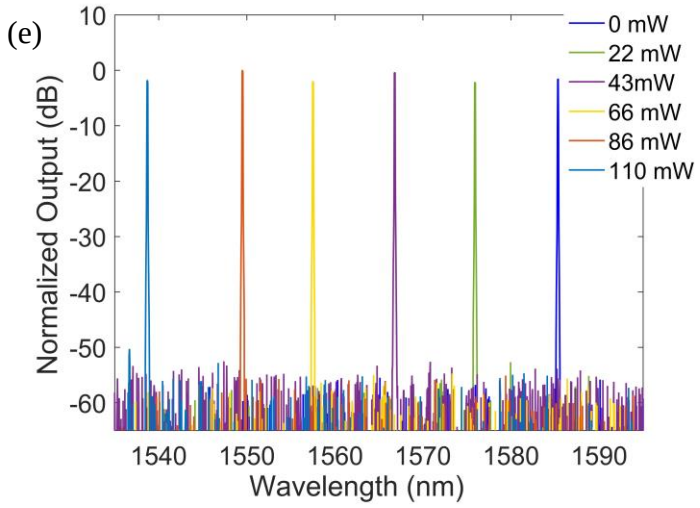

Figure 3.3. Experimental results of the InP-Si_3N_4 hybrid laser. (a) L-I curve (blue) and I-V curve (red). (b) Normalized output optical spectrum with the single frequency operation. (c) Delayed self-heterodyne experimental setup; OSA: optical spectrum analyzer; VOA: variable optical attenuator; FPC: fiber polarization controller; PD: photodiode; ESA: electrical spectrum analyzer; EOM: electro-optic modulator. (d) Recorded RF beat spectrum (red dots), the blue line shows a Lorentzian fit corresponding to a laser linewidth of 18-kHz. (e) Superimposed spectra when we thermally tune one of the two microresonators (the tuning range is ~ 46 nm).

3.4 Experimental results of the GaAs-Si_3N_4 hybrid laser

In addition to the InP gain chip, a GaAs gain chip is also integrated into the same hybrid platform due to the large transparency window of Si_3N_4. Figure 3.4 shows the experimental results of the GaAs-Si_3N_4 hybrid laser in the same chip. The radii of the two

microrings in the Si_3N_4 external cavity are 50 and 52 nm. Figure 3.4(a) shows the L-I curve and I-V curve for the laser. The threshold current is around 85 mA. The slope efficiency is 220 mW/A, which is higher than that of the InP-Si_3N_4 hybrid laser due to the higher photon energy for 1 μm, the higher internal quantum efficiency and the lower internal loss [1]. The output power of above 20 mW can be obtained from the output port. From the normalized output optical spectrum shown in Fig. 3.4(b) (the pump current is set at around 150 mA), it is found that the single frequency lasing is also obtained here. The SMSR is ~46 dB. As shown in Fig. 3.4(c), the FWHM laser linewidth is 70 kHz which is broader than that of the InP-Si_3N_4 hybrid laser. The possible reasons include the higher loss of the Si_3N_4 waveguide at the wavelength of 1 μm and the larger linewidth enhancement factor of GaAs gain medium. For the 1.55 μm laser linewidth measurement, SMF-28e is used as the fiber delay line. All other components are telecom compatible products. For the 1 μm laser linewidth measurement, it is best to use HI1060 as the fiber delay line. The other components (i.e., isolator, couplers, VOA, FPC, EOM) should be designed for the 1 μm band. Figure 3.4(d) shows the superimposed spectra when one of the two microresonators are thermally tuned. The tuning range is 38 nm. When we thermally tune the microring resonator, the resonance peaks of the two microring resonators may not be completely overlapped, which results in the extra loss in the laser cavity, thereby the power fluctuation.

(a)

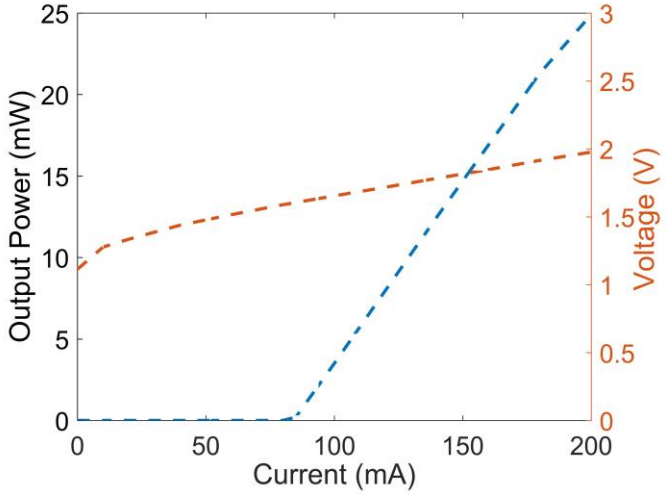
Output Power (mW)
Voltage (V)
Current (mA)
0
5
10
15
20
25
0
0.5
1
1.5
2
2.5
3
0
50
100
150
200

(b)

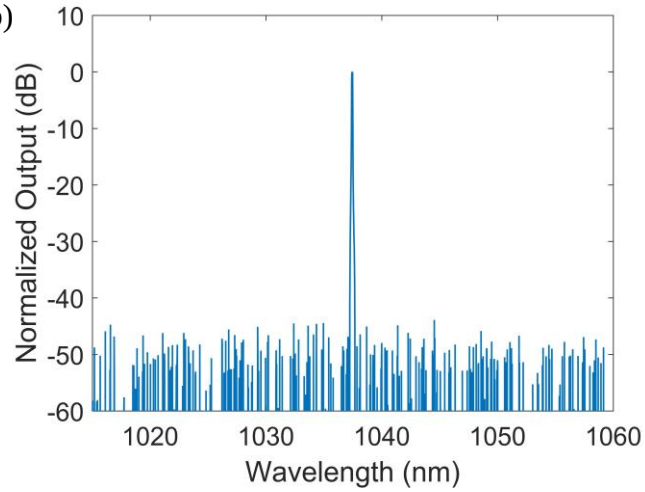
Normalized Output (dB)
Wavelength (nm)
10
0
-10
-20
-30
-40
-50
-60
1020
1030
1040
1050
1060

(c)

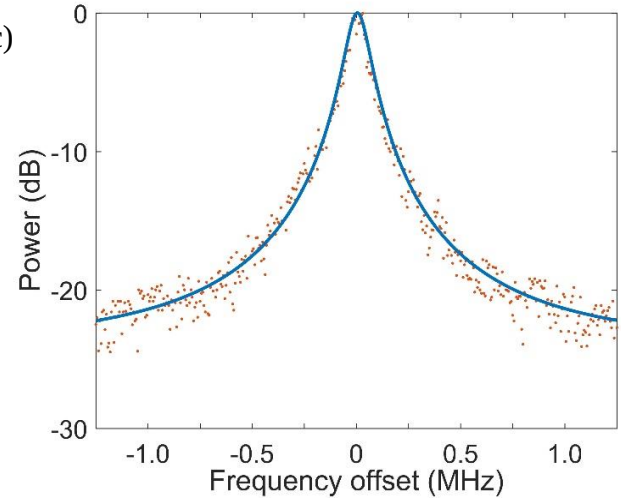
Power (dB)
Frequency offset (MHz)
0
-10
-20
-30
-1.0
-0.5
0
0.5
1.0

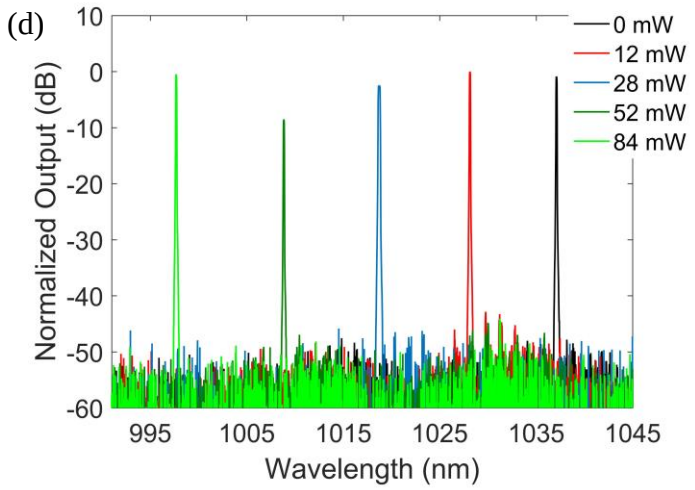

Figure 3.4. Experimental results of the GaAs-Si_3N_4 hybrid laser. (a) L-I curve (blue) and I-V curve (red). (b) Normalized output optical spectrum. (c) Recorded RF beat spectrum (red dots), the blue line shows a Lorentzian fit corresponding to a laser linewidth of 70-kHz. (d) Superimposed spectra when we thermally tune one of the two microresonators.

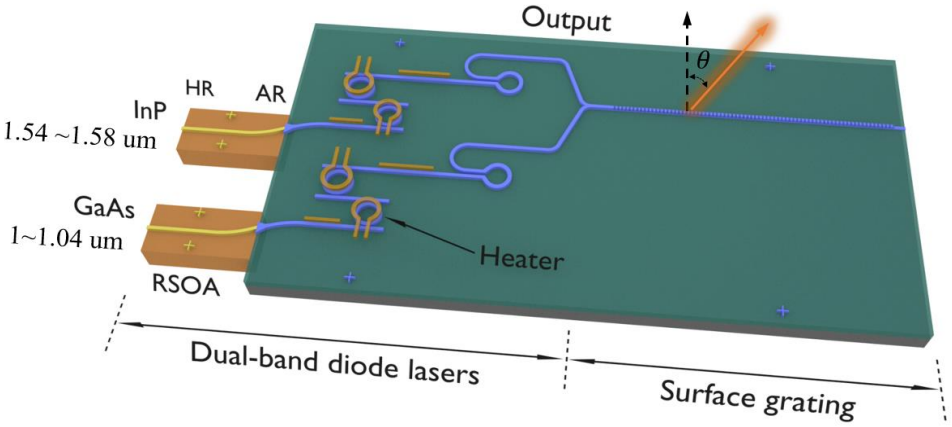

Figure 3.5. Schematic plot of the integrated beam steering hybrid system.

3.5 Experimental results for the beam steering

Narrow linewidth, tunable lasers are well suited for numerous applications in coherent optical communications, optical sensing, LiDAR and spectroscopy [53]. Here shows one potential application in beam steering [54]. As shown in Fig. 3.5, the tunable dual-band diode laser combined with a waveguide surface grating can provide beam steering by tuning the wavelength of the light signals [55]. The beam propagation direction can be tuned when the laser wavelength is changed [56]. The beam emission angle θ is indicated by Eq. (3.1):

$$\sin\theta = \frac{n_{eff}\Lambda - \lambda_0}{\Lambda} \tag{3.1}$$

where n_{eff} is the effective index of the grating. Λ_0 is the wavelength. Λ is the grating period. θ is the angle of the output beam with respect to the axis orthogonal to the chip plane.

Figure 3.6 shows the preliminary experimental results of the beam steering for the tunable dual-band diode lasers. Figure 3.6(a) shows the far-field infrared (IR) image. The FWHM beam width is measured to be ~0.4 degree. Figure 3.6(b) shows the beam steering results of the tunable dual-band diode lasers working at ~1.55 μm and ~1 μm.

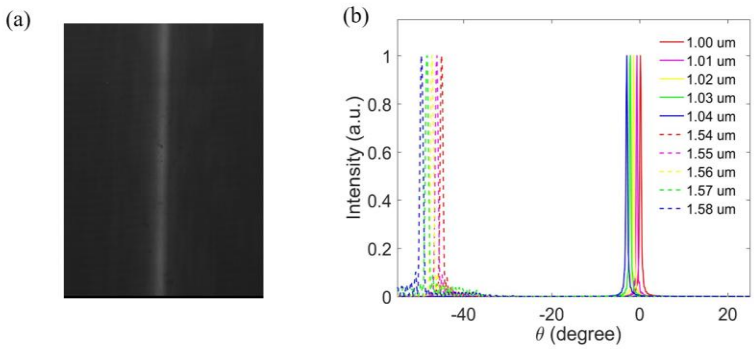

Figure 3.6. Experimental results of the beam steering for the dual-band diode lasers. (a) The far-field IR image of the emission from surface grating. (b) The beam steering results of the tunable dual-band diode lasers working at 1.54 ~ 1.58 μm and 1 ~ 1.04 μm.

The beam steering range of the waveguide grating is limited by the wavelength tuning range of the single laser source, which is around several tens of nm. To increase the beam steering range, multiple laser sources with different gain materials working at different wavelength bands must be used [57, 58]. By integrating multi-band laser sources on a single photonic chip, an extremely broadband tunable laser source can be obtained for integrated wide-angle beam steering. Here we use edge-coupled hybrid integration to create multi-band tunable laser sources on a single chip [59]. As for the passive components, we use Si_3N_4 due to its high-power compatibility, low nonlinearity, high index contract with silica, very large transparency window (from 300 nm to several microns) and low linear propagation loss. The hybrid III-V/Si_3N_4 platform enables the

integration of multi-band diode lasers to create a very broadband laser source on a single silicon chip, which is critical for fully integrated, wide-angle beam steering.

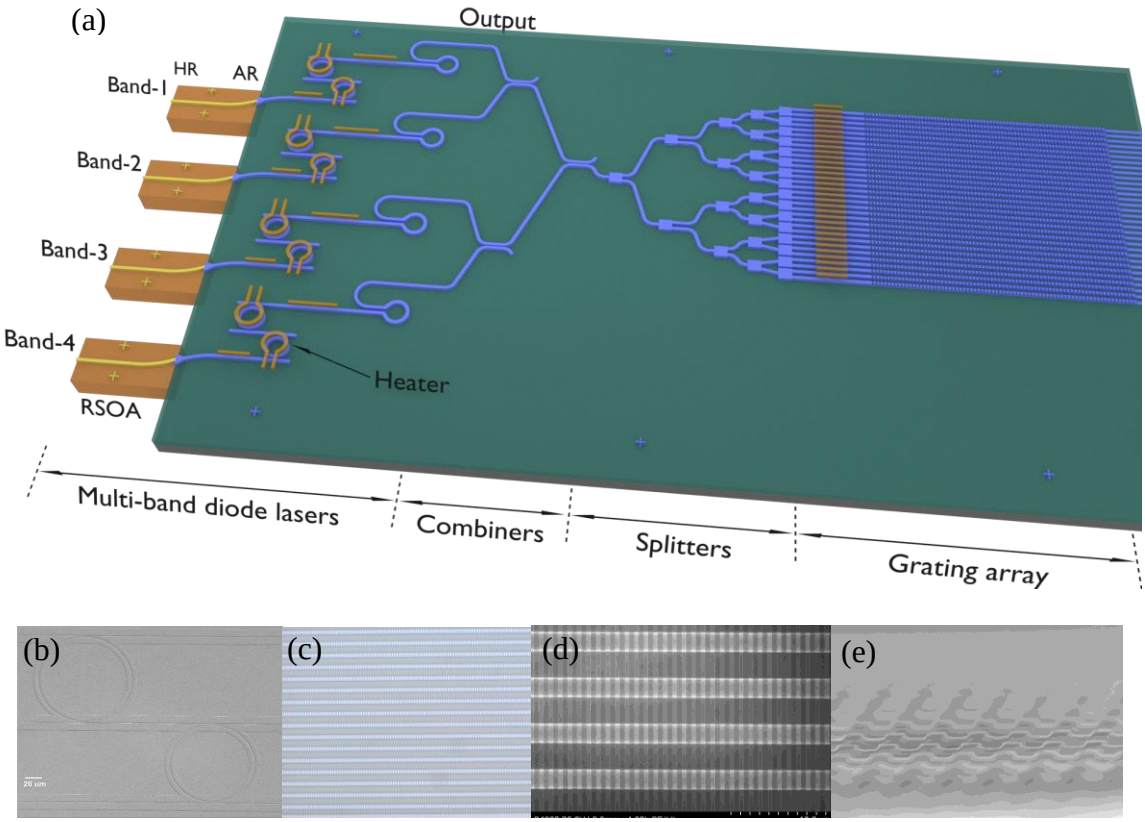

Figure 3.7. (a) Schematic plot of the integrated beam steering hybrid system. (b) The SEM image of the coupled ring resonators. (c) The microscopic image of the optical phased arrays. The SEM images of the optical phased arrays of the top view (d) and side view (e).

Here, we propose on-chip, fully integrated, wide-angle beam steering system by hybridly integrating multi-band gain chips in both GaAs and InP materials, microring based delay-line filters, spectral beam combiners, phase tuners and a waveguide grating

array. Figure 3.7(a) shows the schematic plot of the integrated beam steering hybrid system. It consists of multi-band external cavity diode lasers in different gain materials, beam combiner and a waveguide grating array. Each external cavity diode laser is realized by hybridly integrating a gain chip with a HR coated back-facet and an AR coated front facet, two ring resonators with slightly different free spectral ranges acting as a wavelength filter and a Sagnac loop mirror. The light from different diode lasers is first coupled into a single Si_3N_4 waveguide through broadband beam combiners. The light is then split by a tree-like splitter array into sixteen 2 μm wide parallel waveguides, spaced 4 μm apart. A diffraction grating is shallowly etched on top of each waveguide, characterized by a period of 1 μm, a duty cycle of 50% and etching depth of 100 nm. The total length of each grating coupler is 300 μm. Figure 3.7(b) shows the SEM image of the fabricated microring-based spectral filter (top view). Figures 3.7(c)-(e) show the microscopic image and SEM images of the waveguide surface grating array.

For now, we only experimentally demonstrated the tunable dual-band diode lasers working at ~1.55 um band and ~1 um band as shown in Fig. 3.5. But if we integrate multiple gain chips into the same Si_3N_4 platform, the wavelength of the laser source can be tuned in a wide range between 1 um and 1.6 um. Figure 3.8 shows the beam steering result of the waveguide grating which is obtained via FDTD simulation. Figure 3.8(a) shows the beam steering result of the waveguide grating. The steering range of > 50° is obtained if the wavelength of laser sources can be tuned continuously between 1 um and 1.6 um. The far field profile of a waveguide grating array is shown in Fig. 3.8(a).

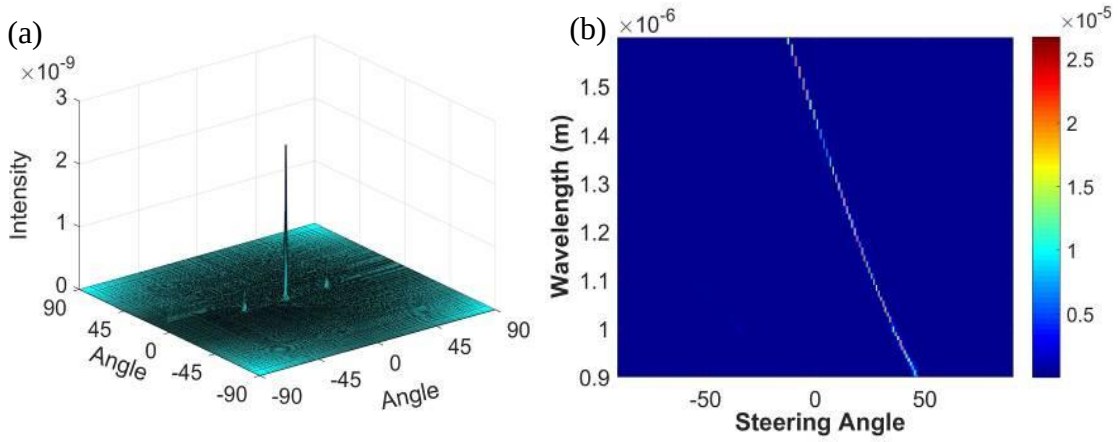

Figure 3.8. FDTD simulation results for the waveguide grating array. (a) Far-field profile. (b) The variation of emitting angle as a function of the wavelength.

3.6 Conclusion

In conclusion, we have demonstrated the hybrid integration of a low-loss, passive Si_3N_4 external cavity with two RSOAs simultaneously in silicon photonics platform to obtain the ultra-narrow laser linewidth and wide wavelength tunability. The hybrid integration allows multiple active chips with different types of gain media to be integrated easily in the platform at the same time. In addition to the InP chip operating around 1.55 μm, a GaAs chip at 1 μm is also integrated in the same hybrid platform. Single frequency lasing at 1.55 μm and 1 μm has been demonstrated simultaneously on a single chip with the spectral linewidths of 18 kHz and 70 kHz, side mode suppression ratio of 52 dB and 46 dB, and tuning range of 46 nm and 38 nm, respectively. The dual-band single frequency diode lasers have a great potential for a wide range of applications in integrated nonlinear optics and quantum optics. Besides, we demonstrate the beam

steering using the dual-band diode laser and waveguide surface grating. We also propose the hybrid integration of multi-band external cavity diode lasers with a waveguide grating array in silicon nitride platform to obtain the wide-angle beam steering, which is desired for advanced applications such as remote sensing and LiDAR.

CHAPTER FOUR

INTEGRATED BEAM COMBINED LASERS

4.1 Introduction

The emerging applications of PICs in LiDAR, microresonator based frequency comb, and photon pair generation require single frequency, high power, narrow linewidth, tunable semiconductor lasers. Although the hybridly integrated diode lasers demonstrated in the chip-scale platform can provide narrow linewidth and wavelength tunable operation, the output power of the hybridly integrated diode lasers is still limited.

To scale up the output power, coherent beam combining (CBC) can be used to overcome this limitation [25]. However, the CBC laser system usually requires optical fibers [60, 61] or free-space components such as lens [62, 63], external cavities [64, 65], diffraction gratings [66] and photonic crystals [31, 35]. In this chapter, by manipulating mirror losses at different output ports of coupled Fabry-Perot cavities, we proposed and experimentally demonstrated an integrated coherently combined laser system in the InP-Si_3N_4 hybrid platform. In our demonstration, we eliminate the need of fiber and free space based optical components. Our miniaturized CBC laser system in the InP-Si_3N_4 hybrid platform not only is important for creating an integrated high-power laser source for passive PICs but also provides a chip-scale platform to study the phase locking dynamics in a laser system with coupled cavities.

4.2 Beam combining techniques in photonic integrated circuits

There are two main methods for obtaining beam combining: one is incoherent (wavelength) beam combining and the other one is coherent beam combining. In an incoherently combined laser array system, all the emitters have different wavelengths with random phase relationship. In a coherently combined laser array system, there is constant phase difference between emitters. All the emitters have the same wavelength. Therefore, here we only focus on the coherent beam combining technique.

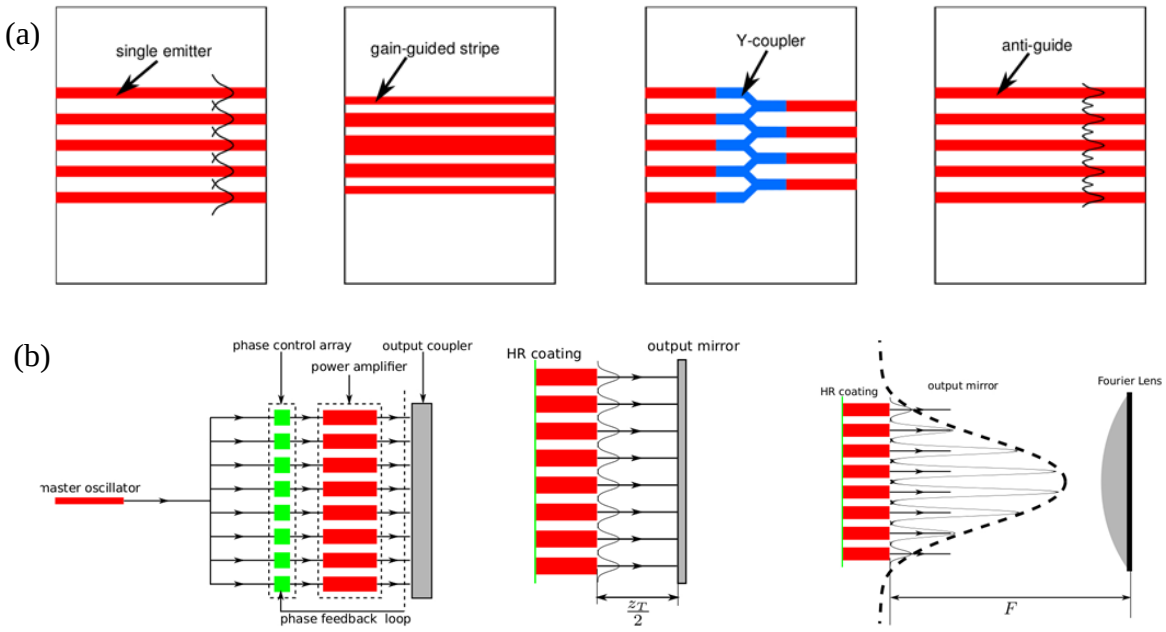

Figure 4.1: (a) Monolithic coherent beam combining (evanescently coupled laser arrays, chirped and Y-coupled laser arrays, leaky wave coupled laser arrays). (b) Coherent beam combining with external components (master oscillator power amplifier arrays, talbot cavity laser arrays, self-Fournier cavity laser arrays).

Depending on if external optical components are needed, coherent beam combining of laser arrays is divided into two categories. As shown in Fig. 4.1(a), the first category can be monolithically implemented, including: i) evanescently coupled laser arrays, where multiple closely-spaced lasers are coupled to form a super transverse mode; ii) chirped and Y-coupled laser arrays; and iii) leaky wave coupled (anti-guided) laser arrays. The main problem with these previously demonstrated coherent arrays is that they provide poor modal discrimination and have limited scalability.

The second category, which requires external optical components, includes: i) master oscillator power amplifier (MOPA) arrays; ii) Talbot cavity laser arrays; iii) self-Fournier cavity laser arrays, as shown in Fig. 4.1(b). These systems usually provide better performances. But since external components and/or accurate phase control are needed, these systems are always complex, bulky, and expensive.

Compared to the first laser array category, the second category can provide much higher modal discrimination. The self-Fournier cavity offers better performance than the Talbot cavity. The feedback is more uniformly distributed in the Talbot cavity, while the feedback to the central element is always the strongest in the self-Fournier cavity, which results in stronger modal discrimination for the self-Fournier cavity. The in-phase supermode in the self-Fournier cavity usually has the lowest loss. Besides, the self-Fournier cavity also suffers less from the edge diffraction loss due to the additional objective lens. Both approaches have some disadvantages. The high modal discrimination

requires small fill factors, which lead to side lobes in the far field and reduce the beam combining efficiency.

We demonstrate an N×N coupler based interferometric array to replace the external cavity in free space CBC systems, as shown in Fig. 4.2. We create a chip-scale CBC system by using the hybrid integration method discussed in Chap. 2. The diode laser array (RSOA) is directly coupled to the coupler array. The key here to realize coherent beam combining is the tree-like passive external cavity. These tree-like coupled cavity has been proposed and demonstrated in a fiber-based laser system. In contrast, adjacent RSOAs in our design are coupled through a specially designed 50:50 coupler. One of the output ports is made to be total lossy by narrowing down the width of the waveguide. Only a single end in the passive CBC cavity can provide optical feedback for lasing through a distributed Bragg reflector (DBR) reflector or cleaved facet. The output wavelength can be tuned by changing the resonance wavelength of the DBR reflector. The supermode supported by the external cavity can be obtained by solving the eigenvalue problem of the transfer matrix of the CBC cavity, as shown in Fig. 4.2(c) and discussed next section. The modal properties of the supermodes are determined by the geometric parameters of the CBC cavity. Then, the modal discrimination between the supermodes supported in the coupler array can be greatly increased. Therefore, the maximum modal discrimination for coherent beam combining can be achieved by selectively controlling the optical feedback at each coupler output port.

(a)

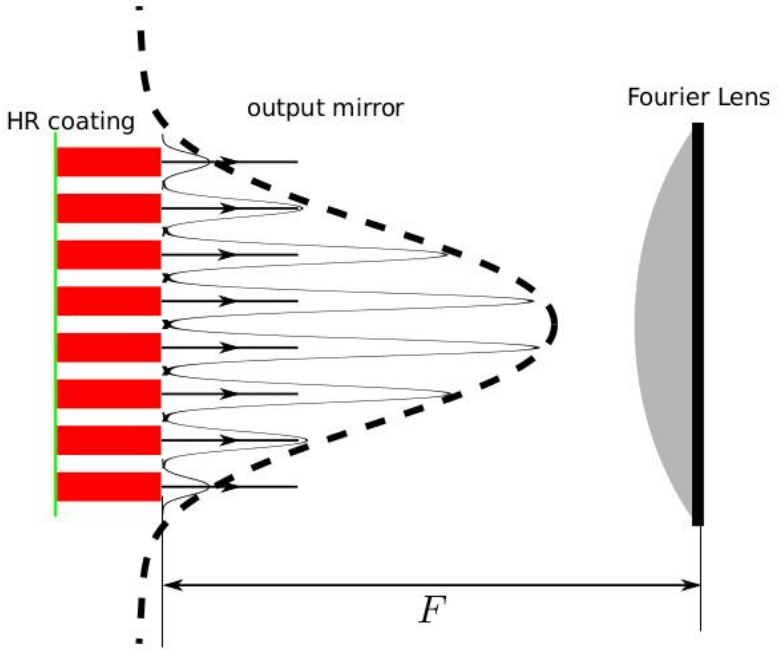

(b)

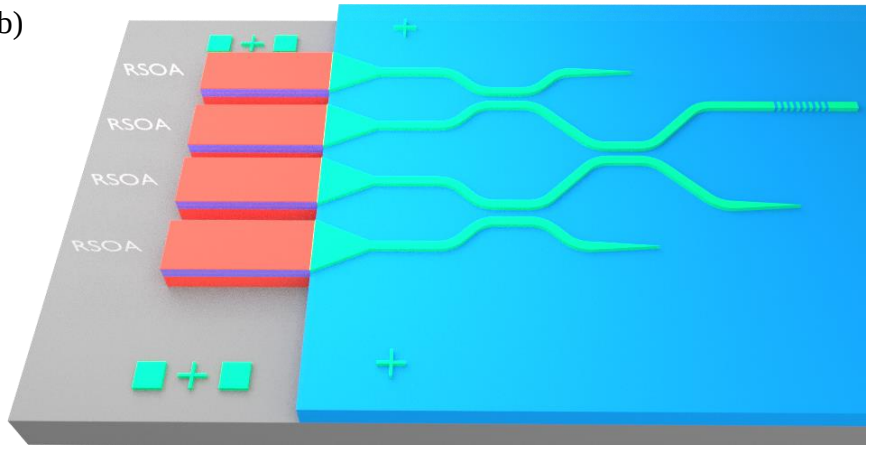

(c)

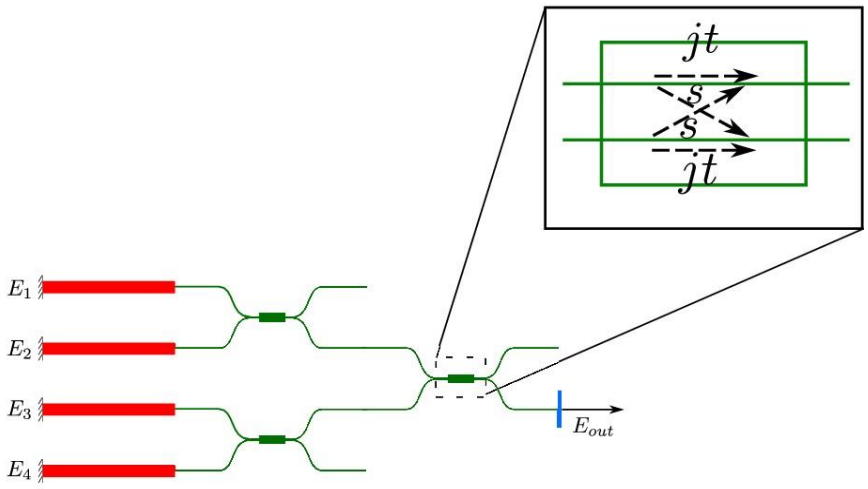

Figure 4.2: The external cavity in the above beam combining system can be replaced by a coupler array in PICs. (a) Self-Fournier cavity laser arrays. (b) Schematic plot of a hybridly integrated CBC laser array system. (c) a 2×2 coupler with a transfer function.

For the 3 dB coupler design, multiple mode interferometers (MMI) or directional couplers (DC) are commonly used. But the MMI may cause unwanted back reflection to the laser array. For the DC, the power splitting ratio often has strong wavelength dependence due to the waveguide dispersion. Thus, we choose the adiabatic coupler design. The 3 dB adiabatic coupler has the 50% power splitting ratio over a broad range of wavelengths and provides the great fabrication tolerance and reproducibility.

Before we demonstrated the CBC of four gain chips shown in Fig. 4.2. We first need to demonstrate that the beam combing of two gain chips can be obtained, so that we can prove that our method is feasible.

4.3 Integrated beam combining of two gain chips

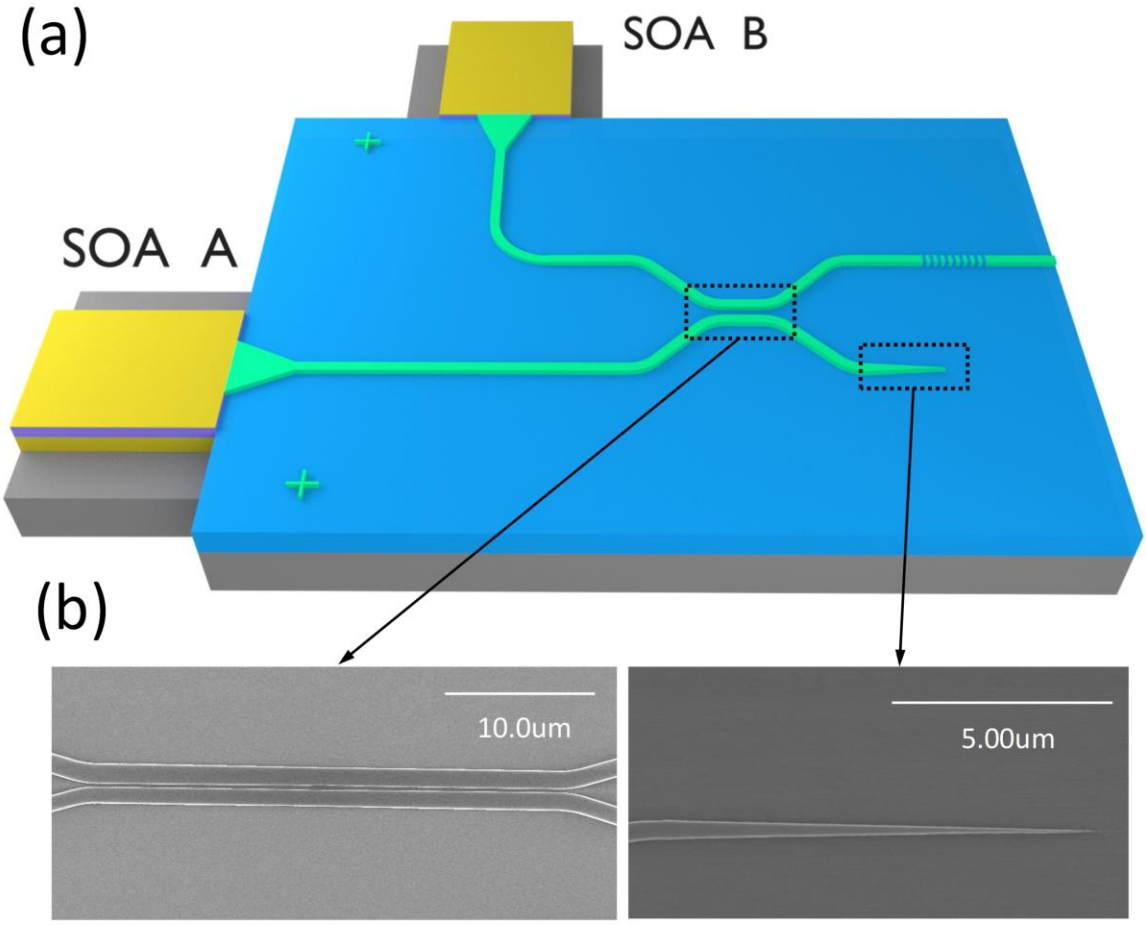

Figure 4.3: (a) Schematic plot of a hybridly integrated chipscale CBC laser system with two gain chips. (b) SEM images of the fabricated passive CBC cavity.

Figure 4.3(a) presents the schematic plot of the coherently combined laser system based on the hybrid integration approach. It consists of two InP-based RSOAs, and a

$Si_3N_4/SiO_2/Si$ chip where the SiO_2 cladding layer is thick enough (4 μm) to prevent optical leakage from the Si_3N_4 waveguide layer to the Si substrate. The length of RSOA is 1 mm. It has a HR coated back-facet with a 90% reflectivity. The RSOA front facet is AR coated. The gain ripple of the RSOA is less than 1 dB across a 40 nm range near 1550 nm. In the CBC cavity design, the two RSOAs (A and B) are coupled by a 50:50 broadband directional coupler. The mode converter is used to improve the coupling efficiency between the gain chip and passive chip. One of the coupler output ports is made to be lossy by narrowing down the waveguide width as shown in Fig. 4.3. The other output port can provide optical feedback for lasing through a broad-band reflector, i.e., a DBR reflector or a cleaved facet. Coherent combining of the two RSOAs is obtained by the extra mirror loss introduced at the output port. The width of the single mode silicon nitride waveguide is set to be 800 nm and the height is 300 nm. The gap between the waveguides at the coupling region is set to be 300 nm. Figure 4.3(b) also shows the SEM images of the fabricated CBC cavity.

The passive chip fabrication is summarized here. A 300-nm-thick Si_3N_4 is deposited on a SiO_2-on-Si wafer using a Tystar Nitride LPCVD tool. To pattern the Si_3N_4 layer, a JEOL JBX-9300FS EBL system is used with ZEP520A (by Zeon cooperation) as the e-beam resist. Next, the pattern is transferred to the Si_3N_4 layer using plasma etching with a CF_4/CHF_3 gas mixture in an Oxford Endpoint reactive ion etching machine. After the resist is removed, a 2-μm-thick SiO_2 is deposited on the Si_3N_4 layer using plasma-enhanced chemical vapor deposition process.

4.4 Modal analysis of the CBC cavity with two gain chips

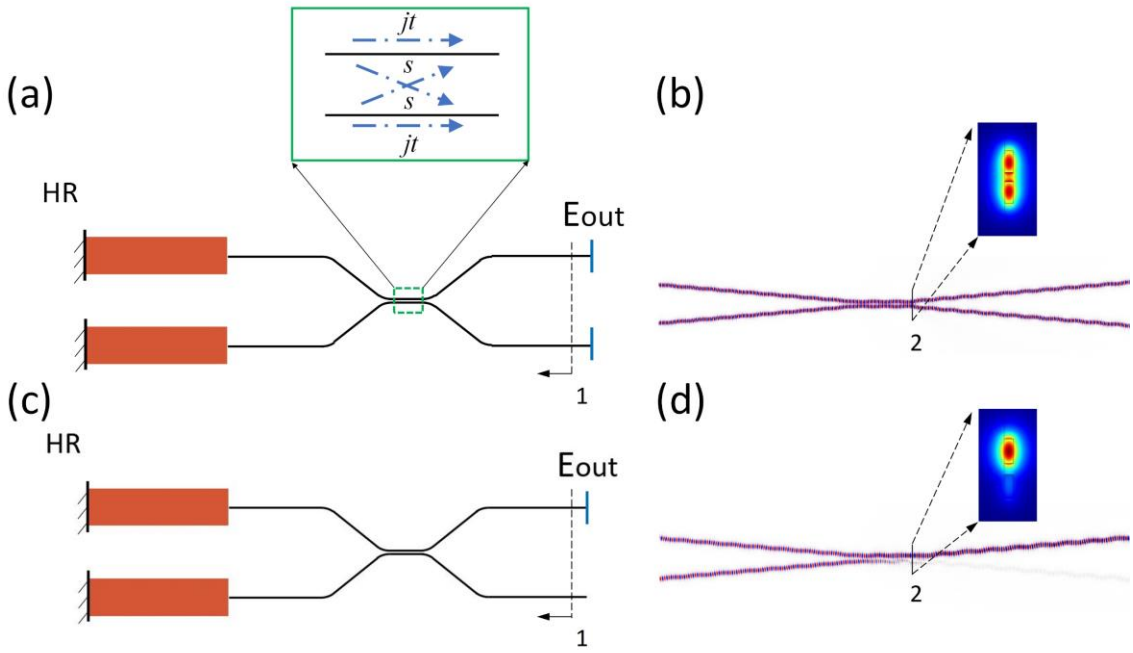

Figure 4.4: Schematic plot and FDTD/FEM simulation results of the combined laser cavities in the InP-Si_3N_4 platform without the extra loss (a, b) and with the extra loss (c, d).

The modal analysis of two types of coupled cavities in the InP-Si_3N_4 platform is performed by a transfer matrix method [42]. As shown in the schematic plot in Figs. 4.4(a) and (c), each system design consists of two gain chips (i.e., RSOAs) at the left side and a 3 dB broadband coupler at the right side. The interface reflection between the gain element and coupler is assumed to be zero. Thus, each composite cavity includes two groups of end facets acting as the feedback mirrors: one is the left end facets of the gain elements and the other one is the right end facets of the coupler output ports. Figure

4.4(a) shows the combined laser cavity design without the extra loss added at one of the output ports, which means that the mirror losses at the two coupler output ports are the same (symmetric). Figure 4.4(c) shows the CBC cavity design where one of the coupler output ports is made to be lossy, so that the asymmetric mirror losses are introduced. Here, we assume that the two gain elements work at the same resonance frequency. The cavity supermodes can be obtained by solving the eigenvalue problem of the overall transfer matrix of the composite cavity. The transfer function of the 3 dB coupler shown in Fig. 4.4 is described by a matrix as:

$$\begin{bmatrix} jt & s \\ s & jt \end{bmatrix} \tag{4.1}$$

where t and s are described in the inset of Fig. 4.4(a), and they should satisfy $|t|^2 + |s|^2 = 1$ ($t = s = 1/\sqrt{2}$ for a 3 dB coupler). Starting from position 1 (shown in Figs. 4.4(a) and (c)), the round-trip matrix for the light wave propagating in the cavity can be expressed as:

$$X = R_2 A^* S R_1 S A \tag{4.2}$$

$$A = \begin{bmatrix} jt & s \\ s & jt \end{bmatrix} \qquad S = \begin{bmatrix} e^{j\phi_1} & 0 \\ 0 & e^{j\phi_2} \end{bmatrix} \qquad R_1 = \begin{bmatrix} 1 & 0 \\ 0 & 1 \end{bmatrix} \tag{4.3}$$

$$R_2 = \begin{bmatrix} r & 0 \\ 0 & r \end{bmatrix} \quad or \quad R_2 = \begin{bmatrix} r & 0 \\ 0 & r_t \end{bmatrix} \tag{4.4}$$

where *A* is the transfer matrix of the 3 dB coupler, *S* is the phase change in each gain element, *R1* and *R2* are the reflection matrices of the left and right end facets, and the operator * denotes the complex conjugate. In the following analysis, we assume the left end mirrors have perfect reflectivity. *R* is set to be 1/3 that is the estimated reflection coefficient at the interface between a Si_3N_4 waveguide and air. R_t is set to be 0.02 that is the estimated reflection coefficient at the lossy port. To support a supermode, the system should be able to reproduce the electric field *E* after one round trip, which means the following equation should be satisfied:

$$XE = \mu E \tag{4.5}$$

where μ is the eigenvalue of *X* and *E* is the eigenvector. Each pair of μ and *E* corresponds to a supermode supported by the coupled cavities. The eigenvector is the field distribution at the output ports and eigenvalue μ is the associated modal gain. There are two elements in the eigenvector that correspond to the electric field amplitudes at the position 1 shown in Fig. 4.4. For the cavity without the extra loss shown in Fig. 4.4(a), if the phase change in the gain elements is the same, the nonzero eigenvalues and the corresponding eigenvectors are shown as follows:

$$\mu_{a1} = 1/3; \qquad |E_{a1}| = [1 \quad 0] \tag{4.6}$$

$$\mu_{b1} = 1/3; \qquad |E_{b1}| = [0 \quad 1] \tag{4.7}$$

Since the two eigenvalues are the same, the modal discrimination between the two eigenmodes is zero, which means the two supermodes will be induced at the same time. There will be the light emitting from both two output ports. This can also be demonstrated by the FDTD simulation results shown in Fig. 4.4(b). The inset shows the modal profile near the right end of the coupling region (position 2) through the FEM analysis (COMSOL). The optical field is evenly distributed at the two waveguides.

$$\mu_{a2} = 1/3; \qquad |E_{a2}| = [1 \quad 0] \tag{4.8}$$

$$\mu_{b2} = 0.02; \qquad |E_{b1}| = [0 \quad 1] \tag{4.9}$$

For the CBC cavity design in Fig. 4.4(c), the two eigenvalues are different, as shown in Eqs. (4.8) and (4.9). The modal discrimination between the two eigenmodes becomes much larger. This means that only the supermode with the higher modal gain will be selected in the CBC cavity for lasing. The constructive interference occurs at the output port with the mirror feedback and the destructive interference occurs at the other output port. The supermode selection leads to the coherent combining of the two gain elements at the left side. This is also demonstrated by the FDTD analysis in Fig. 4.4(d). The finite element method (FEM) analysis in the inset shows the mode profile of the preferred lasing mode. Therefore, though there is an extra loss introduced into the laser cavity, the two RSOA gain chips can be coherently combined without compromising the laser performance.

4.5 Measurement results for the coupling ratio of the coupler is 50:50

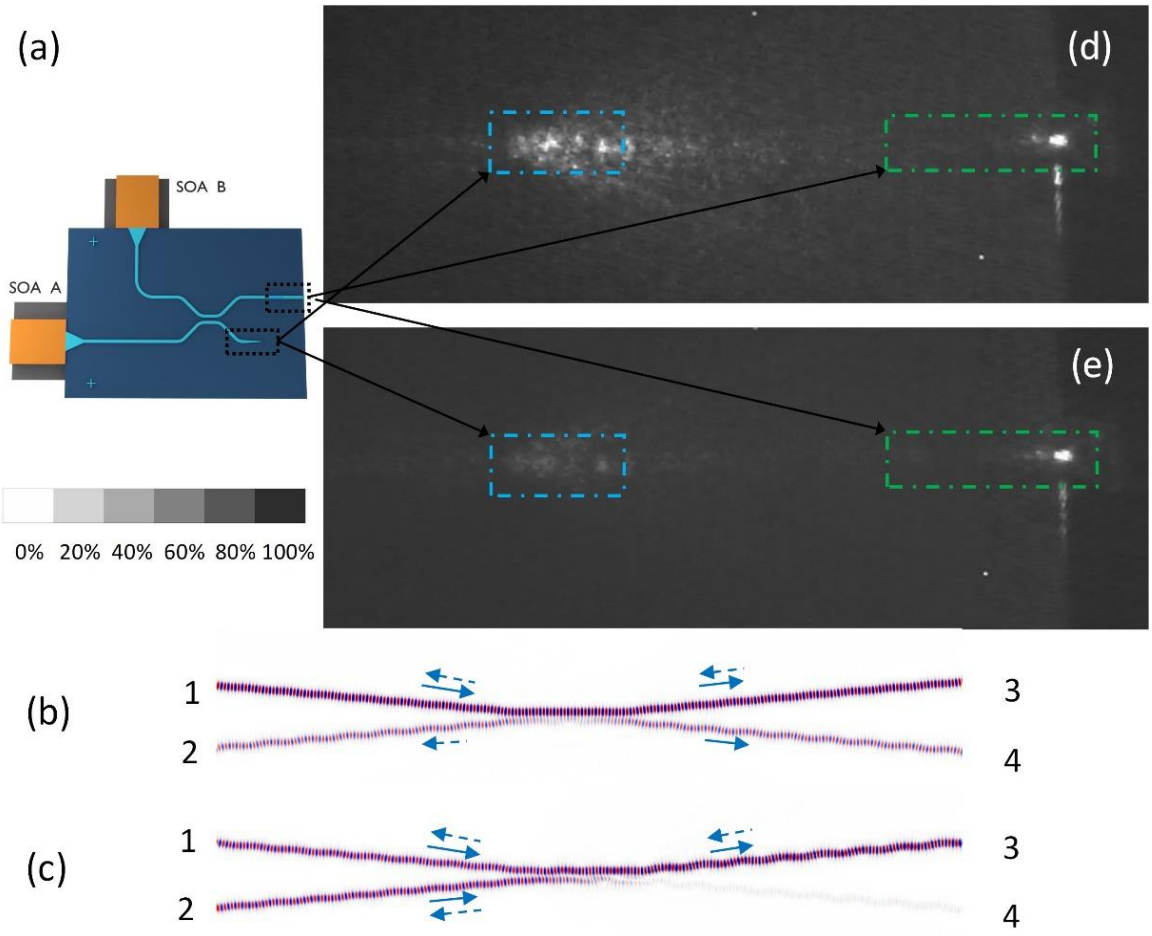

Figure 4.5: (a) Schematic plot of the hybridly integrated CBC laser system; FDTD simulation results and near field IR images (top-view) of the coherently combined lasers if only one RSOA is turned on (b) and (d). both two RSOAs are turned on at the same time (c) and (e). The grayscale bar shows the relative grey value.

We use active alignment method to demonstrate the hybrid integration of two RSOAs and a passive cavity. The RSOA is directly coupled to the passive waveguide through a spot-size converter. Figure 4.5(a) shows the schematic plot of the hybridly integrated CBC laser system. If only one RSOA (i.e., RSOA B) is turned on, the emitted light will be equally coupled to two output ports of the coupler. Figure 4.5(b) shows the power flow at the coupling region through FDTD analysis. The light signal is injected from port 1 (RSOA B) and is coupled into port 3 and 4 evenly. Then it is reflected back into the coupling region at port 3 through a broad-band reflector. Since RSOA A is not turned on and port 4 is the lossy output port, the light transmitted to port 4 and 2 dissipates completely. The extra loss at these two output ports for one round trip is 6 dB. Figure 4.5(d) shows the top-view near field IR image. The green line area corresponds to the Si_3N_4 waveguide with the cleaved facet, while the blue line area corresponds to the lossy output port of the coupler. As shown in the near field IR image, there is intense light scattered from the blue line area. Then, the two RSOAs are turned on at the same time with the similar injection currents to optimize the combining efficiency. If the two RSOAs are coherently combined and in-phase, they will constructively interfere at port 3 and destructively interfere at port 4 as shown in Fig. 4.5(c). This exactly matches our measurement results, as shown in Fig. 4.5(e). From the near field IR image, we can find that the intensity of the scattered light from the lossy output port of the coupler is greatly suppressed, while the output power obtained at the cleaved facet remains the same with the single RSOA operation. The ratio between the brightness of port 4 in Fig. 4.5(d) and

the one in Fig. 4.5(e) is ~9. The results in Fig. 4.5 demonstrate that the two lasers are coherently combined through the passive CBC cavity.

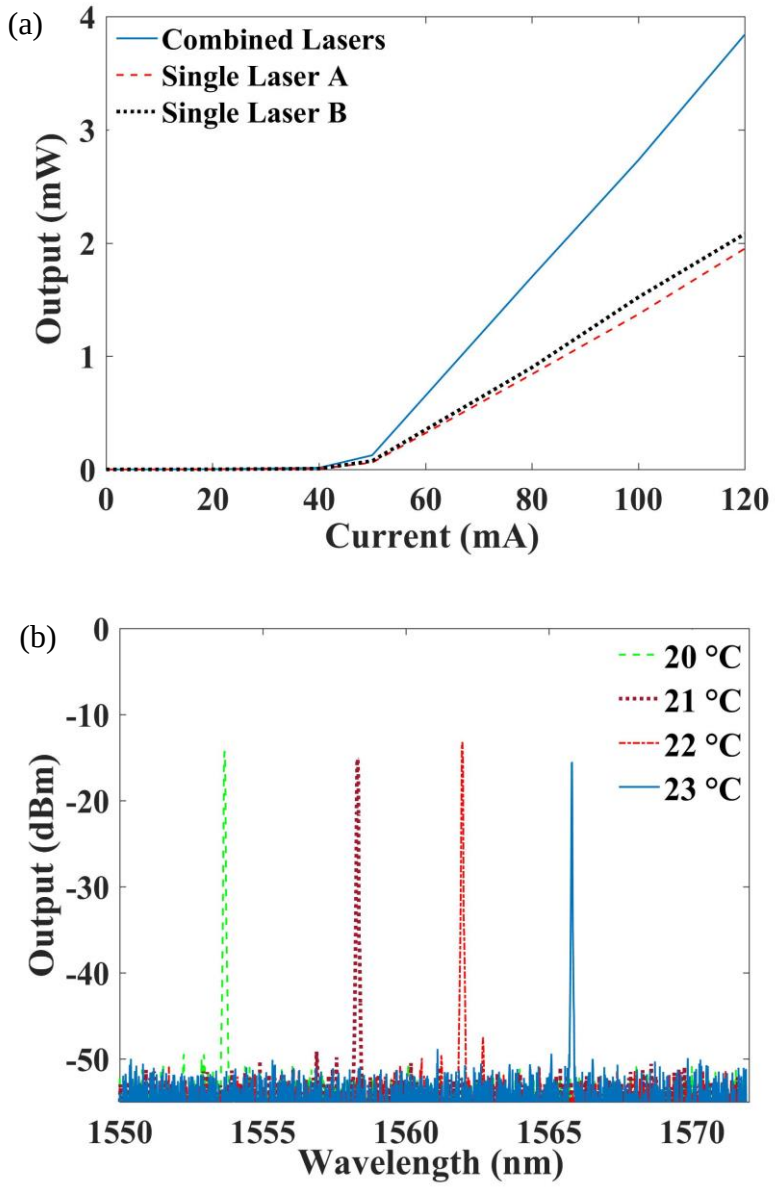

Figure 4.6: L-I curves (a) and optical spectra (b) of the coherently combined laser system.

Figure 4.6(a) shows the L-I curves of the hybridly combined lasers and the single individual laser. For the single individual laser operation, we simply couple each RSOA with a single Si_3N_4 waveguide, where the same broadband reflector is used to provide the optical feedback. The corresponding L-I curves are shown by the black dotted and red dashed line. For the hybridly combined lasers, both RSOAs are turned on simultaneously. The corresponding L-I curve is shown by the blue solid line. Therefore, if the two lasers are coherently combined with a perfect combining efficiency, the output power of the combined lasers should be twice the output power of the single individual laser when the pump currents are the same. As shown in Fig. 4.6(a), we obtain the combining efficiency of ~92% at I = 120 mA (~2×threshold). The measured high combining efficiency further proves that the two RSOA are indeed coherently combined. In addition, it should be mentioned that two RSOAs usually do not have the exact same optical lengths. Thus, in our experiments, we first use the same injection currents for each RSOA to obtain the similar optical gains in each laser cavity. Then, we slightly tune the injection current in one of the two RSOAs in order to obtain the optimal combining efficiency. The current tuning helps to find the common resonant mode and increase the combining efficiency. But the injection current difference between the two RSOAs to achieve the best combining efficiency is always small. Figure 4.6(b) shows the optical spectra for the combined lasers at different thermoelectric cooler (TEC) temperatures. The pump currents are set at 100 mA. As we tune the temperature of the TEC, the lasing wavelengths change from 1554 nm to 1566 nm. The wavelength change is mainly due to

the mode hopping. Since many longitudinal modes exist in the single laser cavity, the mode hopping occurs when the TEC temperature is tuned. The single frequency operation is obtained with a side mode suppression ratio higher than 30 dB at different temperatures. The demonstrated wavelength tuning range is ~12 nm.

Here we use a DSH interferometer to measure the spectral linewidth. The measured RF-beat spectrum is shown as the black circles in Fig. 4.7. The red line shows a Lorentzian fit with a 3 dB bandwidth of 700 kHz, which corresponds to a 350 kHz FWHM laser linewidth. The measured linewidth compares favorably with the approximate 1 MHz linewidth of typical monolithic DBR and DFB laser sources [67]. The linewidth of the hybrid laser is reduced mainly due to the increased cavity length. The linewidth can be further reduced by use of a microring based delay-line filter in the passive chip, which is discussed in Chapter 3.

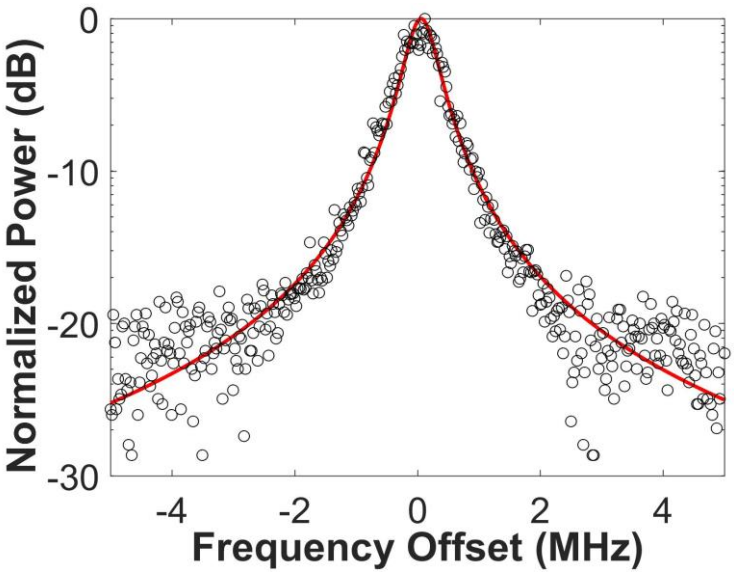

Figure 4.7: Recorded beat spectrum (black circles), the red line shows

a Lorentzian fit corresponding to a laser linewidth of 350 kHz.

4.6 Measurement results for the coupling ratio of the coupler is 60:40

In this section, we investigate the performance of the hybrid laser if the coherent coupler does not have a desired 50:50 coupling ratio. This is important for evaluating the system robustness of the proposed hybrid CBC against fabrication errors. Here, we intentionally set the coupling ratio of the coupler to be around 60:40. Figure 4.8(a) shows the power flow in our system through FDTD analysis. The input light signal at port 1 is unevenly coupled into port 3 and port 4. The output power ratio between the port 3 and the port 4 is 60:40 since no reflection is used in the simulation.

The schematic plot of the hybridly integrated CBC laser system is the same as the one shown in Fig. 4.5(a), except that the coupling ratio of the coupler is set to be 60:40. Figure 4.8(b) shows the measured top-view near field IR image. When only one RSOA (i.e., RSOA B) is turned on, intense scattered light is observed inside the blue line area. The blue line area corresponds to the lossy output port of the coupler, while the green line area still corresponds to the cleaved Si_3N_4 waveguide output facet.

Then, the two RSOAs are turned on at the same time. If the two RSOAs are coherently combined with a 100% efficiency, complete destructive interference must happen at port 4 as shown in Fig. 4.8(c). That means that the input power ratio between port 1 and port 2 should be around 60:40. Thus, the injection currents for the two RSOAs need to be different. In our experiment, the injection current for RSOA B is set to be

around 80 mA, whereas the one for RSOA A is set to be around 70 mA. We select these values based on the measurement results of the single individual hybrid laser. From Fig. 4.6(a), we can find that the ratio of the output power between the single individual laser A (at 70 mA) and the single individual laser B (at 80 mA) is around 40:60. With these settings, we obtain the near field IR image shown in Fig. 4.8(d). It is clear that the intensity of the scattered light from the lossy output port of the coupler is greatly reduced (indicating destructive interference at port 4), while the output power obtained at the cleaved facet remains the same with the situation where only RSOA B is turned on. The results in Fig. 4.8 demonstrate that the two RSOAs are still coherently combined with a high efficiency through the passive CBC cavity with an asymmetric coupler.

For the traditional evanescently-coupled laser array, all the supermodes have the similar modal gains so that there is little modal discrimination among them. It is important to enhance the modal discrimination for the efficient and robust single-mode operation. Here, we improve the modal discrimination and performance of the coherent array by introducing the extra mirror losses into the coupled cavities. Normally loss will result in energy dissipation that is ubiquitous in nature. However, by taking advantage of the different field distributions induced by the extra loss, we demonstrate the coherent beam combing without compromising the laser performance.

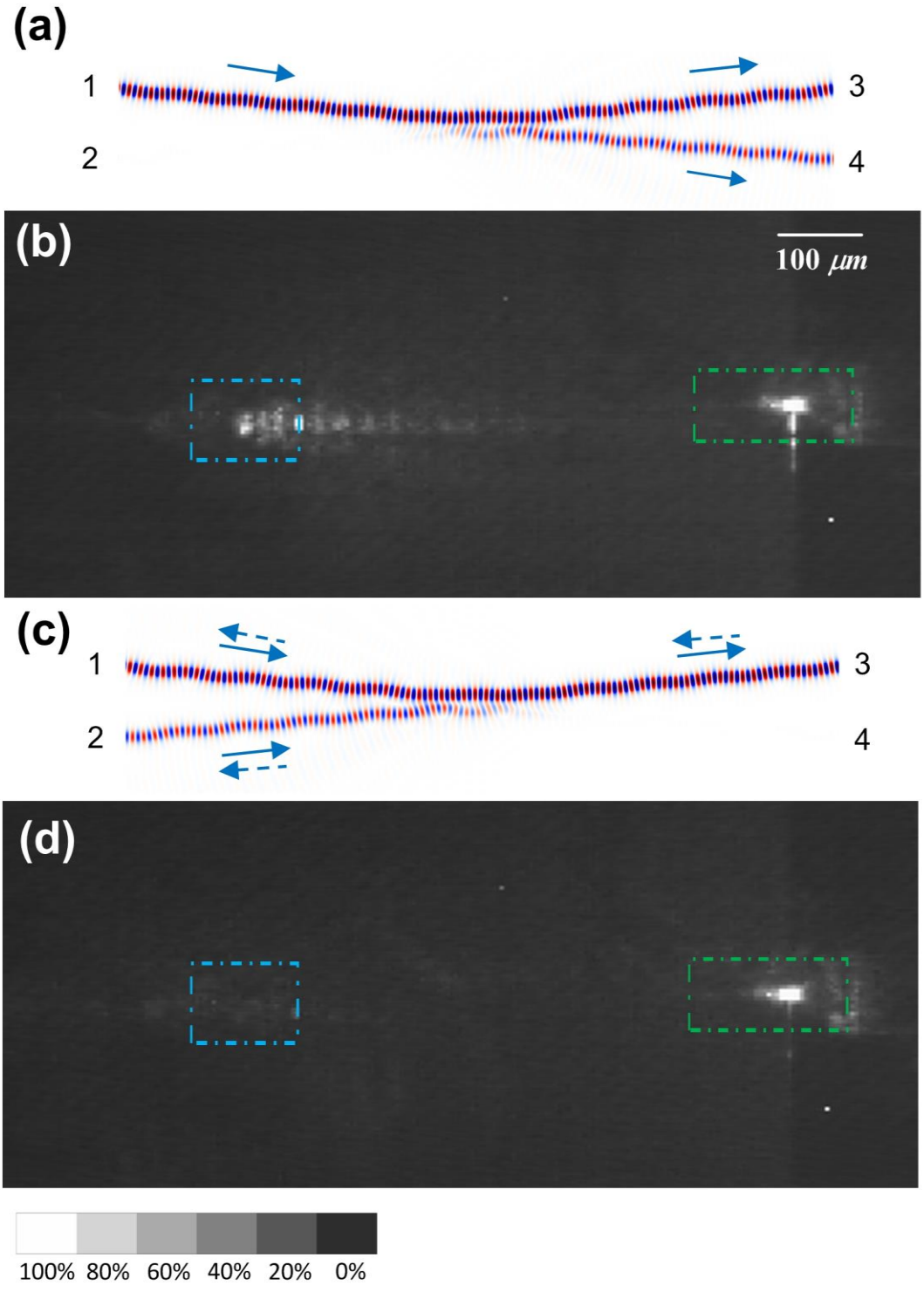

Figure 4.8: (a) FDTD simulation results for the power flow at the coupling region, the coupling ratio is 60:40. (b) near field IR images (top-view) of

the coherently combined lasers if only one RSOA is turned on. (c) FDTD simulation results and (d) near field IR images (top-view) of the coherently combined lasers if both two RSOAs are turned on at the same time. The scale bar shows the relative optical intensity.

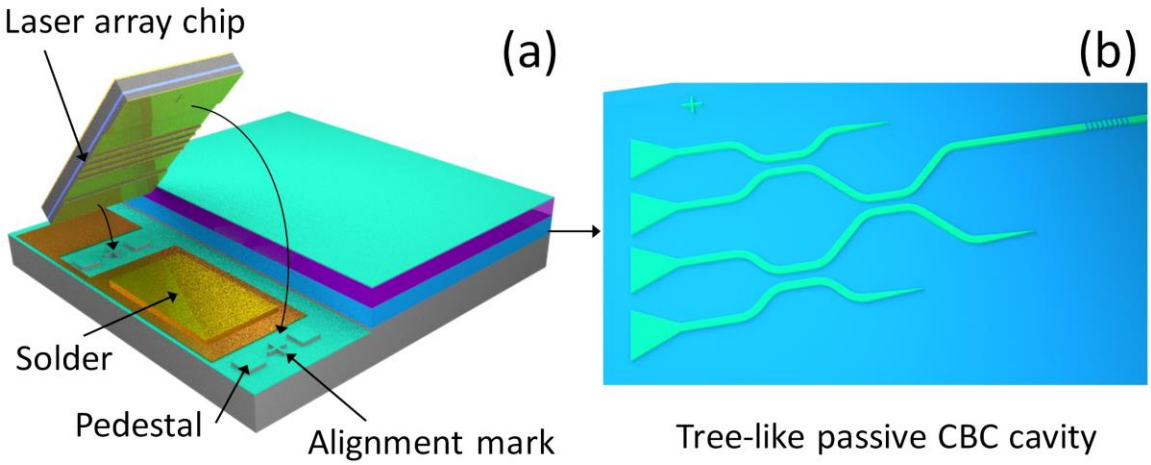

Figure 4.9: Schematic plot of a fully integrated CBC laser system.

Although only two RSOA gain chips are coherently combined through active alignment in this chapter, the demonstrated approach can be expanded to a fully integrated coherently combined laser array system as shown in Fig. 4.9 [68]. Figure 4.9(a) shows the schematic plot of a hybrid integration procedure where a laser gain chip is flip-chip bonded on a silicon chip. Through the hybrid integration, the vertical position of the laser chip is entirely determined by the silicon pedestals and III-V insulation layers. Figure 4.9(b) shows the schematic plot of the passive CBC cavity for four emitters. The proposed hybrid CBC laser system is important for realizing on-chip high

power laser sources for integrated nonlinear optics applications, such as micro-resonator based optical frequency comb generation, on a single silicon chip.

4.7 Conclusion

We experimentally demonstrate the coherent combining of two RSOAs in an InP-Si_3N_4 hybrid platform. The CBC is realized by controlling the mirror loss distribution of the coupled cavities, due to the tendency of the lasing to self-adaptively operate with minimum losses. From the measurement results, we show that the combining efficiency of our system is ~92% at ~2× threshold. Besides, we propose a fully integrated coherently combined laser array system on a single chip. The diode laser based chip-scale CBC system provides the desired system compactness by removing the need of external free-space/fiber components and coupling optics. In addition, it is an ideal platform for investigating the coherence coupling between different lasers.

CHAPTER FIVE

INTEGRATED DIODE LASERS IN EMERGING PLATFORMS

5.1 Introduction

Since different material platforms in photonics provide certain advantages and limitations at the same time, photonic devices have to be fabricated in different material systems based on different photonic functions needed. III-V semiconductors are suitable for light generation and detection. Silicon based platforms are good for obtaining couplers, filters, routers, and modulators et. al. Besides those traditional platforms, in recent years, the emerging platforms (i.e., gain chips based on semiconductor quantum dots, silicon-carbide-on-insulator and lithium-niobate-on-insulator et. al.) have attracted lots of research interests. The integrated diode lasers with high performance in these emerging platforms are highly desired for future PICs.

A unique advantage associated with the integrated diode laser in the hybrid platform is that it can provide a flexible platform to integrate different types of material systems together easily. The active and passive devices are fabricated on their native substrates with different material systems. The desired photonic function is realized using the best suitable material. The coupling between the different material systems is obtained through the mode-matched evanescent wave coupling. In this chapter, we demonstrate that the hybridly integrated diode lasers can also be obtained in these emerging platforms through edge coupling.

5.2 Integrated diode lasers based on quantum-dot gain chips

Besides quantum-well optical gain chips, quantum-dot gain chips can also be integrated into the passive Si_3N_4 platform through hybrid integration. Quantum-dot gain media provide various attractive advantages, such as a small linewidth enhancement factor, ultra-broad optical gain bandwidth, wide wavelength availability, and low temperature dependence [40]. In addition, quantum-dot gain media are good candidates for obtaining uncooled diode lasers, due to strong quantization effects with quasi-zero dimension, which can greatly reduce the total cost and power consumption. Therefore, it is promising to realize the widely tunable narrow linewidth diode lasers in the quantum-dot RSOA/Si_3N_4 platform.

Figure 5.1 shows the schematic plot of the hybridly integrated diode laser. It is composed of a quantum-dot RSOA gain chip and $Si_3N_4/SiO_2/Si$ chip. The BOX layer is 4 μm thick. The RSOA has a HR coated back-facet with 90% reflectivity and an AR coated front facet. In order to efficiently couple the light between the active and passive chip, a well-designed spot size converter is used to reduce the large mode mismatch between the waveguides in the Quantum-dot RSOA and Si_3N_4 chips. The experimentally measured coupling loss of less than 2 dB is obtained. Besides, the RSOA and Si_3N_4 waveguide are both angle-cleaved for eliminating the reflection at the interface between the RSOA and passive chip. The Si_3N_4-based external cavity consists of double-ring micro-resonators with slightly different radii acting as a wavelength filter and extended cavity. The radii

for the two microrings are 51 and 54 μm, respectively. A Sagnac loop mirror at the Si_3N_4 waveguide output port is utilized here to reflect the light back into the laser cavity. The reflectivity is around 50%. The width of the single mode silicon nitride waveguide is set to be 900 nm and the height is 300 nm. The hybrid composite laser cavity is composed of the RSOA, two microring resonators, loop mirror, and input/output waveguides. Micro-heaters are utilized to thermally tune the resonance wavelength of microring resonators for obtaining the wavelength tunability.

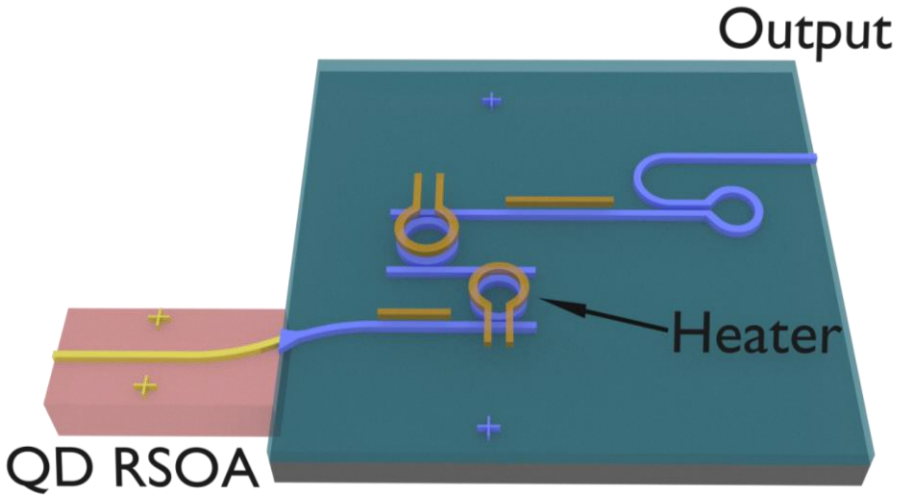

Figure 5.1. Schematic plot of the hybridly integrated diode laser.

An active alignment method is used here to demonstrate the hybrid integration of the RSOA and passive chip for simplicity. The laser light output is collected and measured from the output port. Figure 5.2 shows the experimental results of the hybridly integrated laser based on the quantum-dot RSOA gain chip. The L-I curve for the laser with the threshold current of 95 mA is shown in Fig. 5.2(a). The slope efficiency is 50

mW/A. Figure 5.2(b) shows the output optical spectrum (the pump current is set at 180 mA). The single frequency lasing with ~50 dB SMSR is obtained due to the Vernier effect between the two microrings with different FSRs. A DSH interferometer with a 10-km delay line is used here to measure the laser spectral linewidth. The red dots in Fig. 5.2(c) shows the measured RF-beat spectrum. The black line corresponds to a Lorentzian fit. The FWHM laser linewidth obtained is 85 kHz. The linewidth of the hybrid laser is reduced mainly due to the increased effective cavity length and small linewidth enhancement factor of the quantum-dot gain material. The superimposed spectra are shown in Fig. 5.2(d) when one of the two microresonators is thermally tuned. The wavelength tuning range of ~47 nm is obtained.

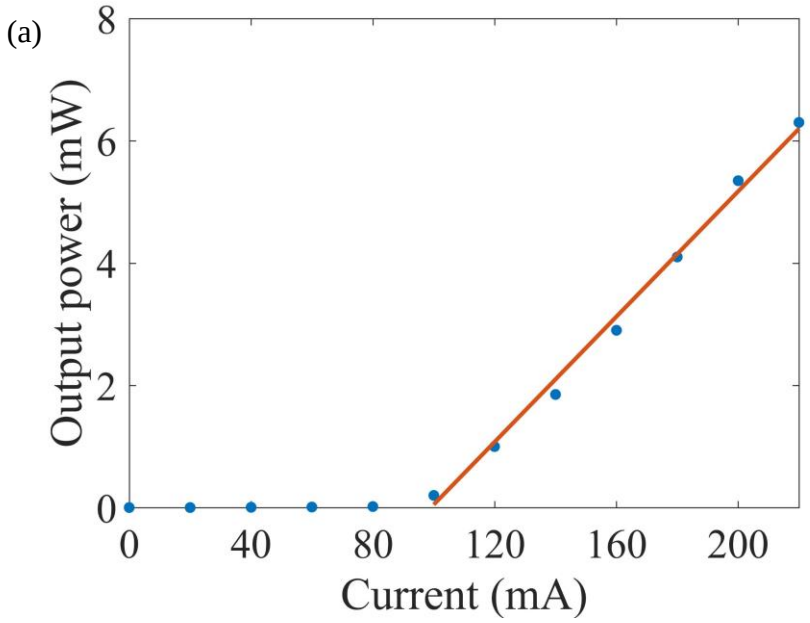

(b)

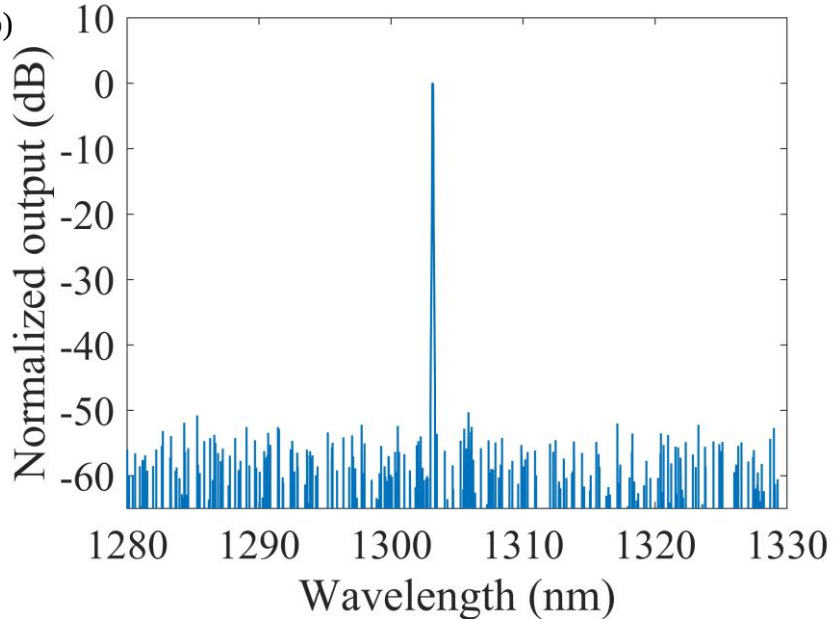
10
0
-10
-20
-30
-40
-50
-60
Normalized output (dB)
1280
1290
1300
1310
1320
1330
Wavelength (nm)

(c)

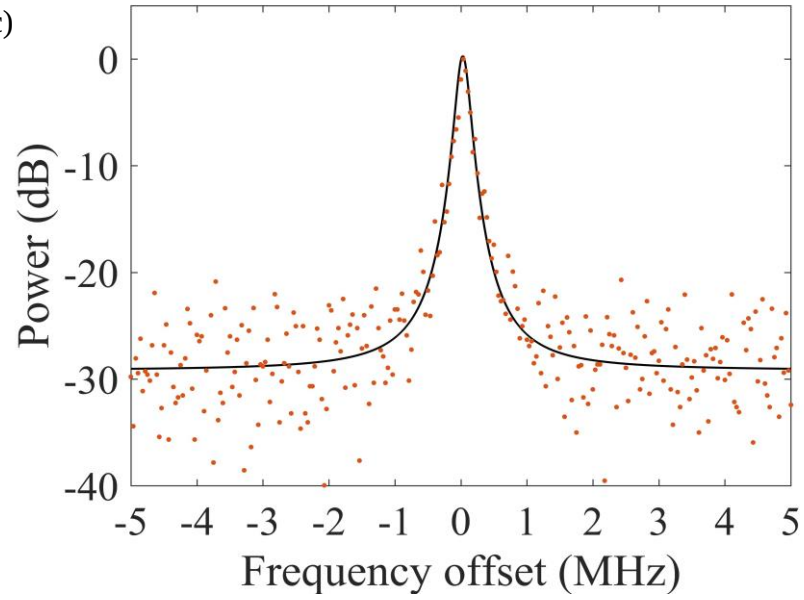
0
-10
-20
-30
-40
Power (dB)
-5
-4
-3
-2
-1
0
1
2
3
4
5
Frequency offset (MHz)

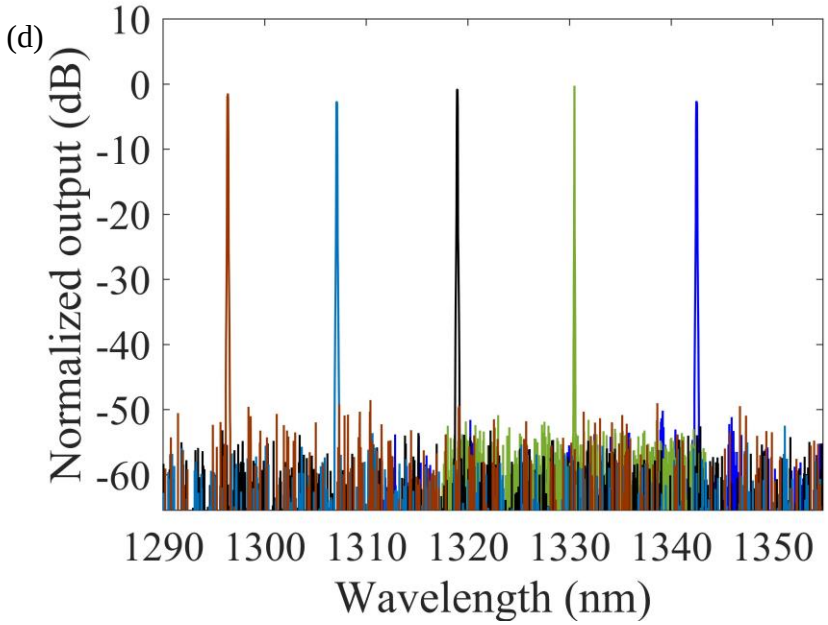

Figure 5.2. Experimental results of the hybrid laser. (a) The L-I curve. (b) The measured optical spectrum with the single frequency operation. (c) Recorded RF beat spectrum (red dots). The black line shows a Lorentzian fit corresponding to a laser linewidth of 85 kHz. (d) Superimposed spectra when thermally tuning one of the two microresonators (the tuning range is ~47 nm).

5.3 Integrated diode lasers in silicon-carbide-on-insulator platform

The emerging platform, i.e., silicon-carbide-on-insulator (SiCOI) platform, has attracted lots of research interests due to its strong optical nonlinearity, piezoelectric, excellent thermal conductivity, large bandgap, silicon compatibility and unique quantum

properties [69]. Here we demonstrate an integrated diode laser in the silicon-carbide-on-insulator platform through edge coupling.

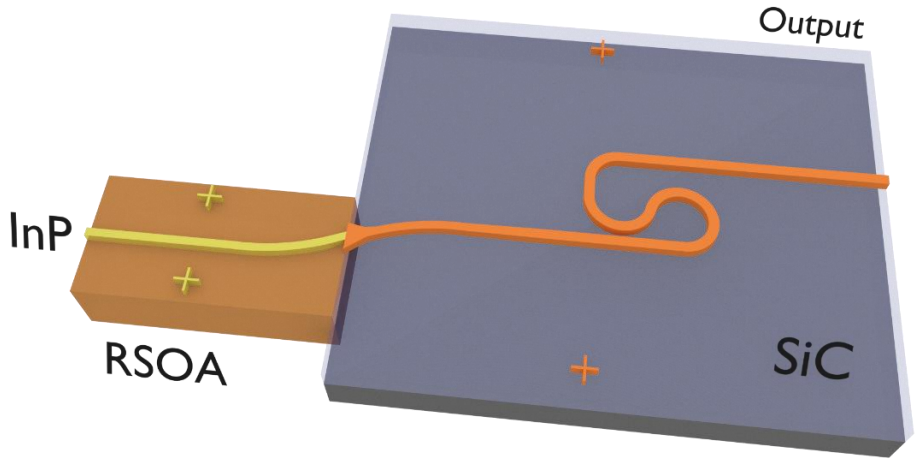

Figure 5.3. Schematic plot of the hybridly integrated diode laser.

Figure 5.3 shows the schematic plot of the hybridly integrated diode laser. It consists of an InP RSOA gain chip and a SiC/SiO_2/Si chip. The BOX layer is thick enough (4 μm) to prevent optical leakage from the SiC waveguide layer to the Si substrate. The RSOA has a HR coated back-facet with a 90% reflectivity and an AR coated front facet. Due to the large mode mismatch between the waveguides in the RSOA and SiC chips, we use a well-designed spot size converter to efficiently couple the light between active and passive chips. The waveguide width at the input end of the converter is 5.9 μm, so the diode laser mode can be matched well with the input end of the converter. Then the waveguide is narrowed down to the width of the single mode waveguide. Besides, the RSOA and SiC waveguide are both angle-cleaved to eliminate

the reflection at the interface between the RSOA and passive chip. The loop mirror in the SiC platform provides the optical feedback for lasing. The measured reflectivity of the cleaved facet is around 50%. The light is coupled into a lensed fiber for measuring the output of the laser at the cleaved facet through a well-designed spot size converter. The width of the single mode silicon carbide waveguide for the lasing wavelength of 1.55 μm is set to be 600 nm and the height is 500 nm. The hybrid composite laser cavity consists of the RSOA, loop mirror reflector, and input/output waveguides.

Figure 5.4 shows the experimental results of the hybridly integrated laser based on the InP RSOA gain chip. The L-I curve for the laser is shown in Fig. 5.4(a). The threshold current is around 85 mA. The slope efficiency is 6 mW/A. The low slope efficiency results from the high coupling loss at the interface between the two chips, which can be improved by using an optimized facet surface in the future. The normalized output optical spectrum is shown in Fig. 5.4(b) (the pump current is set at around 140 mA). The single frequency lasing with ~28 dB SMSR is obtained.

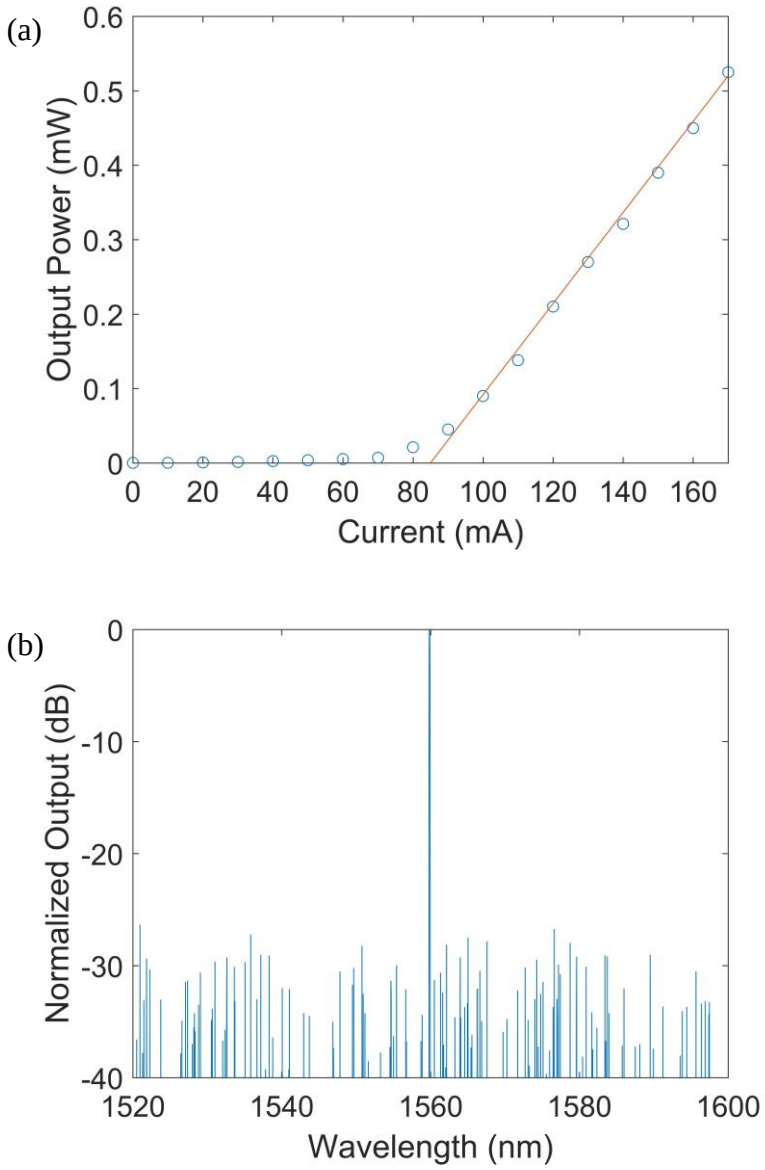

Figure 5.4. LI curve (a) and optical spectrum (b) of the hybrid laser.

5.4 Integrated diode lasers in lithium-niobate-on-insulator platform

Lithium-niobate exhibits one of the largest electro-optic effects among all optical media, of nearly unlimited operation bandwidth with a response time down to femtosecond [70]. This excellent property together with innovative device/circuit design offers a promising solution to realize high power, tunable lasers and integrated high-speed, energy-efficient, and lossless spatiotemporal modulators. Here, we demonstrate that the integrated diode laser can also be obtained in the lithium-niobate-on-insulator platform through the edge coupling approach. The schematic plot is the same with that shown in Fig. 5.3.

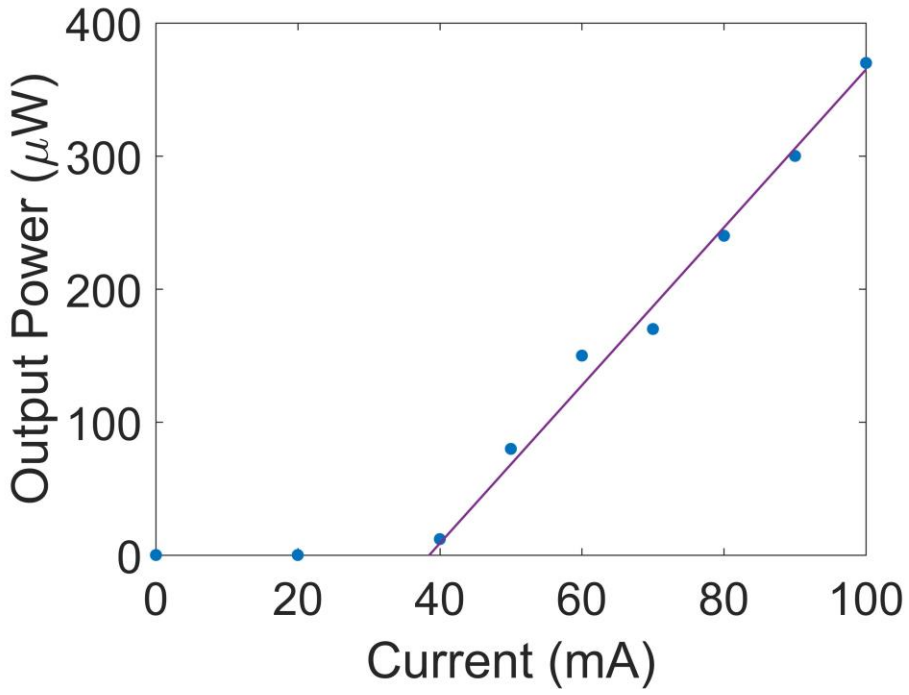

Figure 5.5. L-I curve of the hybridly integrated diode laser.

Figure 5.5 shows the experimental results of the hybridly integrated laser based on the InP RSOA gain chip in the lithium-niobate-on-insulator platform. The L-I curve for the laser is shown. The threshold current is around 38 mA. The detailed results will be given in our future work.

5.5 Conclusion

In summary, the hybrid integration of a low-loss, passive Si_3N_4 external cavity with a quantum-dot RSOA at 1.3 μm in silicon nitride photonics platform. The laser linewidth obtained is around 85 kHz. The tuning range is around 47 nm. Our design has the potential to provide on-chip narrow linewidth laser sources with wide wavelength tunability for passive photonic integrated circuits. In addition, we demonstrate the hybridly integrated diode lasers in the silicon-carbide-on-insulator and lithium-niobate-on-insulator platforms through edge coupling.

CHAPTER SIX

ACCESSING THE EXCEPTIONAL POINTS THROUGH HYBRID INTEGRATION

6.1 Introduction

Parity-Time (PT) symmetric non-Hermitian systems have aroused considerable interests since the late 1990s [59, 71, 72]. A unique feature associated with PT symmetric non-Hermitian systems is that the breaking of the PT symmetry occurs once the non-Hermiticity parameter exceeds a certain threshold. The PT symmetry breaking results in the appearance of the phase transition point (also known as the expectational point) and leads to the splitting of the imaginary part of the eigenfrequencies of the supermodes [73-75]. It has been recognized that the coupled optical cavities, in which the gain and loss are judiciously modulated, can be treated as an analogy to the non-Hermitian quantum system [76]. When the coupled optical cavities are departed from a conventional Hermitian system to a non-Hermitian system, the efficient access of exceptional points (EPs) is obtained through controlling the intercavity coupling and gain/loss contrast. In optical systems, PT symmetry requires the complex refractive index of the system to satisfy $n(x) = n^*(-x)$. It means that the gain/loss distribution in the system has to exhibit the odd symmetry about $x = 0$. In most of PT symmetric optical setups demonstrated for now, the exact PT symmetry is not implemented with perfectly balanced gain and loss. Instead, the non-Hermitian features are observed under the condition that a sufficient loss

or gain contrast exceeds the coupling constant [59]. Many interesting phenomena and results have been demonstrated, such as beam steering, unidirectional light propagation, enhanced sensitivity, lasing mode control and selection, and coherent perfect absorption, to mention a few [77, 78]. Optical beam dynamics due to modal non-orthogonality has been investigated [79]. Unidirectional light transmission or reflection is an attractive feature in non-Hermitian optical systems and has been demonstrated in coupled optical resonators [80-82] and periodic PT symmetric structures [32, 83-87]. Enhanced sensitivity of active sensors working around the EPs has also been demonstrated [88, 89]. Lasing mode control and selection in PT symmetric optical structures have attracted intense interests. The onset of lasing in the PT symmetric coupled resonators is observed with the increased total loss of the system [90]. Single mode lasing is obtained in PT symmetric coupled cavities, and the phase transition of lasing modes at the EPs is directly measured in coupled photonics crystal cavities [91]. With the asymmetric pumping, reversed pump dependence of lasing and PT symmetry breaking are observed [92, 93]. In the single microring setup, single mode lasing can also be obtained when a periodic PT symmetric gain/loss perturbation is introduced [94, 95]. Coherent perfect absorber (CPA) has been realized in PT symmetric optical structures [96-98].

Coupled-resonator based non-Hermitian optical systems have been demonstrated by use of three different configurations: passive-passive, passive-active, and active-active. Here, the active resonator is defined as the one that can be optically or electrically pumped to provide optical gain, while the passive resonator is defined vice versa. In the passive-passive configuration, the PT symmetry breaking is achieved by externally

introducing a loss channel for one resonator and thus increasing the loss contrast between the two coupled resonators. For the passive-active and active-active configurations, the PT symmetry breaking is achieved by selectively pumping one active resonator or asymmetrically pumping both active resonators. The active-active setup allows for the versatile control of the gain/loss of the individual resonator and enables the efficient access of the EPs through introducing the sufficient gain/loss contrast. Among most of active-active PT symmetric systems, optical pumping is used to obtain the required gain/loss contrast. However, electrical pumping is highly desired and necessary for practical applications in integrated photonics [3, 5]. So far, electrically pumped PT symmetric coupled resonators have only been demonstrated in a monolithic platform. Thus, either epitaxy regrowth or complex fabrication is needed to obtain the independent control of each active resonator.

In this chapter, we demonstrate that hybrid photonic integration provides a flexible platform to design and create the non-Hermitian optical system [40, 99]. In our hybrid platform, we separate the passive coupling and feedback regions from the active gain components so that the gain, loss and intercavity coupling are independently controlled. Such an electrically pumped, hybridly integrated non-Hermitian system is a promising candidate to access the EPs through the interplay between the gain/loss contrast and coupling and enable a wide range of practical applications. In addition, for most PT symmetric coupled resonators experimentally demonstrated for now, whispering gallery mode resonators such as microring, microdisk, and microtoroid resonators are used. For these microresonators, the loss manipulation usually relies on externally

introducing a loss channel such as a metallic tip into the optical system. Instead, we use the PT symmetric coupled F-P resonators to demonstrate the non-Hermitian features in the hybrid platform [100]. Since the total loss of a F-P resonator is the sum of the intrinsic loss and mirror loss, we can conveniently manipulate the total cavity loss by changing the waveguide geometric parameters to increase the mirror loss. In this way, we are able to obtain the PT symmetry breaking through both asymmetric pumping and loss manipulation in the same hybrid platform. The experimentally demonstrated non-Hermitian optical system in this work has several unique advantages. First, our hybrid system is electrically pumped, which enables a wide range of practical applications. Second, though two F-P resonators are coupled in this paper, our approach can be feasibly expanded to multiple F-P resonators. Since the gain, loss and intercavity coupling are flexibly controlled in this hybrid platform, it provides a convenient method to access the high order exceptional points with multiple coupled F-P resonators. Finally, compared with the previously reported PT symmetric lasers, the output power of our hybrid laser is increased to be a few mWs, due to the millimeter-long laser cavity used.

6.2 Device design and fabrication

Figure 6.1 presents the schematic plot of the coupled laser system based on the hybrid integration approach. It consists of two InP-Si_3N_4 hybrid F-P cavities. Each F-P cavity includes an InP-based RSOA and a Si_3N_4 waveguide. The electrically pumped RSOA provides the gain for the F-P cavity. The length of the RSOA is ~1 mm. It has a

HR coated back facet with ~90% reflectivity. The RSOA front facet is AR coated. The length of the Si_3N_4 passive waveguide is ~3 mm. The optical feedbacks of the hybrid F-P cavity are provided by the HR coated back facet of the RSOA and the cleaved facet at the Si_3N_4 waveguide output port. The F-P cavity total loss can be controlled by changing the reflectivity at the Si_3N_4 waveguide output port since it directly modifies the cavity mirror loss. The interface reflection between the RSOA and the Si_3N_4 waveguide is minimized (see Methods). The optical coupling between the two F-P cavities is obtained through a coupling region where the two symmetric Si_3N_4 waveguides are placed closely together in the passive chip. In the coupled F-P laser cavities, the gain, loss and coupling can be controlled separately in the three different regions as shown in Fig. 6.1.

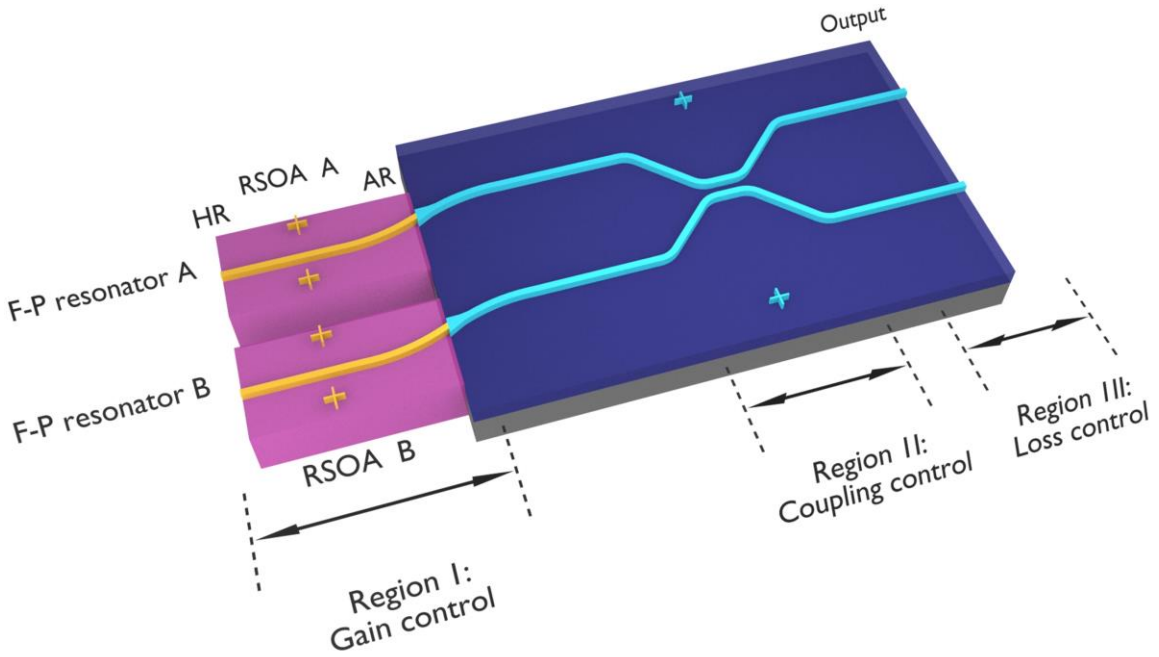

Figure 6.1. The schematic plot of the coupled F-P laser cavities in the InP-Si_3N_4 hybrid platform. Each F-P cavity includes an InP-based RSOA and a Si_3N_4

waveguide. The independent control of the gain, loss, and coupling is obtained in the three different regions.

The eigenfrequencies of the supermodes in the coupled F-P cavities for a specific order longitudinal mode can be obtained by solving the eigenvalue problem of the coupled mode equations in the time domain (See Methods). κ is the coupling coefficient. γ_1, γ_2 are the gain/loss coefficients for the two cavities respectively. $\Delta\gamma = (\gamma_1 - \gamma_2)/2$ is the gain/loss contrast. Figure 6.2 shows the variation of the real and imaginary parts of the eigenfrequencies for the two supermodes in the coupled F-P resonators as a function of the gain or loss contrast. We can find that any pair of modes whose gain or loss contrast is smaller than the coupling coefficient ($\Delta\gamma < \kappa$) will remain neutral. When both resonators are subject to the same level of gain/loss ($\Delta\gamma = 0$), the real parts of the eigenfrequencies are split by 2κ, while their imaginary components remain degenerate. The insets in Fig. 6.2(b) show the mode profiles through the FEM. The two supermodes both have the symmetric intensity distribution in the two coupled cavities, so the light evenly emits from the two cavities. As the gain or loss contrast between the two F-P resonators increases, the real parts of the eigenfrequencies coalesce gradually. The point at which the real and imaginary parts of the two eigenfrequencies are both degenerate is known as the exceptional point and marks the threshold for the PT symmetry breaking. As soon as the contrast of gain or loss exceeds the coupling coefficient ($\Delta\gamma > \kappa$), the PT symmetry condition will be broken, and a conjugate pair of lasing/absorption modes will emerge. The real parts of the eigenfrequencies of the two supermodes remain the same,

while the imaginary parts of the eigenfrequencies split. The insets in Fig. 6.2(b) also show the mode profiles of the lasing mode and absorption mode.

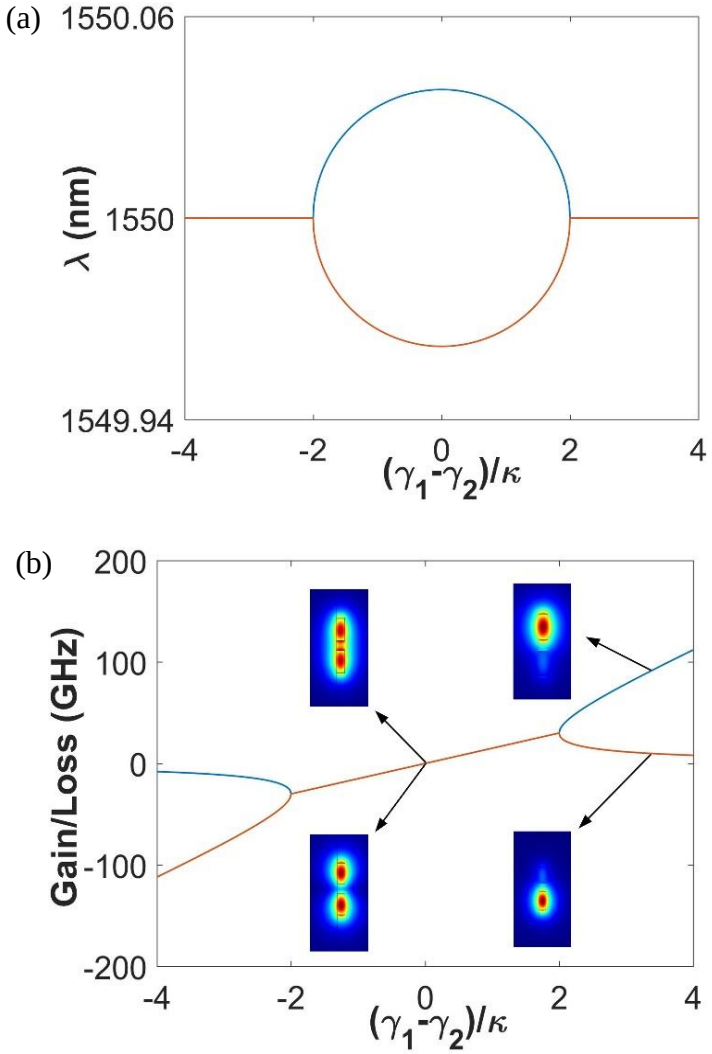

Figure 6.2. Bifurcations of complex eigenfrequencies around the EPs. The splitting of the real parts (a) and imaginary parts (b) of the eigenfrequencies for the two supermodes in the coupled F-P resonators as a function of the gain or loss contrast. The insets show the mode profiles of the two

supermodes in the coupled cavities under the condition of the PT symmetry (left) or broken PT symmetry (right) through the FEM simulation.

Since the gain, loss and coupling are controlled separately in our coupled F-P laser system, the PT symmetry breaking can be obtained through either the asymmetric gain distribution in the active chips or asymmetric loss distribution in the passive chip. We first realize the asymmetric gain distribution by applying different pumping currents for the two RSOAs. By increasing the gain differences between the two RSOAs, we demonstrate the PT symmetry breaking and appearance of the EPs. Then, we obtain the asymmetric loss distribution by increasing the mirror loss for one Si_3N_4 waveguide output port in the passive chip. In this way, we also achieve the breaking of the PT symmetry and obtain the coherent addition of the two RSOAs.

6.3 Accessing the EPs through the asymmetric gain distribution

We first measure the optical spectrum of the single hybrid F-P laser. For the single hybrid laser shown in Fig. 6.3(a), we couple the RSOA with a single Si_3N_4 waveguide with cleaved facets. The corresponding optical spectrum with multiple longitudinal modes is shown in Fig. 6.3(b). The FSR of the single hybrid laser is about 0.11 nm, which matches well with the total hybrid cavity length. We then measure the optical spectrum of the coupled hybrid F-P lasers. Figures 6.3(c) and (e) show the experimental setups of the coupled F-P laser cavities. In order to obtain the efficient current and thermal control of the two RSOAs, they are placed at the two

different sides of the Si_3N_4 passive chip. This configuration allows us to put each RSOA on an independent TEC for the accurate temperature control. It is important to control the temperature of the two RSOAs separately so that the refractive index change due to different optical gains (injection currents) could be compensated. The coupled lasers include two individual F-P cavities, i.e., the upper cavity A and lower cavity B. For the cavities that are separated about 900 *nm* in the coupling region, the coupling strength is about 20 GHz, as shown in the inset of Fig. 6.3(c). This level of coupling requires a gain contrast of ~ 30 /cm between the two RSOAs to reach the PT symmetry breaking threshold. In our hybrid system, this amount of gain difference can be readily obtained by changing the RSOA injection currents. Figures 6.3(d) and (f) illustrate the output spectra of the coupled F-P lasers before and after the PT symmetry is broken, respectively. In Fig. 6.3(d), the two RSOAs are turned on at the same time with the same injection currents (~ 80 mA). We can find that each longitudinal mode is split into two spectral peaks with a separation of 0.047 nm, which proves that the real parts of the two supermodes' eigenfrequencies are separated by 2κ with the symmetric pumping ($\Delta\gamma = 0$). Since the imaginary parts of both supermodes are equal, they are evenly distributed in the two cavities. The insets in Fig. 6.3(c) show the IR images captured at the HR coated back-facet port of each RSOA. We can find that the light intensity is evenly distributed between the two ports. As shown in Fig. 6.3(f), after the sufficient gain contrast is introduced by reducing the injection current of RSOA A, the spectral splitting of the longitudinal modes disappears. This means that the real parts of the resonant frequencies become degenerate, while the imaginary parts bifurcate. One of the supermodes primarily remains in the cavity with higher gain while the other one mainly occupies the other cavity with lower gain. This leads to the uneven light intensity distribution in the two

coupled cavities, as shown in the insets of Fig. 6.3(e). It should be pointed out that we did not obtain the single mode lasing when the PT symmetry was broken with the asymmetric gains. It is challenging to obtain the single longitudinal mode operation based on the PT symmetry breaking in millimeter long edge emitting lasers with smaller FSR. Nonetheless, the PT symmetry breaking and access of the EPs can still be obtained.

Next, we show the lasing spectrum transition process for a specific order longitudinal mode when the gain (injection current) differences between the two coupled cavities are increased. We start with an evenly distributed gain profile and gradually reduce the gain in one of the RSOAs by decreasing its injection current. In our experiments, we also tune the operation temperature of this RSOA so that the central wavelength of the spectrum remains the same. In this way, we compensate the refractive index change induced by the current change. Figure 6.4 shows the corresponding evolution of the output spectra. As the gain contrast is increased, the two resonant peaks associated with the two supermodes move toward each other, and finally coalesce together.

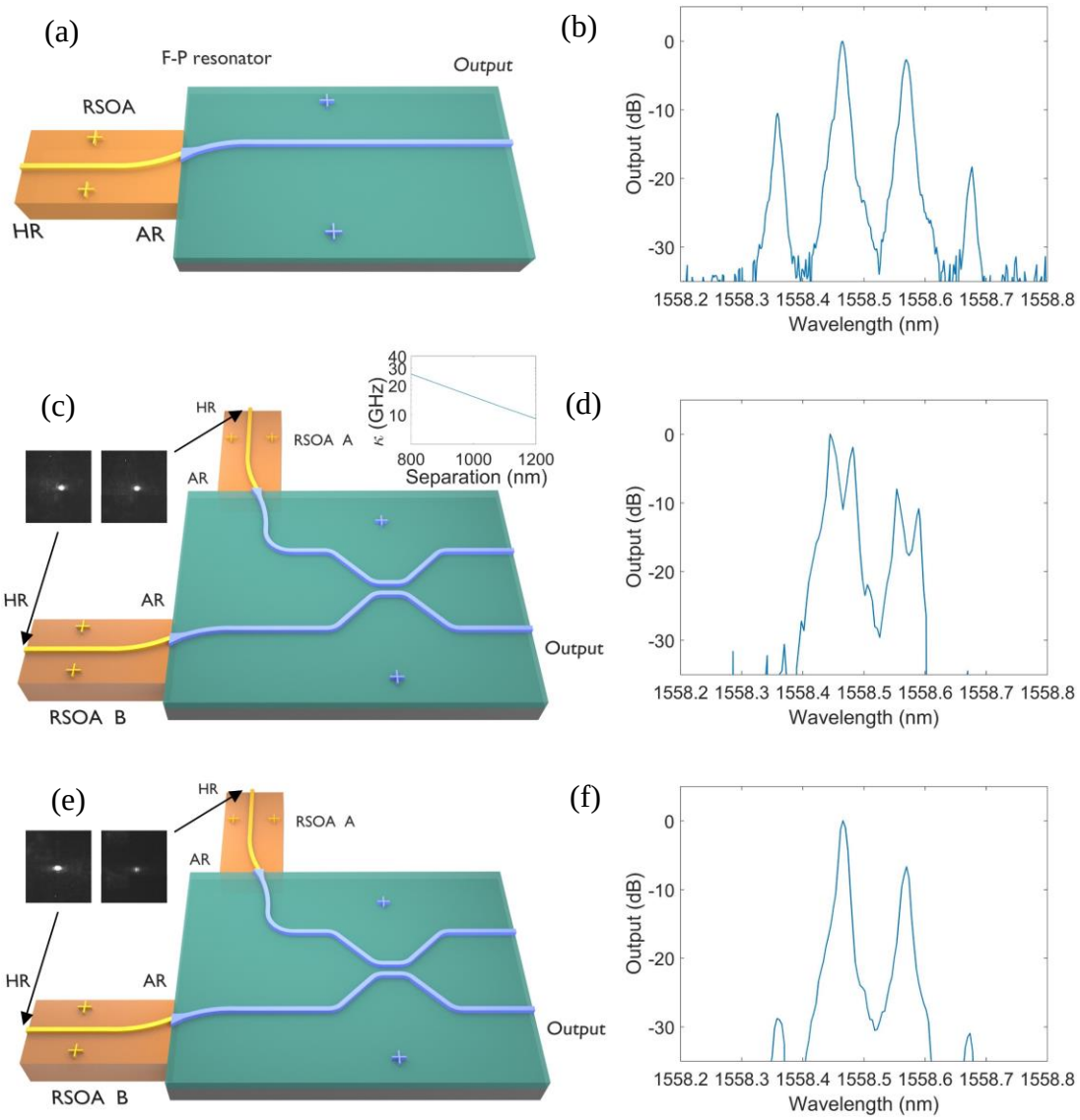

Figure 6.3. Breaking the PT symmetry through the asymmetric gain distribution. (a) The schematic plot of the hybridly integrated laser cavity for the single individual laser operation. (b) The optical spectrum of the single hybrid laser. The schematic plot of the coupled lasers in the hybrid platform with the symmetric pumping (c) and the asymmetric pumping (e). The inset in (c) shows that the coupling coefficient depends exponentially on the separation

distance between the two waveguides (logarithmic scale). The inserted IR images in (c) and (e) are captured at the HR coated back-facet port of the two RSOAs, respectively. Optical spectra of the coupled lasers with the symmetric pumping (d) and the asymmetric pumping (f), respectively.

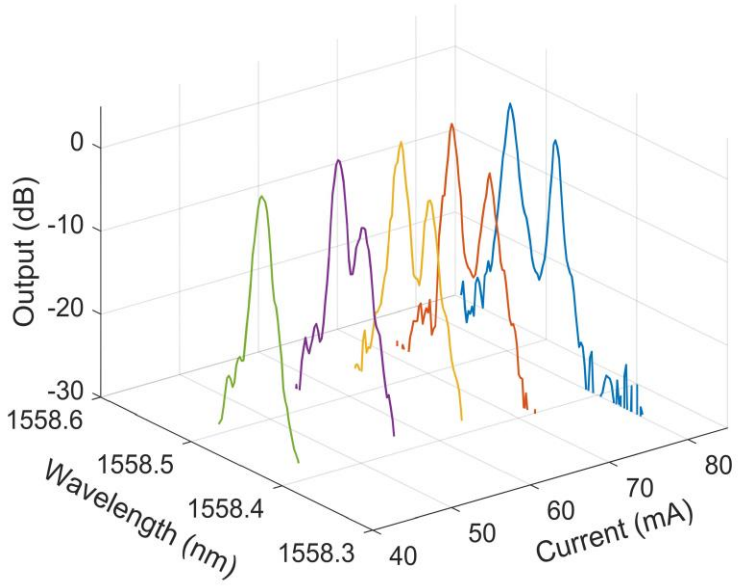

Figure 6.4. Accessing the EPs through the asymmetric gain distribution. Evolution of the optical spectrum of the coupled F-P lasers as the injection current of one RSOA decreases from 80 mA to around 45 mA and the injection current of the other RSOA remains unchanged.

When the coupled system passes the EPs, the two supermodes become spectrally degenerate but they have the different spatial distributions and modal gains. In the PT symmetry broken phase, although the strongly asymmetric intensity distribution at the HR coated back-

facets of the two RSOA is obtained, there is still the light emitting from both Si_3N_4 output ports in the passive chip. This is because the gain is not uniformly distributed within the whole cavity for the hybrid system, different from PT symmetric optical resonators formed in the monolithic platform. In addition, the loss distribution of the upper and lower cavities in the passive chip is still symmetric. Light can be coupled into the lower cavity from the upper cavity in the coupling region located on the passive chip. To eliminate the light emitting from the output port of the lower cavity, the asymmetric loss distribution must be introduced in the passive chip.

6.4 Breaking the PT symmetry through the asymmetric mirror losses

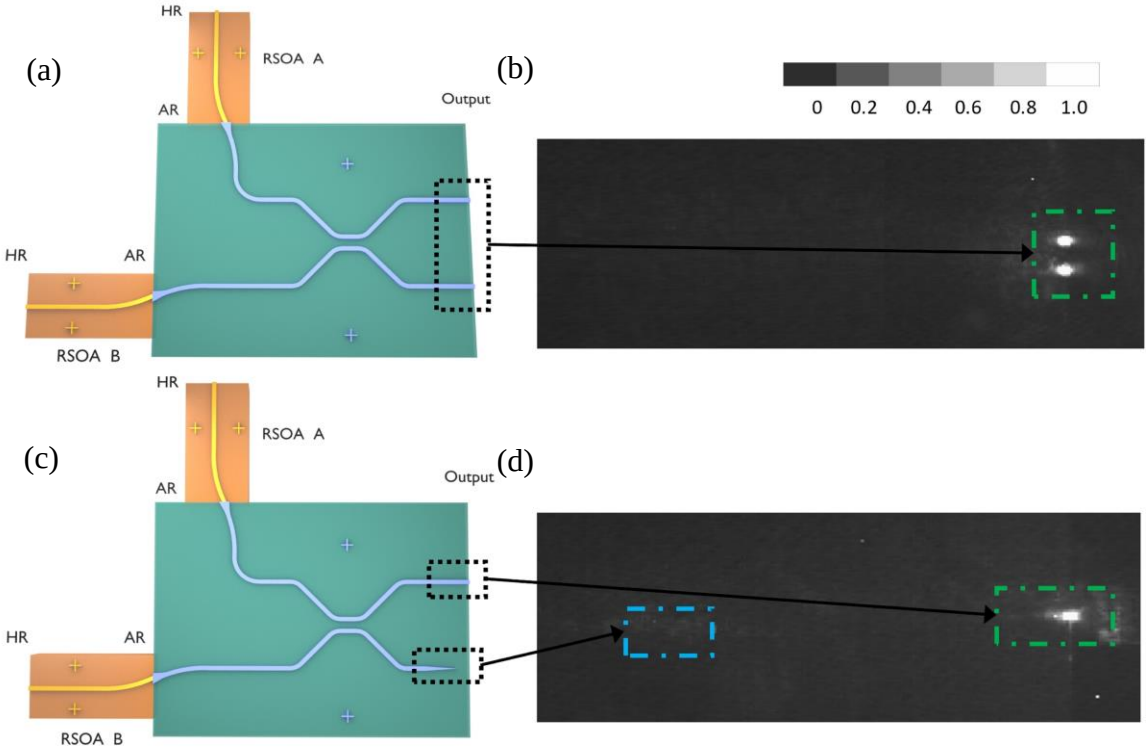

Figure 6.5. Breaking the PT symmetry through the asymmetric losses.

The schematic plots and IR images of the coupled F-P lasers in the hybrid platform with symmetric mirror losses (a) and (b). with asymmetric mirror losses (c) and (d), respectively. The green line area corresponds to the Si_3N_4 waveguide with the cleaved facet, while the blue line area corresponds to the lossy output port. The grayscale bar shows the normalized optical intensity.

Here, we demonstrate the PT symmetry breaking through introducing the asymmetric losses in the passive chip. It is well known that a sufficient loss contrast, instead of a gain contrast, can also be used to induce the PT symmetry breaking. The loss control in most of the non-Hermitian optical systems is obtained through adjusting the intrinsic loss with an external scatter or absorber. For a F-P laser cavity, the total loss γ includes the intrinsic loss γ_i and the mirror loss γ_m ($\gamma = \gamma_i + \gamma_m$). Thus, the total loss of each F-P resonator can be controlled by tuning the cavity mirror losses, i.e. the reflectivity at the Si_3N_4 waveguide output ports. In this way, we can obtain the sufficient loss contrast to break the PT symmetry. Figure 6.5(a) shows the hybrid system with two coupled F-P cavities that have the same mirror losses, same as the system discussed above. Figure 6.5(c) shows the hybrid system with the asymmetric mirror losses. One of the output waveguides is gradually narrowed down and provides almost no reflection, which results in the sufficient loss contrast for the hybrid system to break the PT symmetry. The relation between the mirror loss γ_m and the reflection coefficient r is given in Eq. (6.1). L is the total cavity length, n_g is the group index, and c is the speed of light in vacuum. When we change the reflection coefficient of the output port in a F-P cavity, we change the mirror loss and thus the total cavity loss. If the

intrinsic loss γ_i is ignored here, $\gamma_{avg} = (\gamma_1 + \gamma_2)/2 = (\gamma_{m1} + \gamma_{m2})/2$ and $\Delta\gamma = (\gamma_1 - \gamma_2)/2 = \Delta\gamma_m = (\gamma_{m1} - \gamma_{m2})/2$,

$$\gamma_m = \frac{1}{2L} c n_g \ln \frac{1}{r} \tag{6.1}$$

$$\omega_{\pm} = \omega_0 - i\gamma_{avg} \pm \sqrt{\kappa^2 - \left(\Delta\gamma_m\right)^2} \tag{6.2}$$

From Eq. (6.2), for the asymmetric cavity design shown in Fig. 6.5(c), the splitting of the imaginary parts of the eigenfrequencies occurs when the sufficient mirror loss contrast is introduced. After the PT symmetry is broken, a conjugate pair of lasing and absorption modes is obtained. The lasing mode will occupy the cavity with the lower mirror loss (higher reflection), while the absorption mode will stay at the cavity with the high mirror loss (lower reflection). If only the lasing mode is selected, the light will only emit from the output port with higher reflection, leading to the coherent addition at this port.

Figure 6.5(b) shows the top-view IR image of the coupled cavities with the symmetric mirror losses at the two output ports. The two RSOAs are turned on at the same time with the same injection currents. We can find that the light emits from the two output ports evenly. For the coupled cavities with the asymmetric mirror losses shown in Fig. 6.5(c), the two RSOAs are also turned on at the same time with the same injection currents. However, the PT symmetry is broken by the intentionally introduced loss contrast. In Fig. 6.5(d), the green line area corresponds to the Si_3N_4 waveguide with the

cleaved facet, while the blue line area corresponds to the lossy output port. From the top-view IR image shown in Fig. 6.5(d), we can find that the light only emits from the upper port and there is almost no scattered light around the lossy port, indicating the selection of the lasing mode and absence of the absorption mode. These results prove that the PT symmetry breaking successfully leads to the lasing mode selection in the hybrid system.

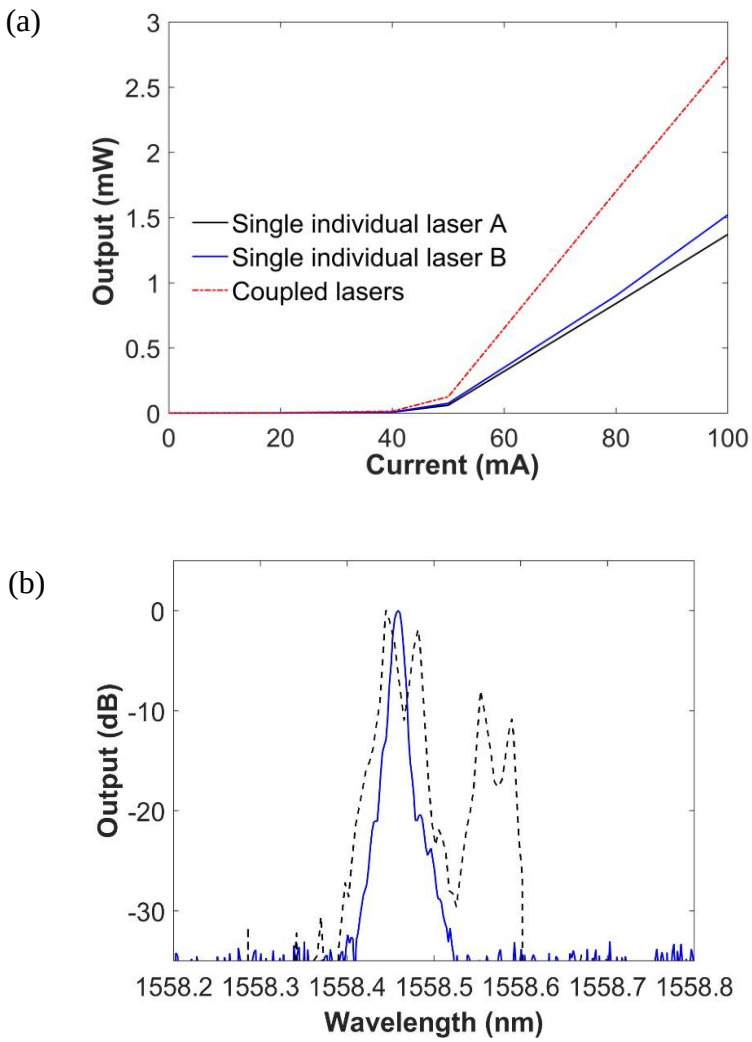

Figure 6.6. Lasing characteristics. (a) L-I curves of the coupled lasers

with the asymmetric mirror losses (red line) and single individual lasers (blue and black lines), respectively. (b) optical spectrum of the coupled lasers with the asymmetric mirror losses (solid blue line) and with the symmetric mirror losses (dashed black line), respectively.

Figure 6.6(a) shows the L-I curves of the coupled lasers and single hybrid lasers. For the single hybrid laser, the corresponding L-I curves are shown by the blue or the black line. For the coupled lasers, the corresponding L-I curve is shown by the red line. When the PT symmetry is broken, the lasing mode selection leads to the coherent addition of the two coupled lasers at the shared common output port. Therefore, with the 100% addition efficiency, the output power of the coupled lasers should be twice the output power of the single hybrid laser if the pump currents are the same. From Fig. 6.6, we can find that the addition efficiency of the coupled lasers is ~90% at I = 100 mA. In Fig. 6.6(b), the solid blue line shows the optical spectrum for the coupled lasers with the asymmetric mirror losses. For comparison, the dashed black line represents the optical spectrum of the coupled lasers with the symmetric mirror losses, which is the same with the one shown in Fig. 6.3(e). Different from the coupled lasers with the symmetric mirror losses, the single mode operation is obtained for the coupled lasers with the asymmetric mirror losses. This is because the effective cavity length of the F-P resonator is changed when we narrow down part of the output waveguide width to reduce the reflection. The cavity length differences between the two coupled resonators result in the Vernier effect that improves the longitudinal mode discrimination. Thus, with the PT symmetry

breaking, the single mode operation is achieved. The FSR of the hybrid laser is about 0.11 nm. There is only one lasing peak with high-SMSR shown by the solid blue line in Fig. 6.6(b), which demonstrates that the single longitudinal mode laser operation is indeed obtained. The total wavelength range in Fig. 6.6(b) is only 0.6 nm. The resolution (0.02 nm) of our optical spectrum analyzer is set at the instrument limit, which leads to the irregular lineshape of the spectra shown in Fig. 6.6(b).

6.5 Methods

The passive chip is a $Si_3N_4/SiO_2/Si$ chip where the SiO_2 cladding layer is 4 μm thick. The width and height of the single mode Si_3N_4 waveguide is 800 nm and 300 nm, respectively. The gap between the waveguides at the coupling region is about 900 nm. The active alignment method is used to demonstrate the hybridly integrated non-Hermitian optical system. The two RSOAs and the Si_3N_4 passive chip are placed on the xyz stages separately. The RSOAs are directly coupled to the Si_3N_4 passive waveguide through a mode converter that is used to improve the coupling efficiency. We use the angle-cleaved ridge waveguides and AR coated chip facets in the active and passive chips to eliminate the reflection at the interface between the chips. The interface reflectivity measured between the two chips is less than 0.01%.

The Si_3N_4 passive waveguide fabrication is described here. We first use a Tystar Nitride LPCVD tool to deposit a 300 nm thick Si_3N_4 film on a SiO_2/Si wafer. A JEOL JBX-9300FS EBL system is used to pattern the Si_3N_4 layer with ZEP520A (by Zeon

cooperation) as the e-beam resist. We transfer the pattern to the Si_3N_4 layer using plasma etching with a CF_4/CHF_3 gas mixture in an Oxford Endpoint reactive ion etching machine. Then, we remove the e-beam resist. A 2 μm thick SiO_2 layer is deposited on the Si_3N_4 layer using plasma-enhanced chemical vapor deposition process. For the coupled cavities with the symmetric mirror losses at the two output ports, the mirror optical feedbacks at the two output ports are provided through the cleaved facets. For the coupled cavities with the asymmetric mirror losses, one of the output ports is made to be lossy by narrowing down its output waveguide width, while the other output port provides the optical feedback for lasing through the cleaved facet.

The modal analysis of the coupled F-P resonators in the InP-Si_3N_4 platform is studied in the time domain. The eigenfrequencies associated with the supermodes in the coupled cavities for a specific order longitudinal mode can be obtained by solving the eigenvalue problem of the coupled mode equations:

$$\frac{da_1}{dt} = -i\omega_1 a_1 + \gamma_1 a_1 + i\kappa_{12} a_2 \tag{6.3}$$

$$\frac{da_2}{dt} = -i\omega_2 a_2 + \gamma_2 a_2 + i\kappa_{21} a_1 \tag{6.4}$$

Here, a_1 and a_2 denote the complex amplitudes for the slowly-varying electric fields in the two resonators respectively. $\omega_{1,2}$ denote each resonator's natural resonance frequency. κ_{12}, κ_{21} are the coupling coefficients, and γ_1, γ_2 are the gain or loss

coefficients. Here, we ignore all the non-linear effects. If $\omega_1 = \omega_2 = \omega_0$, $\kappa_{12} = \kappa_{21} = \kappa$, the eigenfrequencies of supermodes in coupled cavities, $\omega_{\pm}$, are given by:

$$\omega_{\pm} = \omega_0 + i\frac{(\gamma_1 + \gamma_2)}{2} \pm \sqrt{\kappa^2 - \left(\frac{\gamma_1 - \gamma_2}{2}\right)^2} \tag{6.5}$$

Figure 6.2 shows the variation of the real and imaginary parts of the eigenfrequencies for the two supermodes formed in the coupled F-P resonators as a function of the gain or loss contrast. The complex eigenfrequencies of the supermodes and the corresponding mode profiles are also calculated by using the FEM (COMSOL Multiphysics).

6.6 Conclusion

In summary, we have demonstrated the coupled F-P resonators as a novel non-Hermitian optical system in the InP-Si_3N_4 hybrid platform. The electrically pumped active elements are used to provide optical gain for the coupled InP-Si_3N_4 cavities. With the asymmetric injection currents, the PT symmetry breaking is obtained, and the exceptional points are directly accessed in the hybrid platform. Besides, in the same platform, we break the PT symmetry by introducing the asymmetric mirror losses. The PT symmetry breaking with the asymmetric mirror losses leads to the coherent addition of the two active chips due to the lasing mode selection. The electrically pumped,

hybridly integrated chip-scale non-Hermitian optical systems not only provide a promising solution for the lasing mode control and selection, but also create a new platform for other emerging non-Hermitian devices, such as the CPA-lasers, topological insulator lasers, and active sensors with high order EPs.

CHAPTER SEVEN

CONCLUSTION AND FUTURE WORKS

In conclusion, we have demonstrated the hybrid integration of a low-loss, passive Si_3N_4 external cavity with two RSOAs simultaneously in silicon photonics platform to obtain the ultra-narrow laser linewidth and wide wavelength tunability. The hybrid integration allows multiple active chips with different types of gain media to be integrated easily in the platform at the same time. In addition to the InP chip operating around 1.55 μm, a GaAs chip at 1 μm is also integrated in the same hybrid platform. Single frequency lasing at 1.55 μm and 1 μm has been demonstrated simultaneously on a single chip with the spectral linewidths of 18-kHz and 70-kHz, side mode suppression ratio of 52 dB and 46 dB, and tuning range of 46 nm and 38 nm, respectively. The beam steering is also obtained by using the dual-band diode lasers combined with a waveguide grating.

In addition, we experimentally demonstrate the coherent combining of two RSOAs in an InP-Si_3N_4 hybrid platform. The CBC is realized by controlling the mirror loss distribution of the coupled cavities, due to the tendency of the lasing to self-adaptively operate with minimum losses. From the measurement results, we show that the combining efficiency of our system is ~92% at ~2× threshold. We also propose a fully integrated coherently combined laser array system on a single chip. The diode laser based chip-scale CBC system provides the desired system compactness by removing the need of external free-space/fiber components and coupling optics.

Besides, tunable narrow linewidth diode lasers based on quantum-dot RSOAs at 1.3 μm are demonstrated through hybrid integration in silicon nitride photonics platform. We also demonstrate a hybridly integrated diode laser in the silicon-carbide-on-insulator platform and lithium-niobate-on-insulator platform through edge coupling. An InP based gain chip is butt coupled to a low loss silicon-carbide or lithium-niobate waveguide. The optical feedbacks of the laser cavity are provided by the high reflection coated back facet of the gain chip and the loop mirror in the passive chip.

At last, we have demonstrated the coupled F-P resonators as a novel non-Hermitian optical system in the InP-Si_3N_4 hybrid platform. The electrically pumped active elements are used to provide optical gain for the coupled InP-Si_3N_4 cavities. With the asymmetric injection currents, the PT symmetry breaking is obtained, and the exceptional points are directly accessed in the hybrid platform. Besides, in the same platform, we break the PT symmetry by introducing the asymmetric mirror losses. The PT symmetry breaking with the asymmetric mirror losses leads to the coherent addition of the two active chips due to the lasing mode selection. The electrically pumped, hybridly integrated chip-scale non-Hermitian optical systems not only provide a promising solution for the lasing mode control and selection, but also create a new platform for other emerging non-Hermitian devices, such as the CPA-lasers, topological insulator lasers, and active sensors with high order EPs.

In the future, to further improve the operation performance of the laser sources, we plan to optimize our active chip design. The active component needs a highly efficient epitaxial structure and larger aperture than the typical ridge waveguide laser, to keep

electrical and optical power densities low. We plan to optimize the Epi wafer structure and the vertical optical mode of the active gain chip.

APPENDICES

Appendix A

Flip-chip bonding method for edge coupling

For the flip-chip bonding method, a diode laser chip is flip-chip bonded on a silicon substrate. Misalignment during the bonding process can result in extra coupling losses. For the horizontal alignment, sub-micron (±0.5 μm) alignment accuracy is usually enough to obtain good coupling efficiency. And this accuracy is feasible with a well-maintained flip-chip bonding system. Since the vertical size of the laser mode is smaller and the thickness of the Si/Si_3N_4 waveguide is less than 800 nm, the vertical alignment accuracy is more critical for efficient coupling. Multiple steps of etching and film deposition during the fabrication process often present challenges for accurate vertical alignment. In addition, the solder layer thickness could vary during the bonding process, which further increases the difficulty of good vertical alignment. Here, we use dry-etched silicon pedestals on the passive chip to assist the bonding process and precisely control the vertical alignment of the laser diode chip.

Figure A.1(a) shows the schematic plot of the laser diode array with an insulation layer and bonding alignment markers. Each emitter in the array is a single mode ridge waveguide laser with ~4 μm width and 800 nm height. The pitch of the array is 20 μm. Figures A.1(b) and (c) show the schematic plot of the silicon chip before the hybrid integration. After the fabrication of all the passive components, we etch through all the oxide layers until we reach the silicon substrate along the edge of the spot-size converter. Then the exposed silicon substrate is shallowly etched for the subsequent deposition of

the bonding pad and solder. During the shallow silicon etch, several pedestals are also formed as shown in Fig. A.1(b). Meanwhile, we can divide the laser diode chip into the functional region (ridge waveguides with top metal contacts) and bonding region (unetched III-V region with insulation layers). The bonding region is the area that will be in direct contact with the pedestals. Since these silicon pedestals determine the final solder layer thickness during the bonding, the top pedestal surface will be used as the reference plane for the bonding alignment. In this way, the vertical position of the laser chip is only determined by the thickness of the insulation layer in the bonding region on the laser chip. Therefore, during the III-V fabrication, the accumulated thickness in the functional region is not critical since it can be compensated by the etched space in the silicon substrate. Since the bonding region is away from the functional region and usually with simple or no patterns, its thickness can be well-controlled, allowing for the high accuracy vertical bonding alignment. Figure A.1(d) shows the schematic plot of a laser diode on a silicon chip after hybrid integration. It is clear that the vertical position of the laser chip is entirely determined by the silicon pedestals and III-V insulation layers.

The longitudinal alignment during the bonding process requires precise control of the facet location relative to the alignment markers for both chips and the alignment error, i.e. the gap distance between the two chips, should be less than 1~2 μm based on our calculation. For the passive chip, the etched facet is defined by lithography, so its position is accurately controlled. But for the laser chip, the facet is usually created by a "scribe and break" cleaving process. Since the diamond tip for the scriber has a typical radius of ~10 μm and the exact breaking location is hard to be controlled, the laser facet

relative position usually has an uncertainty of 2~5 μm. Here, we propose a micro-cleaving method to overcome this problem and use lithographically defined cleaving markers to accurately control the laser facet location.

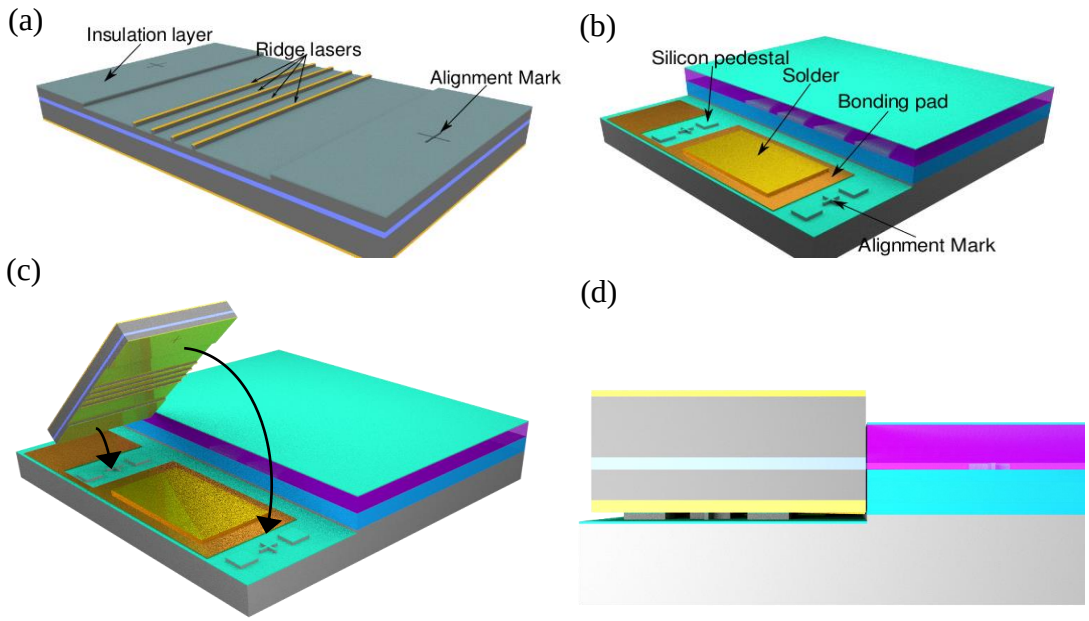

Figure A.1: Direct chip-to-chip coupling obtained by flip-chip bonding. (a) Schematic plot of a laser diode array. (b) Schematic plot of a fabricated silicon chip before bonding. (c) Flip-chip bonding process. (d) Side view of a laser diode chip on the silicon platform after hybrid integration.

(a)

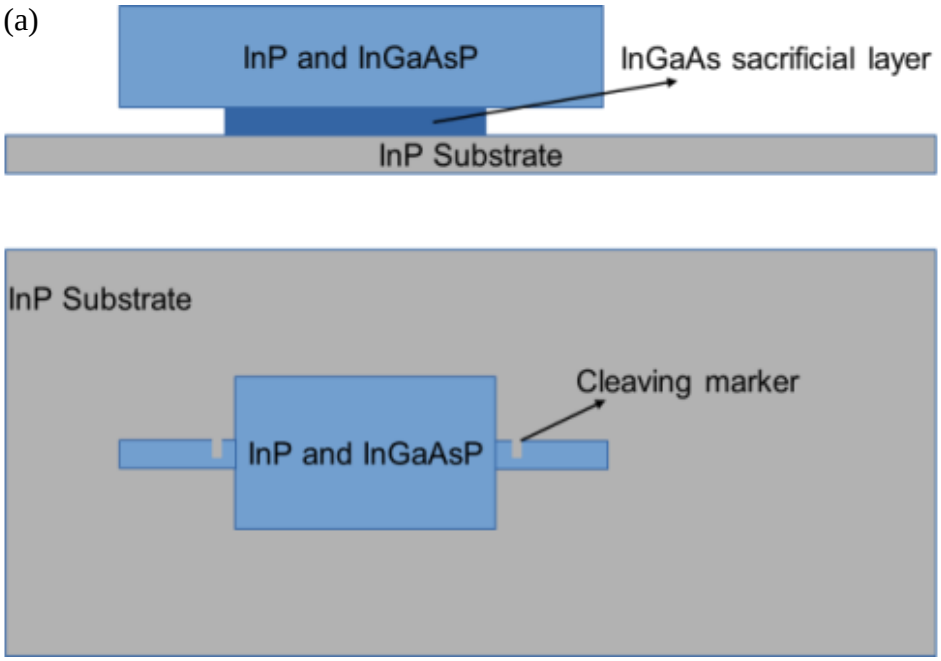
InP and InGaAsP
InGaAs sacrificial layer
InP Substrate
InP Substrate
Cleaving marker
InP and InGaAsP

(b)

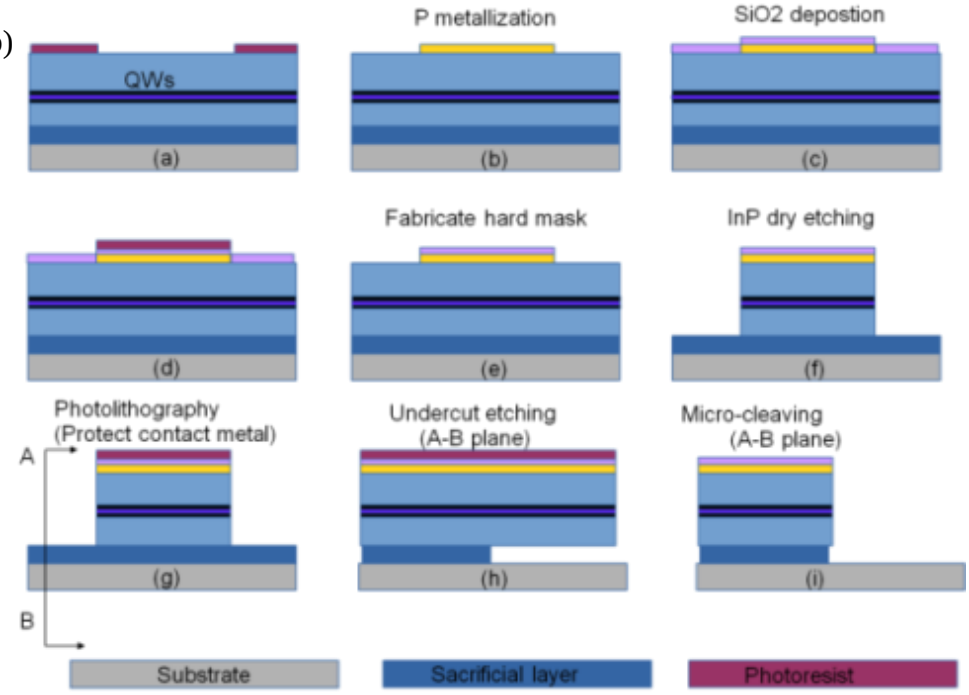
QWs
(a)
P metallization
(b)
SiO2 depostion
(c)
(d)
Fabricate hard mask
(e)
InP dry etching
(f)
Photolithography
(Protect contact metal)
A
B
(g)
Undercut etching
(A-B plane)
(h)
Micro-cleaving
(A-B plane)
(i)
Substrate
Sacrificial layer
Photoresist

(c)

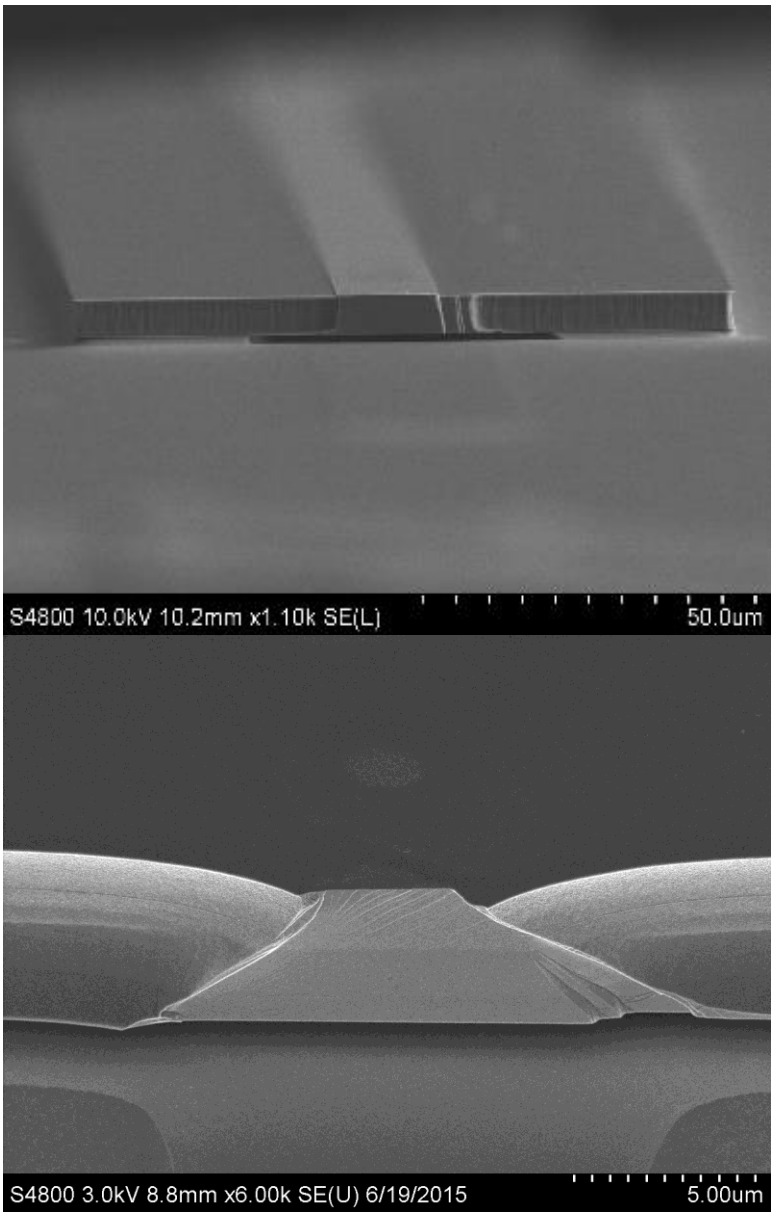

Figure A.2: (a) Side and top view of micro-cleaved lasers before the cantilever cleaving. (b) Detailed fabrication processes for creating micro-cleaved mirrors. (c) SEM image of a micro-cleaved laser facet.

The key to obtain micro-cleaved mirror facets is to selectively etch a sacrificial layer underneath the regular laser structure, resulting in a suspended cantilever with cleaving markers, as shown in Fig. A.2(a). Both the cantilever and cleaving markers are defined by lithography and dry etching. This cantilever can be cleaved preferentially along the notch markers by applying mechanical stress (ultrasonic vibration or probe tip pressing). Since we focus on 1.55 μm light sources, we use InP/InGaAsP material systems for the laser heterostrucutre. We choose lattice-matched InGaAs as the sacrificial layer, because it can be selectively etched by using the H_2SO_4:H_2O_2:H_2O solution. The detailed fabrication processes are shown in Fig. A.2(b). In Fig. A.2(b), we mainly focus on the fabrication processes that create a mesa with micro-cleaved facets. It should be pointed out that various optical structures, such as the ridge waveguide and Bragg gratings, for the laser mode control can be fabricated on the mesa before this step. We start with the top side metallization for the active devices on the mesa and then deposit SiO_2 as hard mask to etch the mesa, cantilever, and cleaving marker. We release the cantilever by selectively removing the InGaAs sacrificial layer underneath it. The last step is to apply mechanical stress to cleave the released cantilever along the cleaving marker. We will deposit a thin layer of alumina (~20 nm) on the cleaved facet for protection by use of atomic layer deposition before reducing the thickness of the substrate. Figure A.2(c) shows the SEM image of a micro-cleaved laser with the precisely-controlled facet position.

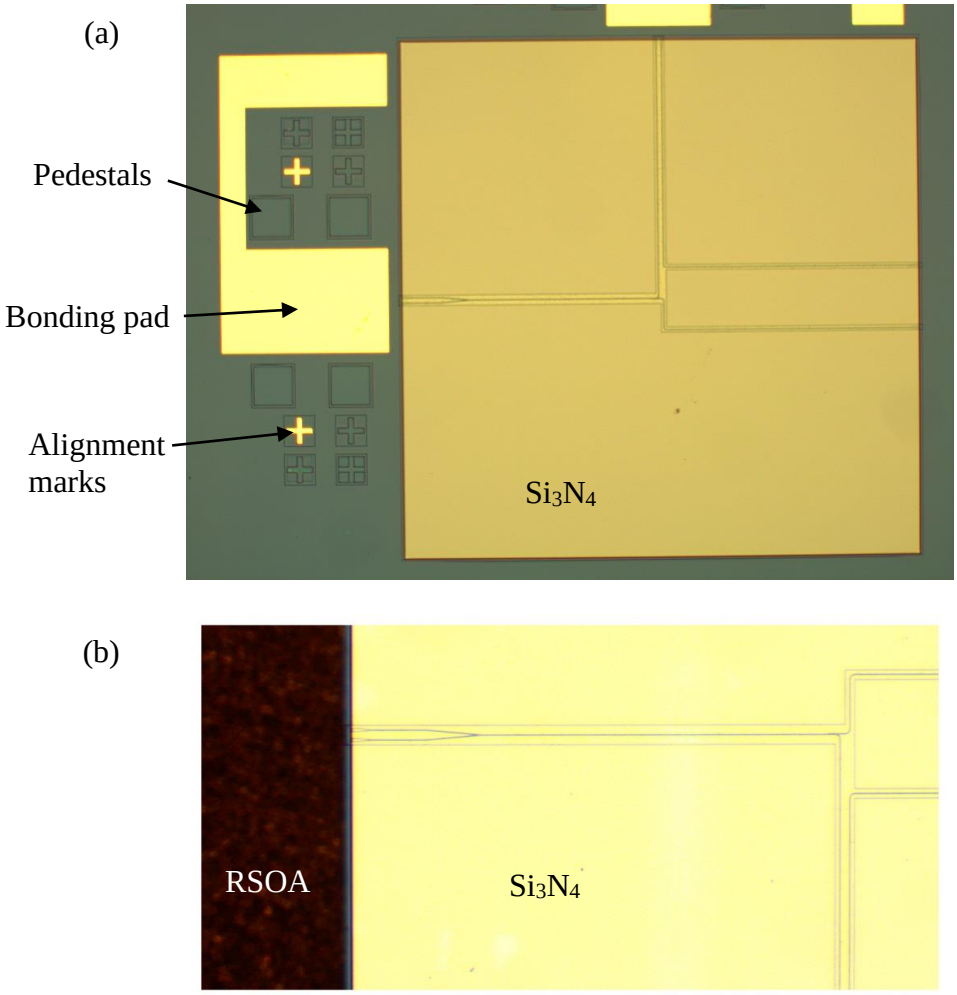

Figure A.3: Microscopic images. (a) waveguide platform of PICs fabricated.

(b) hybridly integrated structure after flip-chip bonding.

We show the preliminary fabrication results in Fig. A.3. Figure A.3(a) shows the layout of the passive PICs on a silicon chip. The waveguides and other passive components are fabricated with the silicon nitride core and BOX lower cladding. The waveguide facet and recessed area for the laser chip bonding is created by dry etching. We fabricate the bonding pad and alignment markers on the exposed silicon substrate for

subsequent flip chip bonding. The support pillars are also etched in the silicon substrate to obtain the accurate vertical alignment. Figure A.3(b) shows the laser chip bonded to the silicon chip with passive PICs.

Appendix B

Publication list

Refereed journal publications with the lead author

1. Y. Zhu, S. Zeng, and L. Zhu, "Hybridly integrated diode lasers based on quantum-dot RSOA and Si_3N_4 microresonators for beam steering," submitted, (2019).

2. Y. Zhu, T. Fan, L. Zhu and A. Adibi, "Hybridly integrated diode lasers in silicon carbide-on-insulator platform," submitted, (2019).

3. Y. Zhu and L. Zhu, "Narrow-linewidth, tunable external cavity dual-band diode lasers through InP/GaAs- Si_3N_4 hybrid integration," Opt. Express, (2019).

4. Y. Zhu and L. Zhu, "Accessing the exceptional points in coupled Fabry-Perot resonators through hybrid integration," ACS Photonics 5, (2018).

5. Y. Zhu and L. Zhu, "Integrated single frequency, high power laser sources based on monolithic and hybrid coherent beam combining," IEEE J. Sel. Top. Quantum Electron 24(6), (2018).

6. Y. Zhu, Y. Zhao, and L. Zhu, "Loss induced coherent combining in InP-Si_3N_4 hybrid platform," Sci. Rep. 8(1), 878 (2018).

7. Y. Zhu, Y. Zhao, and L. Zhu, "Modal discrimination in parity-time-symmetric single microring lasers," IEEE Photonics J. 9(6), 1-8 (2017).

8. Y. Zhu, Y. Zhao, and L. Zhu, "Two-dimensional photonic crystal Bragg lasers with triangular lattice for monolithic coherent beam combining," Sci. Rep. 7(1), 10610 (2017).

9. Y. Zhu, Y. Zhao, J. Fan, and L. Zhu, “Modal gain analysis of Parity-Time-Symmetric distributed feedback lasers,” IEEE J. Sel. Top. Quantum Electron 22(5), 5-11 (2016).

REFERENCES

1. L. A. Coldren, S. W. Corzine, and M. L. Mashanovitch, *Diode lasers and photonic integrated circuits* (John Wiley & Sons, 2012), Vol. 218.
2. S. E. Miller, "INTEGRATED OPTICS - AN INTRODUCTION," Bell System Technical Journal **48**, 2059 (1969).
3. L. A. Coldren, S. C. Nicholes, L. Johansson, S. Ristic, R. S. Guzzon, E. J. Norberg, and U. Krishnamachari, "High Performance InP-Based Photonic ICs—A Tutorial," Journal of Lightwave Technology **29**, 554-570 (2011).
4. D. Liang and J. E. Bowers, "Photonic integration: Si or InP substrates?," Electronics Letters **45**, 578-580 (2009).
5. R. Nagarajan, M. Kato, J. Pleumeekers, P. Evans, S. Corzine, S. Hurtt, A. Dentai, S. Murthy, M. Missey, R. Muthiah, R. A. Salvatore, C. Joyner, R. Schneider, M. Ziari, F. Kish, and D. Welch, "InP Photonic Integrated Circuits," Ieee Journal of Selected Topics in Quantum Electronics **16**, 1113-1125 (2010).
6. T. L. Koch and U. Koren, "SEMICONDUCTOR PHOTONIC INTEGRATED-CIRCUITS," Ieee Journal of Quantum Electronics **27**, 641-653 (1991).
7. W. Bogaerts, D. Taillaert, B. Luyssaert, P. Dumon, J. Van Campenhout, P. Bienstman, D. Van Thourhout, R. Baets, V. Wiaux, and S. Beckx, "Basic structures for photonic integrated circuits in silicon-on-insulator," Optics Express **12**, 1583-1591 (2004).

8. D. J. Moss, R. Morandotti, A. L. Gaeta, and M. Lipson, "New CMOS-compatible platforms based on silicon nitride and Hydex for nonlinear optics," Nature Photonics **7**, 597-607 (2013).

9. A. J. Zilkie, P. Seddighian, B. J. Bijlani, W. Qian, D. C. Lee, S. Fathololoumi, J. Fong, R. Shafiiha, D. Feng, B. J. Luff, X. Zheng, J. E. Cunningham, A. V. Krishnamoorthy, and M. Asghari, "Power-efficient III-V/Silicon external cavity DBR lasers," Optics Express **20**, 23456-23462 (2012).

10. A. A. Liles, K. Debnath, and L. O'Faolain, "Lithographic wavelength control of an external cavity laser with a silicon photonic crystal cavity-based resonant reflector," Optics Letters **41**, 894-897 (2016).

11. A. Verdier, G. de Valicourt, R. Brenot, H. Debregeas, P. Dong, M. Earnshaw, H. Carrere, and Y. K. Chen, "Ultrawideband Wavelength-Tunable Hybrid External-Cavity Lasers," Journal of Lightwave Technology **36**, 37-43 (2018).

12. A. W. Fang, E. Lively, H. Kuo, D. Liang, and J. E. Bowers, "A distributed feedback silicon evanescent laser," Optics Express **16**, 4413-4419 (2008).

13. X. K. Sun, A. Zadok, M. J. Shearn, K. A. Diest, A. Ghaffari, H. A. Atwater, A. Scherer, and A. Yariv, "Electrically pumped hybrid evanescent Si/InGaAsP lasers," Optics Letters **34**, 1345-1347 (2009).

14. X. Z. Zheng, I. Shubin, J. H. Lee, S. Y. Lin, Y. Luo, J. Yao, S. S. Djordjevic, J. Bovington, D. Y. Lee, H. D. Thacker, C. Q. Zhang, K. Raj, J. E. Cunningham, and A. V. Krishnamoorthy, "III-V/Si Hybrid Laser Arrays Using Back End of the

Line (BEOL) Integration," Ieee Journal of Selected Topics in Quantum Electronics **22**, 14 (2016).

15. S. Y. Yang, Y. Zhang, D. W. Grund, G. A. Ejzak, Y. Liu, A. Novack, D. Prather, A. E. J. Lim, G. Q. Lo, T. Baehr-Jones, and M. Hochberg, "A single adiabatic microring-based laser in 220 nm silicon-on-insulator," Optics Express **22**, 1172-1180 (2014).
16. N. Kobayashi, K. Sato, M. Namiwaka, K. Yamamoto, S. Watanabe, T. Kita, H. Yamada, and H. Yamazaki, "Silicon Photonic Hybrid Ring-Filter External Cavity Wavelength Tunable Lasers," Journal of Lightwave Technology **33**, 1241-1246 (2015).
17. X. S. Luo, Y. B. Cheng, J. F. Song, T. Y. Liow, Q. J. Wang, and M. B. Yu, "Wafer-Scale Dies-Transfer Bonding Technology for Hybrid III/V-on-Silicon Photonic Integrated Circuit Application," Ieee Journal of Selected Topics in Quantum Electronics **22**, 12 (2016).
18. T. Komljenovic, S. Srinivasan, E. Norberg, M. Davenport, G. Fish, and J. E. Bowers, "Widely Tunable Narrow-Linewidth Monolithically Integrated External-Cavity Semiconductor Lasers," Ieee Journal of Selected Topics in Quantum Electronics **21**, 9 (2015).
19. G. de Valicourt, C. M. Chang, M. S. Eggleston, A. Melikyan, C. Zhu, J. Lee, J. E. Simsarian, S. Chandrasekhar, J. H. Sinsky, K. W. Kim, P. Dong, A. Maho, A. Verdier, R. Brenot, and Y. K. Chen, "Photonic Integrated Circuit Based on

Hybrid III-V/Silicon Integration," Journal of Lightwave Technology **36**, 265-273 (2018).

20. J. C. Hulme, J. K. Doylend, and J. E. Bowers, "Widely tunable Vernier ring laser on hybrid silicon," Optics Express **21**, 19718-19722 (2013).

21. F. E. Doany, R. A. Budd, L. Schares, T. N. Huynh, M. G. Wood, D. M. Kuchta, N. Dupuis, C. L. Schow, B. G. Lee, M. Module, A. Sigmund, W. Rehbein, T. Y. Liow, L. W. Luo, G. Q. Lo, and I. C. Soc, "A Four-Channel Silicon Photonic Carrier With Flip-Chip Integrated Semiconductor Optical Amplifier (SOA) Array Providing > 10-dB Gain," in *2016 Ieee 66th Electronic Components and Technology Conference* (Ieee Computer Soc, Los Alamitos, 2016), pp. 1061-1068.

22. S. Keyvaninia, G. Roelkens, D. Van Thourhout, C. Jany, M. Lamponi, A. Le Liepvre, F. Lelarge, D. Make, G. H. Duan, D. Bordel, and J. M. Fedeli, "Demonstration of a heterogeneously integrated III-V/SOI single wavelength tunable laser," Optics Express **21**, 3784-3792 (2013).

23. T. Komljenovic, M. Davenport, J. Hulme, A. Y. Liu, C. T. Santis, A. Spott, S. Srinivasan, E. J. Stanton, C. Zhang, and J. E. Bowers, "Heterogeneous Silicon Photonic Integrated Circuits," Journal of Lightwave Technology **34**, 20-35 (2016).

24. Y. Fan, R. M. Oldenbeuving, C. G. Roeloffzen, M. Hoekman, D. Geskus, R. G. Heideman, and K.-J. Boller, "290 Hz intrinsic linewidth from an integrated optical

chip-based widely tunable InP-Si 3 N 4 hybrid laser," in *Lasers and Electro-Optics (CLEO), 2017 Conference on*, (IEEE, 2017), 1-2.

25. Y. Zhu, Y. Zhao, and L. Zhu, "Coherent beam combining on silicon chip through hybrid integration," in *CLEO: Science and Innovations*, (Optical Society of America, 2017), SF1H. 1.

26. E. Dale, W. Liang, D. Eliyahu, A. A. Savchenkov, V. S. Ilchenko, A. B. Matsko, D. Seidel, and L. Maleki, "Ultra-narrow line tunable semiconductor lasers for coherent LIDAR applications," in *Imaging Systems and Applications*, (Optical Society of America, 2014), JTu2C. 3.

27. P. Del'Haye, A. Schliesser, O. Arcizet, T. Wilken, R. Holzwarth, and T. J. Kippenberg, "Optical frequency comb generation from a monolithic microresonator," Nature **450**, 1214-1217 (2007).

28. S. Clemmen, K. P. Huy, W. Bogaerts, R. G. Baets, P. Emplit, and S. Massar, "Continuous wave photon pair generation in silicon-on-insulator waveguides and ring resonators," Optics Express **17**, 16558-16570 (2009).

29. K. Kasai, M. Nakazawa, M. Ishikawa, and H. Ishii, "8 kHz linewidth, 50 mW output, full C-band wavelength tunable DFB LD array with self-optical feedback," Optics Express **26**, 5675-5685 (2018).

30. W. Liang, V. S. Ilchenko, D. Eliyahu, A. A. Savchenkov, A. B. Matsko, D. Seidel, and L. Maleki, "Ultralow noise miniature external cavity semiconductor laser," Nature Communications **6**(2015).

31. Y. Zhu, Y. Zhao, and L. Zhu, "Two-dimensional photonic crystal Bragg lasers with triangular lattice for monolithic coherent beam combining," Scientific Reports **7**(2017).

32. Y. Zhu, Y. Zhao, J. Fan, and L. Zhu, "Modal Gain Analysis of Parity-Time-Symmetric Distributed Feedback Lasers," IEEE Journal of Selected Topics in Quantum Electronics **22**, 5-11 (2016).

33. Y. Zhu and L. Zhu, "Narrow-linewidth, tunable external cavity dual-band diode lasers through InP/GaAs-Si3N4 hybrid integration," Opt Express **27**, 2354-2362 (2019).

34. Y. Zhao, Y. Zhu, and L. Zhu, "Integrated coherent combining of photonic crystal Bragg lasers with triangular lattice," in *2016 IEEE Photonics Conference (IPC)*, (IEEE, 2016), 321-322.

35. Y. Zhu and L. Zhu, "Integrated Single Frequency, High Power Laser Sources Based on Monolithic and Hybrid Coherent Beam Combining," IEEE Journal of Selected Topics in Quantum Electronics **24**, 1-8 (2018).

36. C. H. Henry, "THEORY OF THE LINEWIDTH OF SEMICONDUCTOR-LASERS," Ieee Journal of Quantum Electronics **18**, 259-264 (1982).

37. B. Liu, A. Shakouri, and J. E. Bowers, "Passive microring-resonator-coupled lasers," Applied Physics Letters **79**, 3561-3563 (2001).

38. Y. W. Fan, R. E. M. Lammerink, J. Mak, R. M. Oldenbeuving, P. J. M. van der Slot, and K. J. Boller, "Spectral linewidth analysis of semiconductor hybrid lasers

with feedback from an external waveguide resonator circuit," Optics Express **25**, 32767-32782 (2017).

39. A. H. Atabaki, E. S. Hosseini, A. A. Eftekhar, S. Yegnanarayanan, and A. Adibi, "Optimization of metallic microheaters for high-speed reconfigurable silicon photonics," Optics Express **18**, 18312-18323 (2010).

40. Y. Zhu, S. Zeng, X. Zhao, Y. Zhao, and L. Zhu, "Narrow-linewidth, tunable external cavity diode lasers through hybrid integration of quantum-well/quantum-dot SOAs with Si3N4 microresonators," in *CLEO: Science and Innovations*, (Optical Society of America, 2018), SW4B. 2.

41. B. Stern, X. Ji, A. Dutt, and M. Lipson, "Compact narrow-linewidth integrated laser based on a low-loss silicon nitride ring resonator," Optics letters **42**, 4541-4544 (2017).

42. Y. Zhu, Y. Zhao, and L. Zhu, "Loss induced coherent combining in InP-Si3N4 hybrid platform," Scientific Reports **8**, 7 (2018).

43. B. Sumpf, K. H. Hasler, P. Adamiec, F. Bugge, J. Fricke, P. Ressel, H. Wenzel, G. Erbert, and G. Trankle, "1060 nm DBR tapered lasers with 12 W output power and a nearly diffraction limited beam quality," in *Novel in-Plane Semiconductor Lasers Viii*, A. A. Belyanin and P. M. Smowton, eds. (Spie-Int Soc Optical Engineering, Bellingham, 2009).

44. P. Dupriez, A. Piper, A. Malinowski, J. K. Sahu, M. Ibsen, B. C. Thomsen, Y. Jeong, L. M. B. Hickey, M. N. Zervas, J. Nilsson, and D. J. Richardson, "High average power, high repetition rate, picosecond pulsed fiber master oscillator

power amplifier source seeded by a gain-switched laser diode at 1060 nm," Ieee Photonics Technology Letters **18**, 1013-1015 (2006).

45. K. Nemoto, T. Kita, and H. Yamada, "Narrow-Spectral-Linewidth Wavelength-Tunable Laser Diode with Si Wire Waveguide Ring Resonators," Applied Physics Express **5**(2012).

46. S. Dhoore, L. Y. Li, A. Abbasi, G. Roelkens, and G. Morthier, "Demonstration of a Discretely Tunable III-V-on-Silicon Sampled Grating DFB Laser," Ieee Photonics Technology Letters **28**, 2343-2346 (2016).

47. J. T. Bovington, M. J. R. Heck, and J. E. Bowers, "Heterogeneous lasers and coupling to Si3N4 near 1060 nm," Optics Letters **39**, 6017-6020 (2014).

48. L. Goldberg, J. Koplow, D. G. Lancaster, R. F. Curl, and F. K. Tittel, "Mid-infrared difference-frequency generation source pumped by a 1.1-1.5-mu m dual-wavelength fiber amplifier for trace-gas detection," Optics Letters **23**, 1517-1519 (1998).

49. B. G. Lee, J. Kansky, A. K. Goyal, C. Pflugl, L. Diehl, M. A. Belkin, A. Sanchez, and F. Capasso, "Beam combining of quantum cascade laser arrays," Optics Express **17**, 16216-16224 (2009).

50. I. H. White, "A MULTICHANNEL GRATING CAVITY LASER FOR WAVELENGTH DIVISION MULTIPLEXING APPLICATIONS," Journal of Lightwave Technology **9**, 893-899 (1991).

51. Y. Zhao, Y. Zhu, and L. Zhu, "Hybrid integration for coherent laser beam combining on silicon photonics platform," in *Photonics Conference (IPC), 2016 IEEE*, (IEEE, 2016), 633-634.

52. H. Guan, A. Novack, T. Galfsky, Y. J. Ma, S. Fathololoumi, A. Horth, T. N. Huynh, J. Roman, R. Z. Shi, M. Caverley, Y. Liu, T. Baehr-Jones, K. Bergman, and M. Hochberg, "Widely-tunable, narrow-linewidth III-V/silicon hybrid external-cavity laser for coherent communication," Optics Express **26**, 7920-7933 (2018).

53. Y. Zhu, S. Zeng, Y. Zhao, and L. Zhu, "Hybrid integration of active semiconductor devices with passive micro/nano optical structures for emerging applications," in *Nanoengineering: Fabrication, Properties, Optics, Thin Films, and Devices XVI*, (International Society for Optics and Photonics, 2019), 1108908.

54. D. Kwong, A. Hosseini, J. Covey, Y. Zhang, X. Xu, H. Subbaraman, and R. T. Chen, "On-chip silicon optical phased array for two-dimensional beam steering," Opt Lett **39**, 941-944 (2014).

55. K. Kondo, T. Tatebe, S. Hachuda, H. Abe, F. Koyama, and T. Baba, "Fan-beam steering device using a photonic crystal slow-light waveguide with surface diffraction grating," Opt Lett **42**, 4990-4993 (2017).

56. K. Van Acoleyen, W. Bogaerts, and R. Baets, "Two-Dimensional Dispersive Off-Chip Beam Scanner Fabricated on Silicon-On-Insulator," IEEE Photonics Technology Letters **23**, 1270-1272 (2011).

57. H. Ito, T. Tatebe, H. Abe, and T. Baba, "Wavelength-division multiplexing Si photonic crystal beam steering device for high-throughput parallel sensing," Opt Express **26**, 26145-26155 (2018).

58. Y. Zhu, S. Zeng, Y. Zhao, and L. Zhu, "Hybrid Integration of Multi-Band, Tunable External-Cavity Diode Lasers for Wide-Angle Beam Steering," in *CLEO: Science and Innovations*, (Optical Society of America, 2019), SF3N. 3.

59. Y. Zhu and L. Zhu, "Accessing the Exceptional Points in Coupled Fabry-Perot Resonators through Hybrid Integration," Acs Photonics **5**, 4920-4927 (2018). https://pubs.acs.org/articlesonrequest/AOR-sIeq6WvutygwcChBUQc6

60. A. Shirakawa, T. Saitou, T. Sekiguchi, and K. Ueda, "Coherent addition of fiber lasers by use of a fiber coupler," Optics Express **10**, 1167-1172 (2002).

61. T. W. Wu, W. Z. Chang, A. Galvanauskas, and H. G. Winful, "Model for passive coherent beam combining in fiber laser arrays," Optics Express **17**, 19509-19518 (2009).

62. C. J. Corcoran and F. Durville, "Experimental demonstration of a phase-locked laser array using a self-Fourier cavity," Applied Physics Letters **86**, 3 (2005).

63. C. Changhasnain, D. F. Welch, D. R. Scifres, J. R. Whinnery, A. Dienes, and R. D. Burnham, "DIFFRACTION-LIMITED EMISSION FROM A DIODE-LASER ARRAY IN AN APERTURED GRADED-INDEX LENS EXTERNAL CAVITY," Applied Physics Letters **49**, 614-616 (1986).

64. B. Liu, Y. Liu, and Y. Braiman, "Coherent beam combining of high power broad-area laser diode array with a closed-V-shape external Talbot cavity," Optics Express **18**, 7361-7368 (2010).

65. O. Andrusyak, V. Smirnov, G. Venus, V. Rotar, and L. Glebov, "Spectral Combining and Coherent Coupling of Lasers by Volume Bragg Gratings," Ieee Journal of Selected Topics in Quantum Electronics **15**, 344-353 (2009).

66. J. R. Leger, G. J. Swanson, and W. B. Veldkamp, "COHERENT BEAM ADDITION OF GAALAS LASERS BY BINARY PHASE GRATINGS," Applied Physics Letters **48**, 888-890 (1986).

67. A. J. Ward, D. J. Robbins, G. Busico, E. Barton, L. Ponnampalam, J. P. Duck, N. D. Whitbread, P. J. Williams, D. C. J. Reid, A. C. Carter, and M. J. Wale, "Widely tunable DS-DBR laser with monolithically integrated SOA: Design and performance," Ieee Journal of Selected Topics in Quantum Electronics **11**, 149-156 (2005).

68. T. Shimizu, N. Hatori, M. Okano, M. Ishizaka, Y. Urino, T. Yamamoto, M. Mori, T. Nakamura, and Y. Arakawa, "Multichannel and high-density hybrid integrated light source with a laser diode array on a silicon optical waveguide platform for interchip optical interconnection," Photonics Research **2**, A19-A24 (2014).

69. R. Nagy, M. Widmann, M. Niethammer, D. B. Dasari, I. Gerhardt, Ö. O. Soykal, M. Radulaski, T. Ohshima, J. Vučković, and N. T. Son, "Quantum properties of dichroic silicon vacancies in silicon carbide," Physical Review Applied **9**, 034022 (2018).

70. A. Boes, B. Corcoran, L. Chang, J. Bowers, and A. Mitchell, "Status and potential of lithium niobate on insulator (LNOI) for photonic integrated circuits," Laser & Photonics Reviews **12**, 1700256 (2018).

71. C. M. Bender and S. Boettcher, "Real spectra in non-Hermitian Hamiltonians having PT symmetry," Phys Rev Lett **80**, 5243-5246 (1998).

72. C. M. Bender, D. C. Brody, and H. F. Jones, "Complex extension of quantum mechanics," Physical Review Letters **89**(2002).

73. H. Xu, D. Mason, L. Jiang, and J. G. Harris, "Topological energy transfer in an optomechanical system with exceptional points," Nature **537**, 80-83 (2016).

74. J. Doppler, A. A. Mailybaev, J. Bohm, U. Kuhl, A. Girschik, F. Libisch, T. J. Milburn, P. Rabl, N. Moiseyev, and S. Rotter, "Dynamically encircling an exceptional point for asymmetric mode switching," Nature **537**, 76-79 (2016).

75. S. Klaiman and L. S. Cederbaum, "Non-Hermitian Hamiltonians with space-time symmetry," Physical Review A **78**, 062113 (2008).

76. S. Longhi, "Optical Realization of Relativistic Non-Hermitian Quantum Mechanics," Physical Review Letters **105**(2010).

77. H. Benisty, A. Degiron, A. Lupu, A. De Lustrac, S. Chenais, S. Forget, M. Besbes, G. Barbillon, A. Bruyant, S. Blaize, and G. Lerondel, "Implementation of PT symmetric devices using plasmonics: principle and applications," Optics Express **19**, 18004-18019 (2011).

78. Y. L. Xu, W. S. Fegadolli, L. Gan, M. H. Lu, X. P. Liu, Z. Y. Li, A. Scherer, and Y. F. Chen, "Experimental realization of Bloch oscillations in a parity-time synthetic silicon photonic lattice," Nat Commun **7**, 11319 (2016).

79. S. Klaiman, U. Guenther, and N. Moiseyev, "Visualization of branch points in PT-symmetric waveguides," Physical Review Letters **101**(2008).

80. L. Chang, X. Jiang, S. Hua, C. Yang, J. Wen, L. Jiang, G. Li, G. Wang, and M. Xiao, "Parity–time symmetry and variable optical isolation in active–passive-coupled microresonators," Nature Photonics **8**, 524-529 (2014).

81. B. Peng, Ş. K. Özdemir, F. Lei, F. Monifi, M. Gianfreda, G. L. Long, S. Fan, F. Nori, C. M. Bender, and L. Yang, "Parity–time-symmetric whispering-gallery microcavities," Nature Physics **10**, 394-398 (2014).

82. X. Zhou and Y. D. Chong, "PT symmetry breaking and nonlinear optical isolation in coupled microcavities," Opt Express **24**, 6916-6930 (2016).

83. L. Feng, Y. L. Xu, W. S. Fegadolli, M. H. Lu, J. E. B. Oliveira, V. R. Almeida, Y. F. Chen, and A. Scherer, "Experimental demonstration of a unidirectional reflectionless parity-time metamaterial at optical frequencies," Nature Materials **12**, 108-113 (2013).

84. Y. Jia, Y. Yan, S. V. Kesava, E. D. Gomez, and N. C. Giebink, "Passive Parity-Time Symmetry in Organic Thin Film Waveguides," ACS Photonics **2**, 319-325 (2015).

85. J. Gu, X. Xi, J. Ma, Z. Yu, and X. Sun, "Parity–time-symmetric circular Bragg lasers: a proposal and analysis," Scientific reports **6**, 37688 (2016).

86. Y. Yan and N. C. Giebink, "Passive PT symmetry in organic composite films via complex refractive index modulation," Advanced Optical Materials **2**, 423-427 (2014).

87. C. Hahn, Y. Choi, J. W. Yoon, S. H. Song, C. H. Oh, and P. Berini, "Observation of exceptional points in reconfigurable non-Hermitian vector-field holographic lattices," Nat Commun **7**, 12201 (2016).

88. W. J. Chen, S. K. Ozdemir, G. M. Zhao, J. Wiersig, and L. Yang, "Exceptional points enhance sensing in an optical microcavity," Nature **548**, 192-+ (2017).

89. J. Wiersig, "Enhancing the Sensitivity of Frequency and Energy Splitting Detection by Using Exceptional Points: Application to Microcavity Sensors for Single-Particle Detection," Physical Review Letters **112**(2014).

90. B. Peng, S. K. Ozdemir, S. Rotter, H. Yilmaz, M. Liertzer, F. Monifi, C. M. Bender, F. Nori, and L. Yang, "Loss-induced suppression and revival of lasing," Science **346**, 328-332 (2014).

91. K. H. Kim, M. S. Hwang, H. R. Kim, J. H. Choi, Y. S. No, and H. G. Park, "Direct observation of exceptional points in coupled photonic-crystal lasers with asymmetric optical gains," Nature Communications **7**(2016).

92. M. Liertzer, L. Ge, A. Cerjan, A. D. Stone, H. E. Tureci, and S. Rotter, "Pump-induced exceptional points in lasers," Phys Rev Lett **108**, 173901 (2012).

93. M. Brandstetter, M. Liertzer, C. Deutsch, P. Klang, J. Schoberl, H. E. Tureci, G. Strasser, K. Unterrainer, and S. Rotter, "Reversing the pump dependence of a laser at an exceptional point," Nat Commun **5**, 4034 (2014).

94. L. Feng, Z. J. Wong, R. M. Ma, Y. Wang, and X. Zhang, "Single-mode laser by parity-time symmetry breaking," Science **346**, 972-975 (2014).

95. Y. Zhu, Y. Zhao, and L. Zhu, "Modal Discrimination in Parity-Time-Symmetric Single Microring Lasers," IEEE Photonics Journal **9**, 1-8 (2017).

96. S. Longhi, "PT-symmetric laser absorber," Physical Review A **82**(2010).

97. Z. J. Wong, Y.-L. Xu, J. Kim, K. O'Brien, Y. Wang, L. Feng, and X. Zhang, "Lasing and anti-lasing in a single cavity," Nature Photonics **10**, 796-801 (2016).

98. Y. Sun, W. Tan, H. Q. Li, J. S. Li, and H. Chen, "Experimental Demonstration of a Coherent Perfect Absorber with PT Phase Transition," Physical Review Letters **112**(2014).

99. N. D. Heidel, N. G. Usechak, C. L. Dohrman, and J. A. Conway, "A Review of Electronic-Photonic Heterogeneous Integration at DARPA," IEEE Journal of Selected Topics in Quantum Electronics **22**, 482-490 (2016).

100. Y. D. Chong, L. Ge, and A. D. Stone, "PT-symmetry breaking and laser-absorber modes in optical scattering systems," Phys Rev Lett **106**, 093902 (2011).